Metal / Organic and Metal / Inorganic Interfaces:

Interfacial Bond Energies, Structure and Energy-Level Alignment

James C. Sharp

A dissertation

submitted in partial fulfillment of the

requirements for the degree of

Doctor of Philosophy

University of Washington

2014

Reading Committee:

Prof. Charles T. Campbell, Chair

Prof. Bruce H. Robinson

Prof. Christine K. Luscombe

Program Authorized to Offer Degree:

Chemistry

Abstract

Metal / Organic and Metal / Inorganic Interfaces:

Interfacial Bond Energies, Structure and Energy Level Alignment

James C. Sharp

Chair of the Supervisory Committee:

Professor Charles T. Campbell

Chemistry

Metals deposited on surfaces play an important role in many applications, such as heterogeneous catalysts, fuel cells, photovoltaics, microelectronics and coatings. Further insight into the energetics and structure of metals deposited on surfaces can lead to more efficient catalysts and photovoltaics. The first part of this dissertation details the results from studying the adsorption of Ca onto poly[2-(2-ethylhexyloxy)-5-methoxy-1,4-phenylene cyanovinylene] (MEH-CN-PPV), poly(9,9-di-*n*-hexyl-2,7-fluorene) (PDHF) and poly(9,9-di-*n*-hexyl-2,7-fluorene vinylene) (PDHFV), polymers of interest for organic photovoltaics. Insights into interfacial binding were obtained using microcalorimetry, X-ray photoelectron spectroscopy (XPS) and low energy ion scattering spectroscopy (LEIS). The second part details the results from studying Ag adsorption onto Fe_3O_4(111) using the same techniques, and the third part describes a new method for analyzing signal intensities measured during thin film growth by electron spectroscopies, such XPS and Auger electron spectroscopy (AES), to determine

quantitative details of film morphology, specifically extending the well-known "hemispherical cap model" to angles of detection other than normal to the surface.

For the adsorption of Ca on polymer surfaces, it is found that whenever the polymer contains atoms other than hydrogen or carbon, Ca reacts aggressively with these heteroatoms with high heat. For MEH-CN-PPV, Ca was shown to initially react with the cyano group and form $Ca(CN)_2$ clusters (ΔHads = 436 kJ/mol). There is also XPS evidence for Ca reacting with some of the ether groups to make Ca alkoxides at low coverage. After that, Ca reacted with other Ca on the surface to form 3D islands of Ca(s) (ΔHad = 464 kJ/mol) until ~15 ML of Ca coverage, where the polymer surface is completely covered by Ca. For both PDHF and PDFHV, which ideally contain only hydrogen and carbon, the amount of Ca that reacted aggressively with the polymer was 10-fold less than the amount observed for polymers with heteroatoms. Its initial high heat of adsorption (253-315 kJ/mol) is attributed to Ca reacting with impurities or defects in either PDHF or PDFHV. After reaction with defects or impurities, Ca forms 3D Ca(s) islands which eventually grow together to make continuous film.

For Ag on Fe_3O_4(111), Ag was found to adsorb with an initial heat of adsorption ~230 kJ/mol and increase to within a few percent of the heat of sublimation of bulk Ag (285 kJ/mol) by ~2 ML Ag. Using AES, low energy ion scattering spectroscopy (LEIS), and modeling the growth of Ag on the surface as hemispherical caps, it was found that Ag had a particle density of ~4 x 10^{12} particles/cm^2, from which the heat of adsorption versus particle diameter was extracted.

Table of Contents

List of Tables

List of Figures

Acknowledgements

Funding for the work presented in this dissertation comes from the National Science Foundation under CHE-1010287 and Department of Energy, Office of Basic Energy Sciences, Chemical Sciences Division under Grant No. DE-FG02-96ER14630. J. C. Sharp foremost thanks Professor Charles Campbell for his guidance and wisdom throughout the completion of the work presented here. I would also like to thank Jack Baricuatro for many thought provoking conversations and for taking the time and effort to educated me on the basics of ultrahigh vacuum technology; Brian Holm and John Heutink for their instruction and work in the Chemistry machine shop; Jim Gladden, Lon Buck, Roy Olund, and Bill Beaty for their instruction and work in the Chemistry electronics shop; and the Campbell group members I have had the pleasure of working with: Dr. Jason Sellers, Dr. Jason Farmer, Dr. Wanda Lew, Dr. Eric Karp, Trent Silbaugh, Trevor James, Stephanie Hemmingson, and Christopher Wolcott.

Chapter 1 Introduction

Metal / organic and metal / inorganic interfaces are used in a wide variety of important technological applications. Metal / organic interfaces must be produced when making organic light emitting diodes (OLEDs)[1], organic photovoltaics (OPVs)[2], and photodiodes,[3] and coatings In OPV and OLEDs, this interface is responsible for charge injection and extraction. Metal / inorganic interfaces are crucial in heterogeneous catalysts, fuel cells and other electrocatalysts, microelectonics, coatings, chemical and biochemical sensors and photocatalysts. The nature and strength of the chemical bonding interactions at the metal / substrate interface is very important to the material's performance. For example, in catalytic materials, which are often made from late transition metal nanoparticles dispersed across the surface of some oxide support material, the material's catalytic activity, selectivity and long-term stability against deactivation by sintering are all thought to depend sensitively upon the strength of bonding of the metal to the oxide.[4-7]

Metal / Organic Interfaces: Ca on Semiconducting Polymers

The use of semiconducting π-conjugated polymers for organic photovoltaics (OPV), organic light emitting diodes (OLED), and organic field effect transistors (OFET) is widely studied. The use of polymers has advantages over using inorganics in that the polymers' light absorption, light emission and solubility can be tuned synthetically by either using a different backbone or by attaching different substituents to the polymer backbone. Since the polymers are soluble, new avenues of device production are available to the polymers, such as spin-coating, solvent casting, inkjet printing, and chemical vapor deposition. Electronic devices based on polymers also have

some disadvantages when compared with those using inorganics. Generally, their lifetime and efficiency are not yet acceptable for commercial devices. In photovoltaic and OLED devices based on such polymers, it is often necessary to use a thin film of a low work function metal at the metal/polymer interface to tune the energy level alignment between the electrode and the polymer,[8] and calcium is a common metal used in these applications,[9-11] often protected by an overcoat of a less reactive metal like Al.

Some common polymers used for OPVs and OLED are derivatives of poly(alkylthiophenes) (PATs) poly(*p*-phenylene vinylenes) (PPVs) and polyfluorenes (PFs). The interface formation between calcium and poly(3-hexylthiophene) (P3HT) has been previously studied.[12,13] Based on X-ray photoelectron spectroscopy (XPS) and calorimetry data, it was found that Ca interacted with the sulfur in the thiophene to from CaS(s). The Ca was able to react with sulfur down to a depth of ~ 3 nm. After that, based on low energy ion scattering spectroscopy (LEIS), XPS and calorimetry data, Ca forms 3D islands the P3HT surface.

The interface between Ca and PPV derivatives has been previously studied.[14-19] Ettegui *et al.*[17] investigated the formation of Ca / PPV interface by XPS and found that Ca reacted with oxygen impurities present. Andersson *et al.*[18] argue that Ca oxidizes the carbon-carbon double bond in the polymer backbone based on XPS and secondary ion mass spectrometry results of Ca deposited on OC_1C_{10}–PPV. Hon *et al.*[16] studied the interface formation between Ca and poly[2-methoxy,5-(2'-ethylhexyloxy)-*p*-phenylene] and poly[2-methoxy,5-(2'-ethylhexyloxy)-p-phenylene-vinylene] (MEH-PPV) using adsorption microcalorimetry and concluded that Ca reacts with vinylene in the backbone of MEH-PPV. For their reported heats of adsorption, they assumed that Ca had unity sticking probability. The previous work on Ca adsorption on P3HT

along with Ca adsorption on poly(methyl methacrylate) (PMMA)[20] show this assumption not to be valid until high coverages of Ca.

In Chapter 3, the results of Ca adsorption onto poly[2-(2-ethylhexyloxy)-5-methoxy-1,4-phenylene cyanovinylene] (MEH-CN-PPV), a cyano-substituted PPV, studied by XPS, LEIS, and calorimetry is reported. Cyano-substituted PPVs are of interest because of their higher electron affinity compared to unsubstituted PPVs and their ability to be used as an electron transport layer[9,21-25] and their ability to act as either a donor or acceptor in OPVs.[9-11,26]

Polyfluorenes are of interest due to their use in blue emitting OLEDs[27-30] and in blends for OPVs.[31,32] The interface between Ca and poly(9,9-dioctyfluorene) (PFO), a PF derivative, has been widely studied for use in blue emitting OLEDs[27-30] and in blends for solar cells.[31,32] The interface between Ca and PFO has been previously studied by XPS and UPS.[27,33] The authors found Ca induces a decrease in work function and a downward band bending, and gives rise to UPS peaks in the band gap which can be interpreted as being due to Ca clusters and eventually bulk-like metallic Ca.

In Chapters 4 and 5, the results of Ca adsorption on pristine and electron-damaged poly(9,9-di-*n*-hexyl-2,7-fluorene (PDHF) and poly(9,9-di-*n*-hexyl-2,7-fluorene vinylene (PDHFV) studied by UPS, LEIS, and calorimetry are reported. The two polymers PDHF and PDHFV differ only by the inclusion of vinylene in the backbone of PDHFV not present in PDHF. Previous theoretical[34] and experimental[16,18] work on poly(*para*-phenylene-vinylene) (PPV) has suggested that the vinylene moiety could be a reactive site for Ca. It should be noted that the PPV derivatives used in those two experimental studies[16,18] had oxygen-containing side groups, while PDHF and PDHFV only consist of carbon and hydrogen. More recent theoretical studies of Ca /

PPV without these oxygen-containing side groups show very weak interaction between Ca and the polymer chain.[19]

Metal / Inorganic Interfaces: Catalytic-interesting Metals on Oxide Surfaces

Nanoparticles of late transition metals dispersed across the surface of oxide support materials are the key ingredients in many heterogeneous catalysts, fuel cells, other electrocatalysts and photocatalysts, which are crucial for energy, fuel and environmental technologies and chemical processing.[7,35-38] In such materials, the nature and strength of the chemical bonding interactions at the interface between the metal nanoparticle and the oxide support surface are very important to the material's performance, such as its catalytic activity, selectivity and long-term stability against deactivation by sintering.[4-7] The strength of the interaction for metal adsorption and adhesion onto oxide surfaces is not known for many systems, yet this determines the chemical potential of the metal atoms in the supported nanoparticles, which has been shown to directly correlate with their resistance to sintering and their chemical and catalytic reactivity.[6] Work in the Campbell Group has already presented a ranking of a small selection of oxide supports by the strength of the bonding with metal nanoparticles.[39] Also of importance for these systems is the nanoparticle size, as the size can affect the catalytic properties and selectivity.[40,41]

In Chapter 6, the results of Ag adsorption onto $Fe_3O_4(111)$ as studied by LEIS, AES, low energy electron diffraction (LEED), calorimetry are presented. Iron oxides are promising materials for many of the previously mentioned applications. Many researchers have studied metal nanoparticles supported on the magnetite $Fe_3O_4(111)$ surface.[42-49] For example, gold particles supported on $Fe_3O_4(111)$ has been studied for carbon monoxide oxidation and water gas shift.[49] Water gas shift has also been studied over copper particles on $Fe_3O_4(111)$.[48] Palladium

on Fe_3O_4(111) has been studied for CO oxidation.[42-44] Particulate Ag, usually supported on other oxides, is known to be a catalyst for epoxidation of olefins, partial oxidation of methanol, and oxidation of carbon monoxide, and hydrogen.[50,51]

Chapter 7 presents a new method for determining the average size and number density of adsorbed 3D nanoparticles dispersed across a flat solid support surface, based upon quantitative analysis of AES or XPS signal intensities versus the total deposited amount of adsorbed material. As mentioned previously, the size of the nanoparticle can dramatically affect the catalytic properties and selectivity.[40,41] Knowing the average size of the nanoparticle can also be of use in many other applications. A much-used model for determining the average size and number density of adsorbed nanoparticles from measured AES or XPS signal intensities versus coverage when the detection angle is normal to the surface has already been derived.[52] It is called the "hemispherical cap model", and assumes that the nanoparticles keep a fixed number density as the coverage increases, and all have the shape of hemispherical caps, with the same diameter at a given total coverage. These assumptions are reasonably consistent with experimental observations during physical vapor deposition and the kinetic models used to explain.[53] The new method detailed in Chapter 7extends this hemispherical cap model to allow its application to AES or XPS data taken at an angle of detection other than normal, which significantly complicates the theoretical calculation of signal intensities.

Chapter 2 Experimental

To study these interfaces, techniques such as X-ray photoelectron spectroscopy (XPS), Auger electron spectroscopy (AES), low energy ion scattering spectroscopy (LEIS), and microcalorimetry are utilized. XPS, AES, and LEIS give information about the growth mode of metals deposited on these surfaces with XPS also being able to give chemical state information. An in-depth review of the these techniques can found here.[54]

Microcalorimetry is a technique to determine the heat of metal atom adsorption on these surfaces by a direct measurement of the temperature change. This technique was pioneered by Sir David King's research group using an optical pyrometer to detect temperature changes when a dose of adatoms impinged on the single crystal surface.[55-57] Professor Campbell's group improved upon this design by utilizing β-Polyvinylidene fluoride (PVDF) as the heat detector.[58,59] For experiments with semiconducting polymers, the polymer of interest is spin-coated directly onto the PVDF using 0.5% w/w solution of polymer in $CHCl_3$. This leads to an approximately 100 nm thick film. When metal atoms are dosed, the heat released can be measured by the change in the face to face voltage across the PVDF, which is linearly proportional to the heat input over the region measured in our experiments. The voltage response is calibrated using heat input from a He-Ne laser of known power.

The fraction of metal atoms that stick to the surface, sticking probability, is measured using a modified Kings-Wells method.[58] The total number of dosed metal atoms in each pulse is determined using a quartz crystal microbalance (QCM). A zero sticking flag is then utilized to reflect the metal atoms. The reflected metal atoms are measured using a quadrupole mass spectrometer (QMS) and the signal of the QMS is calibrated. A metal mesh placed between the

QMS and the sample was biased at negative 500 volts to avoid any electron damage on the sample. While dosing metal atoms onto the sample, The QMS is used to measure the fraction of metal atoms in each pulse that do not stick adsorb to the sample. A cartoon of this setup is shown in Figure 2.1.

For metal adsorption on oxide surfaces, the method of heat detection is modified. Instead of growing the oxide on PVDF, the oxide is grown on a 1 μm thick single crystal of Pt(111). The growth of oxide surfaces generally requires temperatures greater than PVDF can withstand and be useful as a heat detector. For heat detection, a ribbon of PVDF is pressed against the back side of the Pt(111) crystal and the face to face voltage across the PVDF ribbon can be measured. As with the polymer setup, the face to face voltage is calibrated with using heat input from a He-Ne laser of known power and is linearly proportional to the heat input over the region measured in our experiments.

2.1 Figures

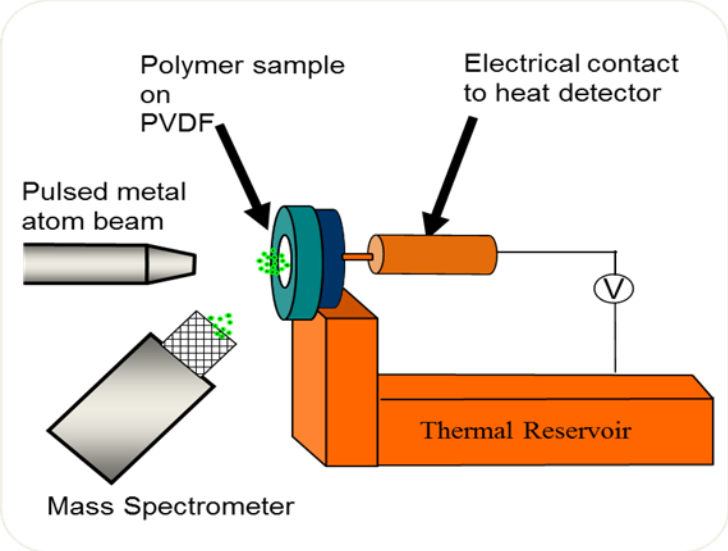

Figure 2.1 A cartoon of the microcalorimetry apparatus that is housed in an ultra-high vacuum chamber. Metal atoms are dosed at the sample and generate a face to face voltage across PVDF when they adsorb. The fraction of metal atoms that don't adsorb is measured by the mass spectrometer.

Chapter 3 Calcium Thin Film Growth on a Cyano-substituted Poly(*p*-phenylene vinylene): Interface Structure and Energetics

J. C. Sharp,[†] F. Bebensee,[‡,∥] J. H. Baricuatro,[†] H.-P. Steinrück,[‡] J.M. Gottfried,[‡,§] and C.T. Campbell[†]

[†]*Department of Chemistry, University of Washington, Seattle, Washington 98195-1700*

[‡]*Lehrstuhl für Physikalische Chemie II and Interdisciplinary Center for Molecular Materials, Universität Erlangen-Nürnberg, Egerlandstr. 3, 91058 Erlangen, Germany*

[∥]*Institut für Funktionelle Grenzflächen (IFG), Karlsruher Institut für Technologie (KIT), Hermann-von-Helmholtz-Platz 1, D-76344 Eggenstein-Leopoldshafen, Germany*

[§]*Fachbereich Chemie, Philipps-Universität Marburg, Hans-Meerwein-Str., 35032 Marburg, Germany*

Abstract

The adsorption of Ca on poly[2-(2-ethylhexyloxy)-5-methoxy-1,4-phenylene cyano-vinylene] (MEH-CN-PPV) at 130 and 300 K has been studied by adsorption microcalorimetry, X-ray photoelectron spectroscopy (XPS), and low-energy He^+ ion scattering spectroscopy (LEIS). The initial heat of adsorption of Ca on MEH-CN-PPV at 300 K is 436 kJ/mol. The heat of adsorption increases to 464 kJ/mol at ~0.05 ML. We ascribe this initial heat to Ca abstracting cyano groups from the polymer backbone to make $Ca(CN)_2$ clusters, plus a less important contribution due to Ca abstracting alkoxy groups to make Ca alkoxides. This is supported by

XPS which shows the formation of new peaks in the N 1s and C 1s regions consistent with $Ca(CN)_2$. There is also XPS evidence for Ca reacting with some of the ether groups to make Ca alkoxides at low coverage. Above 0.05 ML Ca coverage, the heat of adsorption decreases nearly exponentially to the sublimation enthalpy of bulk Ca solid (178 kJ/mol) by 5 ML. The observed behavior is attributed to the increasing probability of forming Ca nanoparticles and eventually a continuous solid Ca film on top of the reacted polymer. LEIS, which shows only a slow increase of the signals related to solid Ca, supports this model. Incoming Ca atoms undergo a kinetic competition between diffusing into the polymer to react with subsurface cyano or ether groups versus forming or adding to three-dimensional Ca clusters on the surface. For studies done at 130 K, similar behavior is observed, with the heat of adsorption starting lower and decreasing more quickly to the heat of sublimation, already by 1.2 ML Ca coverage. This behavior along with the quicker growth of Ca on the surface of the polymer is attributed to the slower diffusion of Ca adatoms to subsurface cyano and ether groups. The effective thickness of "reacted" polymer (i.e., polymer which has lost its –CN groups and some alkoxy groups) is estimated to be 5.6 nm at 300 K but only 1.0 nm at 130 K.

3.1 Introduction

Interfaces formed between metals and semiconducting π-conjugated polymers play an important role in organic electronic devices such as organic light emitting diodes (OLEDs)[1], organic photovoltaics (OPVs)[2], and photodiodes.[21] One class of semiconducting polymers that is of interest for these devices is cyano-substituted poly(*p*-phenylene vinylenes) (PPVs) because of their higher electron affinity compared to unsubstituted PPVs and their ability to be used as an

electron transport layer.[9,21-25] One of the most studied polymers in this class is poly[2-(2-ethylhexyloxy)-5-methoxy-1,4-phenylene cyanovinylene] (MEH-CN-PPV, see Fig. 3.1 for structure) due to its improved solubility properties and higher luminescence efficiency in the red.[9,11,22,60] In photovoltaic and OLED devices based on such polymers, it is often necessary to use a thin film of a low work function metal at the metal/polymer interface to tune the energy level alignment between the electrode and the polymer,[8] and calcium is a common metal used in these applications,[9-11] often protected by an overcoat of a less reactive metal like Al. Thus, the Ca interface to MEH-CN-PPV is interesting from the point of view of OPV and OLED devices. Most importantly, it serves as a prototype system for study of all metal / polymer interfaces between alkaline earth metals and cyano-substituted polymers, especially those with functional groups similar to those in PPVs. In this paper, we study the formation, structure and bonding energetics of the calcium / MEH-CN-PPV interface as Ca is vapor deposited onto the clean surface of MEH-CV-PPV, as done in typical device fabrication. We find that a very aggressive reaction occurs between Ca and the cyano groups of the polymer which continues down to a depth of more than 5 nm, and which is likely to occur for many polymers containing -CN groups. Adsorption microcalorimetry was used to measure the heat of Ca atom adsorption as a function of Ca coverage, and He^+ low-energy ion scattering spectroscopy (LEIS) was used to determine the fraction of the polymer surface covered by Ca during growth of the calcium film. High-resolution X-ray photoelectron spectroscopy was used to probe the character of the local chemical bonding at the interface.

To our knowledge, no other studies exist studying the formation of the Ca / MEH-CN-PPV interface using XPS, LEIS, or adsorption microcalorimetry. The interface between Ca and other PPV derivatives has been previously studied.[14-19] Ettegui *et al.*[17] investigated the formation

of Ca / PPV interface by XPS and found that Ca reacted with oxygen impurities present. Andersson *et al.*[18] argue that Ca oxidizes the carbon-carbon double bond in the polymer backbone based on XPS and secondary ion mass spectrometry results of Ca deposited on OC_1C_{10}–PPV. Hon *et al.*[16] studied the interface formation between Ca and poly[2-methoxy,5-(2'-ethylhexyloxy)-*p*-phenylene] and poly[2-methoxy,5-(2'-ethylhexyloxy)-p-phenylene-vinylene] (MEH-PPV) using adsorption microcalorimetry and concluded that Ca reacts with vinylene in the backbone of MEH-PPV. For their reported heats of adsorption, they assumed that Ca had unity sticking probability. As shown below for the similar system studied here, the sticking probability drops to 0.65. If the sticking probability were actually 0.65 in that case, their reported heats were too low by over 50%. The interface between aluminum and poly(2,5,2',5'-tetrahexyloxy-8,7'-dicyanodi-*p*-phenylenevinylene) (CN-PPV) was studied both by XPS and quantum-chemical calculations.[23] Aluminum was found to form covalent bonds with the nitrogen and carbon in the cyano group in CN-PPV.

3.2 Experimental

The MEH-CN-PPV polymer were obtained from Sigma Aldrich (purity verified by manufacturer using proton NMR and infrared spectra) and used without further purification. Solutions of 0.5 % w/w polymer in chloroform were prepared and 120 μL of this solution was spin-coated directly onto the pyroelectric β-polyvinylidene fluoride sheet used for heat detection at 2000 rpm for 30 s. This yielded a film thickness of ~100 nm, consistent with expectations based on prior work.[61] The film thickness was determined by spin coating the polymer onto a glass slide in exactly the same way, removing some of the film with a razor blade, and measuring

the film height with a profilometer. The samples were immediately transferred to the sample preparation chamber, pumped down to its base pressure of 8 x 10^{-9} Torr and outgassed while the polymer was heated at 330 K for ~10 hours to remove trace amounts of solvent. The samples were then transferred into the ultrahigh vacuum (UHV) analysis chamber when needed. No remaining solvent was detected with XPS and Auger Electron Spectroscopy (AES).

The UHV system used in these experiments had a base pressure 2 x 10^{-10} mbar and was equipped with a hemispherical energy analyzer (Leybold-Heraeus EA 11/100) for He^+ LEIS and Auger electron spectroscopy, an ion gun (Leybold-Heraeus IQE 12/38), a quartz crystal microbalance (QCM, Inficon), quadrupole mass spectrometer (UTI 100C), and adsorption microcalorimeter. The surface analysis chamber and pulsed metal atom beam have been described previously.[58] The Ca atom beam was chopped into 100 ms long pulses which contained ~0.02 ML of Ca at a rate of 0.5 Hz. One monolayer (ML) of Ca is defined here as the Ca(111) packing density, 7.4 x 10^{14} Ca atoms per cm^2. The metal atom adsorption microcalorimetry methods used in these experiments has been described in detail previously.[59,20] The heat detectors for the calorimeter were 1.3 cm diameter disks cut from a 9 μm thick sheet of β-polyvinylidene fluoride (PVDF) coated on both sides with ~60 nm films of nickel-aluminum that serve as the two electrodes for heat signal measurements (as purchased from Measurement Specialties, Inc.). The MEH-CN-PPV was directly spin coated onto these. These heat detector disks were mounted across the hole in a small sample holder plate as described elsewhere.[59]

For experiments performed at liquid nitrogen temperature, the procedure was described in detail previously.[62] Briefly, the temperature of the sample holder plate was controlled by flowing dry nitrogen through copper tubes immersed in liquid nitrogen, then through the thermal

reservoir on the calorimeter. The temperature was monitored by a thermocouple spot welded to the calorimeter.

The sticking probability for Ca on MEH-CN-PPV was determined using a quadrupole mass spectrometer (QMS) with the modified King-Wells method described previously.[63] A metal mesh placed between the QMS and the sample was biased at negative 500 volts to avoid any electron damage of the sample.

The growth of Ca on MEH-CN-PPV was studied by LEIS using $^4He^+$ ions with a primary energy of 1.00 keV and an angle of 45° between the ion source and analyzer axes (i.e., scattering angle = 135°). Ion fluxes were typically 100 nA/cm^2 with a total ion dose of 6 μC/cm^2 per experiment. For the XPS studies, the MEH-CN-PPV films were spin-coated onto a washed 0.1 mm thick Al foil in exactly the same way as for the calorimetric measurements (where the substrate was NiAl-coated β-PVDF instead).

The high-resolution XPS measurements were performed using a commercial X-ray photoelectron spectrometer (Scienta ESCA-200) with an Al anode X-ray source, a mono-chromator, and a hemispherical energy analyzer (SES-200). The UHV chamber (base pressure of below 2 x 10^{-10} mbar) also comprises a QMS (Pfeiffer HiQuad QMA 400), various evaporators, and a sample load-lock system. All spectra were recorded in normal emission with the binding energy (B.E.) referenced to the Fermi edge of a clean Ag(111) surface (B.E.=0), and the spectra were normalized to the background. For XPS, Ca was evaporated from a home-built Knudsen cell evaporator at a temperature of 873 K. The deposition rate, 2 Å/min at the sample position, was measured by monitoring the attenuation of the substrate XPS signals upon deposition of Ca onto an Au foil. More detailed descriptions of the equipment and the experimental procedures for XPS can be found in our previous publication[12] and the references therein.

3.3 Results

Sticking Probability. Figure 3.1 shows the sticking probability of Ca on MEH-CN-PPV at 130 K and 300 K as a function of Ca coverage. The flux of the Ca atomic beam was measured by the calibrated QCM. The Ca coverage was determined by time-integrating the product of the Ca flux times the sticking probability, taking into consideration the chopped Ca beam's "on" time. Each curve in the figure is the average of 3 independent runs.

For Ca on MEH-CN-PPV at 130 K, the curve starts at an initial sticking value of 0.92 and increases asymptotically towards unity. At 300 K, the initial sticking probability is 0.69. The sticking probability initially increases to 0.75 at 0.1 ML and then decreases to 0.63 at 1.5 ML. Thereafter it increases asymptotically towards unity.

The lineshape of the Ca mass spectrometer signal versus time for the atoms which did not stick at 300 K was analyzed and indicated that they had negligible surface residence time (<10 ms). Assuming that these atoms which did not stick permanently were nevertheless transiently adsorbed as monomers on the polymer surface, this short residence time suggests they were bonded very weakly to the polymer. Estimating the pre-exponential factor for desorption to be 10^{13} s^{-1} at 300 K using the method described in ref. [64], this short residence time implies a desorption energy below 64 kJ/mol.

Low-Energy Ion Scattering Spectroscopy. When metal is vapor deposited onto a polymer film, the metal atoms can form 3D islands or a continuous film on the surface, or diffuse subsurface and react with functional groups of the polymer.[20,65-69] LEIS using He^+ is a valuable

tool for determining growth modes since it is only sensitive to the topmost surface layer and is element specific. Thus, it directly measures the fraction of the polymer covered by Ca.

Figure 3.2 shows the evolution of the normalized Ca LEIS signal on MEH-CN-PPV versus Ca coverage at 130 K and 300 K. Effects of beam damage by the He^+ ion beam were determined to be negligible by comparing measurements of signal versus coverage with 10-fold shorter cumulative beam exposure times, yielding results that were indistinguishable within the data scatter. As shown in Figure 3.22, the Ca signal initially grows much, much more slowly than would be expected by a layer-by-layer growth mode, at 130 K and 300 K. This can be attributed to Ca initially diffusing to below the surface and binding to subsurface reactive sites on the polymer. This continues until ~1.5 ML. At both 130 K and 300 K, the Ca LEIS signal begins to grow more rapidly starting at ~1.5 ML, but still much slower than expected for layer-by-layer growth. This trend is indicative of the formation of 3D Ca islands on the surface. The rate of Ca signal growth is higher on the 130 K surface than the 300 K surface, which is consistent with Ca being able to diffuse subsurface more rapidly at 300 K, and its ability to subsequently grow larger 3D particles at 300 K. The Ca LEIS signal does not reach its maximum intensity expected for a pure Ca surface until ~ 10 ML of Ca coverage at 130 K and ~15 ML for 300 K. (Data were collected out to 50 ML, but not shown here so we could expand the low-coverage behavior that is more important.)

X-Ray Photoelectron Spectroscopy (XPS). Figure 3.3 shows XP spectra of the C 1s, O 1s and N 1s regions for the clean MEH-CN-PPV surface, and their deconvolution into individual peaks. We assumed here that these had a fixed peak full-width at half maximum (FWHM) of 1.2 eV (to match the narrowest peaks observed in the N 1s spectrum at this same pass energy,

which we take to define the resolution used) and Gaussian lineshape. For the N 1s spectrum, the only species present is cyano nitrogen. The peak position of 399.7 eV binding energy (B.E.) agrees well with the value for poly(acrylonitrile) and poly(methacrylonitrile) of 399.57 eV.[70] The O 1s peak was deconvoluted into 3 peaks, O-CH_3, O-C_8H_{15}, and O=C, at binding energies of 533.5, 533.1 and 531.8 eV, respectively. The separation of 0.4 eV between O-CH_3 and O-C_8H_{15} is in good agreement with the difference between the O 1s peak of poly(vinyl isobutyl ether) and poly(vinyl methyl ether) of 0.27 eV.[70] These peak positions and the general O 1s shape are in agreement with those from MEH-PPV, where the individual peaks were not deconvoluted.[71] The peak due to the O=C subunit has also been seen with about this same relative intensity for MEH-PPV.[72] Since it is not in the repeat unit of these polymers, it must be associated with end groups and/or impurities. The C 1s spectrum in Fig. 3.3 was deconvoluted into five individual peaks: unsaturated carbon at 284.7 eV, saturated carbon at 285.0 eV, ether carbons and carbons bonded to the cyano group at 286.3 eV, cyano carbons at 287.0 eV, and carbonyl carbons at 288.1 eV. These B.E. assignments are based on reported B.E.s for polymers containing the same functional groups as listed in Appendix 1 of *High resolution XPS of organic polymers : the Scienta ESCA300 database*. Table 1 shows the B.E.s and percent contributions from each of these individual XPS peaks as obtained from the deconvolutions shown in Fig. 3.3.

	0 ML Ca			0.1 ML Ca		0.5 ML Ca		
Species	B.E. (eV)	% area	% area ideal	B.E. (eV)	% area	B.E. (eV)	% area	Ref
C 1s								
C_{unsat}	284.7	25.5	27.8	285.0	25.5	285.1	26.1	28
C_{sat}	285.0	39.7	38.9	285.3	39.6	285.4	39.1	28
C-O, C-CN	286.3	28.1	27.8	286.6	27.8	286.7	27.0	28
CN	287.0	5.7	5.6	287.3	4.5	287.4	3.2	28
C=O	288.1	1.0	0	288.4	1.0	288.5	1.5	28
$Ca(CN)_2$	-	0	0	286.0	1.6	286.1	3.1	32
N 1s								
CN	399.7	100	100	400.0	84.3	400.1	54.2	28
$Ca(CN)_2$	-	0	0	399.3	15.7	399.4	45.8	32
O 1s								
$O\text{-}CH_3$	533.5	46.5	50	533.8	44.1	533.9	39.4	28
$O\text{-}C_8H_{15}$	533.1	46.5	50	533.4	44.1	533.5	39.4	28
O=C	531.8	7.1	0	532.1	7.1	532.2	7.1	28
$Ca(OR)_2$	-	0	0	531.0	4.8	531.1	14.1	32

Table 3.1 Binding energies and percent composition for the deconvoluted XPS peaks in Figs. 3.3-5 for MEH-CN-PPV before Ca deposition and after dosing 0.1 and 0.5 ML of Ca at 300 K. The composition for the ideal unreacted polymer (based on its stoichiometry) is also listed.

Figure 3.4 shows XP spectra of the C 1s, O 1s and N 1s regions for the MEH-CN-PPV surface with 0.1 ML of Ca deposited at 300 K. In all regions of the spectrum the peaks shifted by 0.3 eV to higher B.E. from their values at 0 ML Ca coverage. This shift is most likely due to downward band bending associated with long-range electron donation from Ca into the polymer.[17,73] The N 1s region shows the appearance of a new peak at 399.3 eV. This peak is attributed to nitrogen in solid $Ca(CN)_2$. This is in agreement with values for other metal

cyanides which vary from 398.3 eV to 400.6 eV[74] The C 1s region develops a new peak at 286.0 eV attributed to solid $Ca(CN)_2$. This contribution is small, but significant and can be seen already in the raw spectra by the disappearance of the dip at 286.0 eV (compare the C 1s spectra in Figures 3.3 and 3.4). The B.E. is consistent with values for KCN and NaCN of 286.1 eV and 286.2 eV, respectively.[74] The O 1s region also shows the formation of a new peak at 531.0 eV, which is similar to the reported B.E. of 531.2 eV for solid $Ca(OH)_2$ [75] This peak is attributed to solid Ca alkoxides, labeled here as $Ca(OR)_2$, due to Ca abstracting alkoxy groups from the polymer. This new peak may also have some contribution from the reaction of Ca with water impurity present in the background gas. However, this is unlikely as large a contribution as from Ca alkoxides since the same sample preparation method was used in our studies of Ca adsorption on P3HT [12] and no O 1s peak was seen, showing that any surface contamination from adsorbed water was below the detection limits of XPS.

Figure 3.5 shows XP spectra of the C 1s, O 1s and N 1s regions for the MEH-CN-PPV surface with 0.5 ML of Ca deposited at 300 K. In all regions of the spectrum the peaks shifted by 0.1 eV to higher binding energy from their values at 0.1 ML Ca coverage. The peaks for $Ca(CN)_2$ in the N 1s and C 1s regions increase relative to the other peaks, showing continued formation of $Ca(CN)_2$. In the O 1s region, the $Ca(OR)_2$ peak also grows relative to the other peaks in the same region.

Table 3.1 also shows the B.E.s and percent contributions from each of these individual XPS peaks as obtained from the deconvolutions shown in Figs. 3.4 and 3.5 after dosing Ca. In this coverage range, the Ca 2p XPS spectrum remains as a doublet of narrow $2p_{3/2}$ and $2p_{1/2}$ peaks, with the $2p_{3/2}$ peak at 348.5 eV B.E., as expected for Ca in ionic compounds. No evidence is seen at 0.5 ML and below for intensity in this peak at the B.E. expected for metallic

Ca(solid), of ~346.5 eV, nor for the intense tail at higher binding energy (353-357 eV) due to the plasmon loss expected if metallic Ca(solid) were present.[76] This observation that Ca is in the Ca^{2+} form below 0.5 ML is consistent with the other evidences presented below for the formation of mainly $Ca(CN)_2$, plus some Ca alkoxide, in this coverage range, with metallic Ca(s) forming only at higher coverages.

Heat of Adsorption. Figure 3.6 shows the differential heat of adsorption of Ca on MEH-CN-PPV at 130 K and 300 K as a function of Ca coverage. Each of the curves is the average of 3 independent runs. The heat of adsorption in the limit of zero coverage is 325 kJ/mol at 130 K and 430 kJ/mol at 300 K. It then increases slightly at both temperatures until about 0.05 ML, and thereafter decreases slowly in an exponential-like decay to 179±2 kJ/mol at high coverages, which it approaches to within a few percent by ~1.3 ML at 130 K and ~4.5 ML at 300 K. This final value is within experimental error of the reported heat of sublimation of Ca, 178 kJ/mol[77], as expected for Ca adsorption onto pure Ca solid.

3.4 Discussion

The experimental results can be summarized as follows:

a) The LEIS intensity of Ca increases much more slowly with Ca coverage than expected for layer-by-layer growth.

b) The XPS results show the formation of solid $Ca(CN)_2$ and $Ca(OR)_2$, and loss of relative intensity in the carbon-carbon portion of the C 1s peak, upon Ca deposition at low coverages up

to 0.5 ML, but Ca(s) is clearly formed at very high coverages as shown by the heat of adsorption and LEIS.

c) The heat of Ca adsorption on MEH-CN-PPV for low and medium Ca coverages (<4 ML) is very high (up to 465 kJ/mol at 300 K), and much larger in magnitude than the heat of bulk Ca sublimation (178 kJ/mol).

d) The heat of Ca adsorption approaches the heat of bulk Ca sublimation at high coverages.

e) Lowering the temperature of the MEH-CN-PPV decreases the amount of Ca needed for the heat of Ca adsorption to reach the heat of bulk Ca sublimation, and increases the rate at which Ca LEIS intensity grows on the surface

In the following, we will describe a model for the formation of the Ca / MEH-CN-PPV interface which is consistent with these results.

As shown in Figure 3.2, the Ca LEIS signal grows much more slowly with Ca coverage than expected for the formation of a continuous first layer and subsequent layer-by-layer or 3D growth for both temperatures. This is consistent with either 3D Ca island growth or the diffusion of Ca down into the subsurface or bulk region of the polymer, or both. For 3D Ca island growth, the heat of adsorption should be equal to the heat of sublimation of bulk Ca, 178 kJ/mol, or less in the case of small Ca clusters due to the formation of fewer Ca-Ca bonds.[78] Figure 3.6 shows a much higher heat of adsorption than 178 kJ/mol at low coverages, starting as high as 450 kJ/mol at 300 K, and it remains higher up to 4 ML at 300 K and 1¼ ML at 130 K. Thus the adsorbed Ca must diffuse to subsurface where a more exothermic reaction occurs than Ca(s) formation. This is consistent with the XPS results, which show the formation of Ca cyanide and Ca alkoxide. Note that the -CN and -OR groups of the polymer are expected to be subsurface, since the alkyl chains of such polymers usually enrich at the surface due to their lower surface energy.[79,80]

We propose that the reaction which occurs between Ca and the -CN groups of the polymer is similar to the following reaction, whose standard heat at 298 K (ΔH^0_{rxn}) could be calculated using thermodynamic tables of heats of formation [77,81]:

$$Ca(g) + 2C_2H_3CN(l) \rightarrow Ca(CN)_2(s) + C_4H_6(g) \quad (1)$$

$$\Delta H^0_{rxn} = -546 \text{ kJ/mol.}$$

In this proposed reaction, each Ca atom extracts two cyano groups from MEH-CN-PPV and forms $Ca(CN)_2$, followed by polymer-polymer coupling between two C atoms which lost their -CN groups. This is consistent with the XPS data, which shows formation of a new peak at 286.0 eV in the C 1s spectra and 399.3 eV in the N 1s spectra in Fig. 3.5 attributed to $Ca(CN)_2$. The observed heat of adsorption has a maximum value of 465 kJ/mol, which is 80 kJ/mol less than this heat. This difference could be caused by the much lower heat of formation expected for small $Ca(CN)_2$ clusters than for bulk $Ca(CN)_2$(solid), as was observed for CaS clusters made by reacting Ca with the polythiophene P3HT.[12]

Another reaction that contributes to the high initial heat of adsorption is the abstraction of alkoxy groups by Ca to make Ca alkoxide and the subsequent polymer-polymer coupling between two C atoms which lost their alkoxy groups. That is, a reaction of the type:

$$Ca(g) + 2\ ROR'(l) \rightarrow Ca(OR)_2(s) + R'_2(g), \quad (2)$$

where R is any alkyl group and R´ is any hydrocarbon group. This is consistent with the observation of the formation of Ca alkoxides by XPS in Figs. 3.4-5. The heat for this type of reaction must be similar to the standard heat for the reaction:

$$Ca(g) + 2\ EtOH(l) \rightarrow Ca(OH)_2(s) + \text{n-butane}(g), \quad (3)$$

which is -755.1 kJ/mol at 298 K.[77] Again, this is higher than the maximum observed heat of 465 kJ/mol, which again may be due to cluster size effects. The XPS data of Table 1 shows that

this reaction of Ca with –OR groups is much less likely than the reaction of Ca with –CN groups: by 0.5 ML Ca, 45% of –CN groups have reacted with Ca whereas only 14% of the –OR groups have reacted. As shown in Fig. 3.3, there are more than ten times fewer C=O species than –OR groups in the starting surface, which may explain the higher probability for Ca to react with the alkoxy groups than with these C=O impurities, even though the probability to react with alkoxy group is still low compared to Ca reacting with cyano groups.

The LEIS data in Fig. 3.2 clearly show that at the condition of this maximum heat in Fig. 3.6 (i.e., 0.07 ML Ca and 300 K), a negligible fraction of the Ca that adsorbs resides in the topmost atomic layer as clusters of Ca(s). That is, the reaction is clearly dominated here by Reactions (1) and (2), where the Ca interacts with subsurface heteroatoms. On the other hand, at high coverages, the heat of adsorption is equal to the heat of sublimation of bulk Ca(s) at both temperatures, and the LEIS shows that the surface is nearly pure Ca. Thus, at high coverages, the dominant reaction is Ca(g) making Ca(s).

We now use a simple two-state model to estimate the effective thickness of reacted polymer (i.e., the amount of polymer whose –CN groups or -OR have been abstracted by Ca either by Reaction (1) or (2). The model assumes that the measured heat of adsorption has two contributions, one due to Reaction (1) or (2) with an average heat equal to the maximum heat observed (465 kJ/mol, see Fig. 3.6), and a second due to formation of Ca(s) with a heat equal to its bulk heat of sublimation (178 kJ/mol). The differential heat of adsorption at any Ca coverage (ΔH_{ad}) is a simple sum of the fraction *f* of Ca in that pulse that reacts with -CN or –OR groups times 465 kJ/mol and the remaining fraction (1-*f*) times 178 kJ/mol:

$$\Delta H_{ad} = f\,(465\ \text{kJ/mol}) + (1-f)\,(178\ \text{kJ/mol}). \qquad (4)$$

This equation can be solved to give the value of *f* for each coverage from its measured ΔH_{ad} value. The resulting *f* values look identical to the heat curves in Fig. 3.6 except that they are rescaled such that 465 kJ/mol corresponds to $f = 1$ and $f = 0$ is at 178 kJ/mol. Multiplying *f* by the amount of Ca that adsorbed in that pulse and integrating with time gives the total amount of "reacted Ca" at that coverage. This is shown in Fig. 3.7 versus Ca coverage at both 300 and 130 K. As seen, 1.15 ML of Ca reacts at 300 K and saturation coverage, but only 17 % as much (0.20 ML) reacts at saturation at 130 K.

We converted this reacted Ca coverage to the effective "reacted thickness" by assuming that the dominant reaction (i.e., the reaction with –CN groups) is the only reaction (i.e., neglecting the small contribution from -OR reactions) using the number density of repeat units ("monomers") in this polymer, the knowledge that there are two –CN groups per repeat unit (see Fig. 3.1) and assuming the $Ca(CN)_2$ stoichiometric ratio of Reaction (1), following a similar procedure to that described previously.[20] We assumed that the number density of repeat units in MEH-CN-PPV is approximately the same as in MEH-PPV. The number density of repeat units in MEH-PPV was calculated from its reported crystal structure[80] to be 1.53×10^{21} repeat units per cm^3. Assuming that the repeat units are packed like spheres in FCC closest packing, the closest-packed face (i.e., the (111) face) would have a packing density of 1.22×10^{14} repeat units per cm^2 and a monomer layer thickness of 0.80 nm. Remembering the Ca : CN reaction stoichiometry of 1:2 and the fact that there are 2 –CN groups per repeat unit, one ML of reacted Ca (7.4×10^{14} Ca /cm^2) thus corresponds to 6.1 repeat unit layers or an effective reacted thickness of 4.9 nm. Figure 3.7 also shows this estimated thickness of reacted polymer versus Ca coverage. From this plot, one can see that the total effective thickness of reacted polymer at saturation is ~5.6 nm (~7 layers of monomers) at 300 K but only ~1.0 nm at 130 K.

The much lower initial heat at 130 K than at 300 K shows that the fraction of Ca that makes Ca(s) is much larger at 130 K than at 300 K (and *f* is much smaller). This is consistent with Ca diffusion to subsurface functional groups being slower at this lower temperature, which is expected to decrease the contributions from Reactions (1) and (2) in this three-reaction kinetic competition. This same effect of temperature was observed for Ca on P3HT[82] and OC_1C_{10}-PPV.[14]

At 300 K, the sticking probability for Ca is always substantially below unity (Fig. 3.1). Thus, some of the diffusing Ca monomers are neither able to find a subsurface -CN or -OR group with which to react nor are they able to attach to a growing Ca(s) cluster before they desorb back into the gas phase. Since their desorption will be faster at 300 K than at 130 K, one expects a substantially lower sticking probability at 300 K than at 130 K, as indeed observed (Fig. 3.1). The decrease in sticking probability from 0.75 to 0.63 as coverage increases from 0.1 to 1.5 ML at 300 K is due to the fact that the Ca must diffuse deeper and deeper to find a subsurface -CN or -OR group with which to react as the extent of that reaction proceeds. Its later asymptotic increase towards unity starting at ~1.5 ML reflects the fact that most of the Ca that sticks is making particles of Ca(s) starting at ~1.5 ML, and that pure Ca(s) has unit sticking probability for Ca(g) at 300 K.[20,83] This increase reflects the increasing fraction of the surface covered by Ca(s) as measured by LEIS (Fig. 3.2). It is not clear why the sticking probability increases from 0.69 to 0.75 in the first 0.1 ML, but it is correlated with an increase in heat of adsorption also seen in this same coverage range. We postulate that both effects are due to the electronic stabilizing effects of small amounts of reacted polymer and Ca cyanide on the energy of species nearby, both the transiently adsorbed Ca adatom (which would increase its sticking probability) and the products of that same reaction (which would increase the measured heat).

The heat of Ca adsorption decays nearly exponentially with Ca coverage to the bulk heat of Ca sublimation at both 300 and 130 K, but it does so almost four times faster at 130 K than at 300 K. This is due to the lower diffusion coefficient for Ca into the polymer at lower temperature, [14] which leads to less competition from subsurface Reactions (1) and (2) that have higher heats. At 300 K, LEIS shows that the 3D Ca islands coalesce and form a continuous layer by 15 ML. This occurs already by 9 ML for Ca growth at 130 K. These differences between 130 K and 300 K are also due to the slower Ca diffusion across the polymer surface at 130 K, which generally leads to a higher density of metal clusters per unit area and thus a quicker percolation into a continuous metal film.[84] The combination of this higher density of Ca(s) clusters at 130 K than at 300 K and the slower rate of desorption of transiently adsorbed Ca adatoms (which slows down more than diffusion upon cooling due to the higher activation barrier for desorption than diffusion) leads to a much higher probability that a Ca adatom find an existing Ca(s) cluster at 130 K than at 300 K, explaining the higher sticking probability at 130 K in spite of its much lower probability to diffuse subsurface and react. The net effect of this decrease in probability to diffuse subsurface and the increase in probability to add to Ca(s) clusters, is that less than 20% of the Ca reacts by pathways like Reactions (1) and (2) at 130 K than at 300 K (Fig. 3.7).

The observation that much less of the polymer reacts with Ca at 130 K than at 300 K (Fig. 3.7) implies that devices constructed at low temperatures should have better operational characteristics than those fabricated at room temperature due to the formation of a sharper metal / polymer interface. Previously it has been shown that decreasing the amount of metal atom diffusion into OC_1C_{10}-PPV leads to improved device performance for PLEDs.[14] The decrease in the diffusion in that paper was done by increasing the metal deposition rate leading to more Ca

cluster formation. This may not be the ideal method to limit diffusion if one wants to make a thin uniform layer of Ca. Our results show, in agreement with previous work on another polymer,[82] that deposition at low substrate temperature (130 K) greatly limits the amount of Ca that diffuses and reacts with subsurface groups that contain heteroatoms, in this case with -CN and alkoxy groups.

3.5 Conclusions

The interface formation of Ca onto MEH-CN-PPV was studied by microcalorimetry, LEIS, and XPS. Ca deposited on the surface can desorb, diffuse and react with nitrogen contained in cyano groups of MEH-CN-PPV, or bond with other Ca atoms to form 3D islands. At low coverages (<1 ML) of Ca, desorption or reaction with the polymer –CN or alkoxy groups are the predominant processes. After 4 ML of Ca coverage, the heat of adsorption is equal to the heat of sublimation of Ca and Ca grows on the surface as 3D islands. At 300 K, the surface is fully covered by Ca at a coverage of 15 ML. Based on the XPS data, we proposed a possible reaction of Ca with MEH-CN-PPV. The proposed dominant reaction has Ca removing two cyano groups and forming $Ca(CN)_2$ and cross-linking polymer chains. The experiments at 130 K show that the reaction can be suppressed by depositing Ca onto cold MEH-CN-PPV. Depositing at low temperatures significantly decreases the subsurface diffusion / reaction of Ca, thus increasing the growth of Ca(s) on the surface. Low temperature deposition also decreases Ca desorption and thus increases the sticking probability. The effective thickness of the reacted polymer is estimated to be 5.6 nm (7 monomer layers) at 300 K but only 1.0 nm (1.2 monomer layers) at 130 K.

Acknowledgments

The authors would like to thank Prof. David Ginger for insightful discussions and use of his spin coater. C.T.C. and J.C.S thank the US National Science Foundation for financial support under CHE-1010287. J.M.G. thanks the Deutsche Forschungsgemeinschaft (DFG) for financial support through Sonderforschungsbereich (SFB) 1083. F.B. and J.M.G. thank the Deutscher Akademischer Austauschdienst (DAAD) for support through the PPP-USA contracts D/06/29404 and D/08/11868.

3.6 Figures

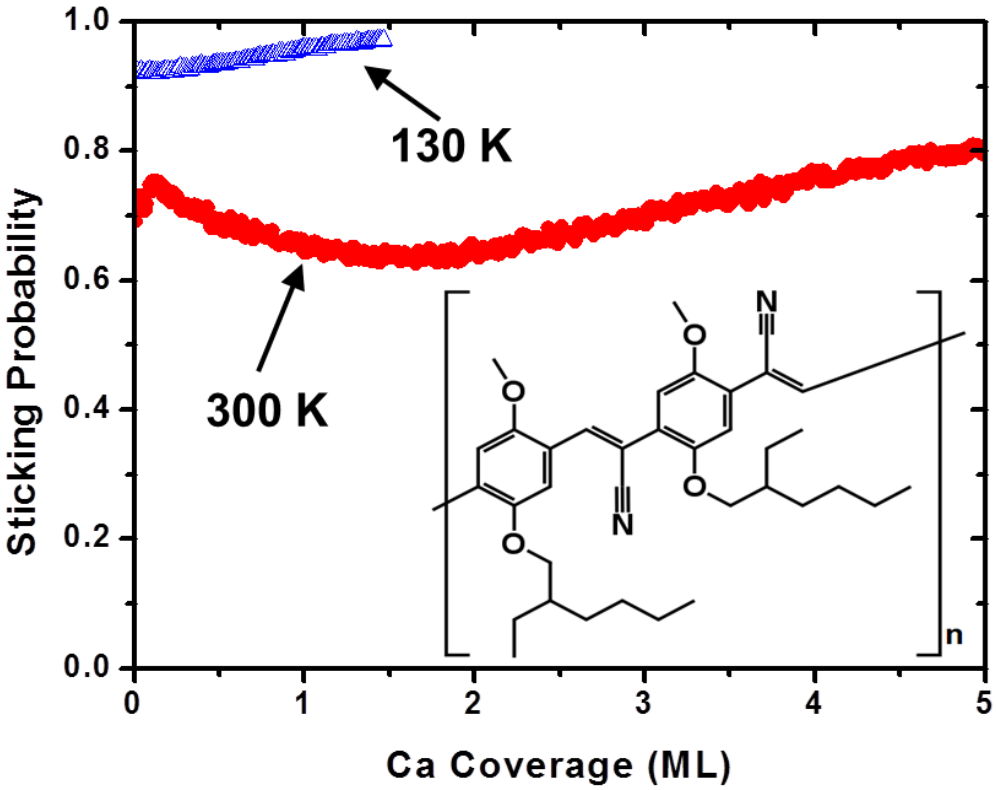

Figure 3.1 Sticking probability of Ca on MEH-CN-PPV at 130 K and 300 K plotted as a function of Ca coverage. One monolayer is defined as 7.4×10^{14} Ca atoms per cm^2, the Ca(111) packing density. The insert shows the structure of the repeat unit of the polymer.

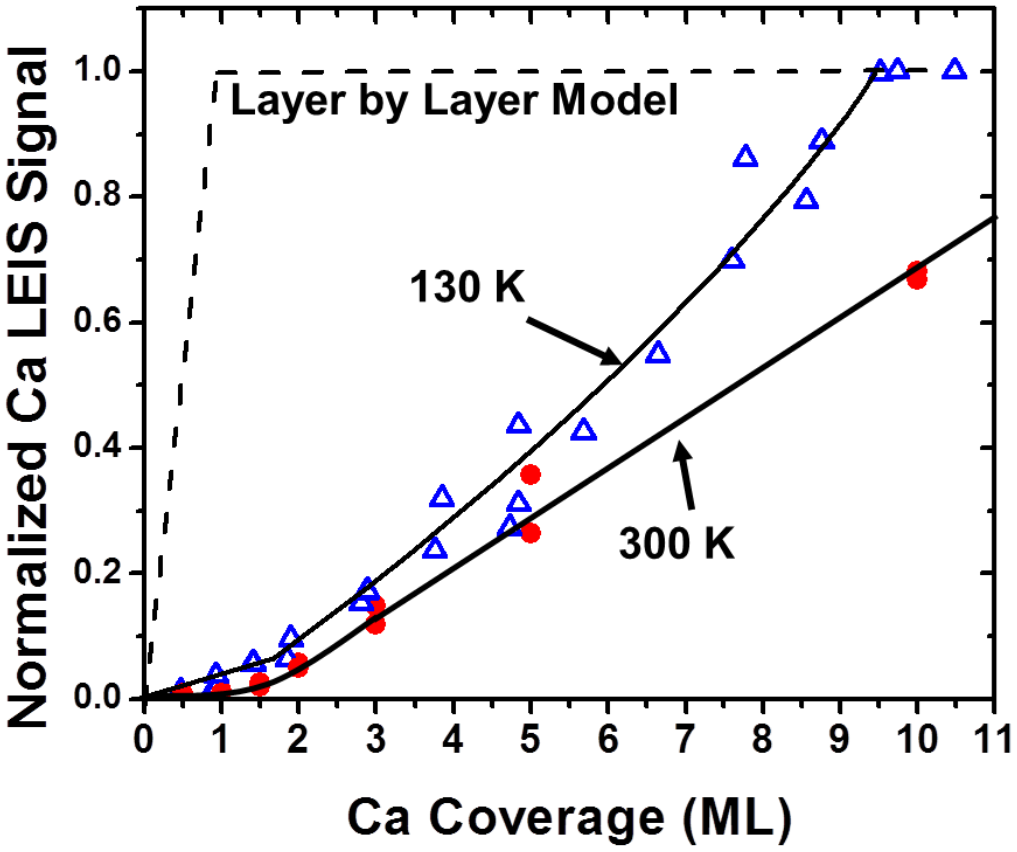

Figure 3.2 He^+ LEIS measurements of Ca on MEH-CN-PPV at 130 K and 300 K. The normalized integrated Ca ISS peak intensity is displayed as a function of Ca coverage. All intensities were normalized with respect to the saturation signal obtained for very high Ca coverages. The black dashed line indicates the expected trace for layer-by-layer growth. The solid lines are drawn to aid the reader and do not represent a fit to the data.

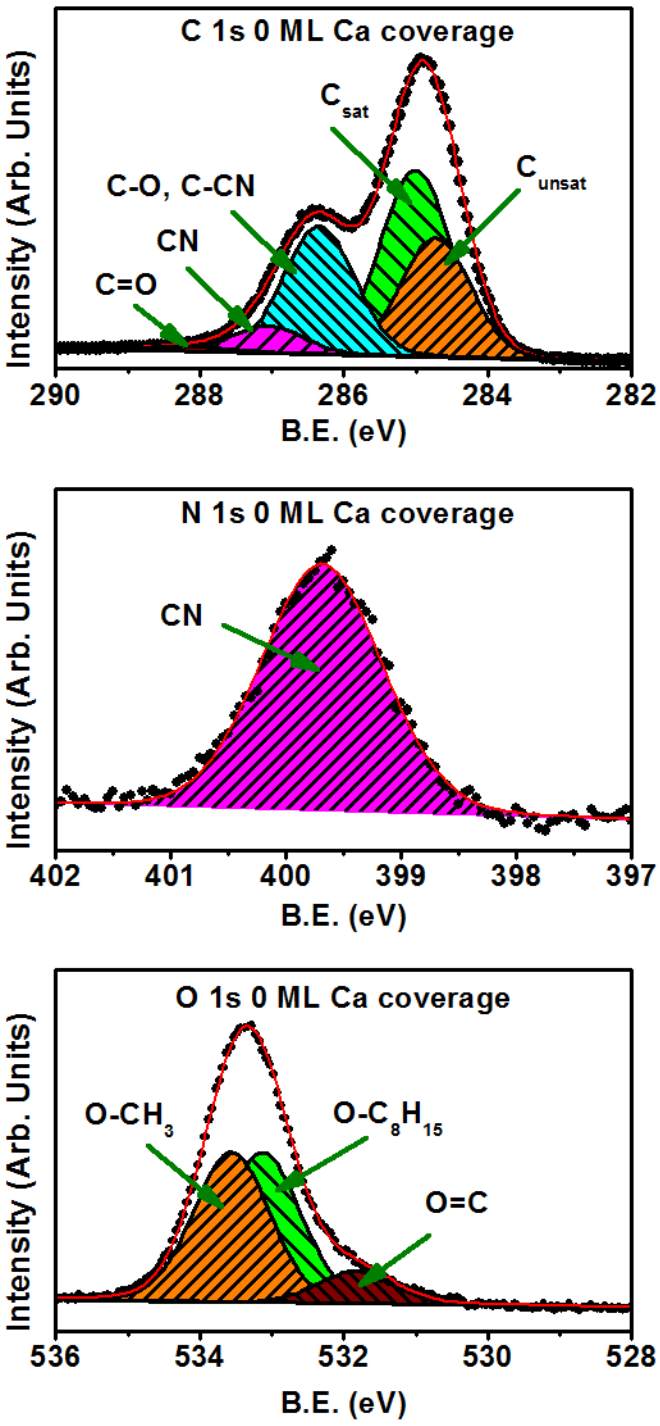

Figure 3.3 XP spectra of the C 1s, N 1s, and O 1s regions on clean, Ca-free MEH-CN-PPV recorded with a photon energy of 1486.6 eV. The C and O spectra are deconvoluted into individual contributions as described in the text.

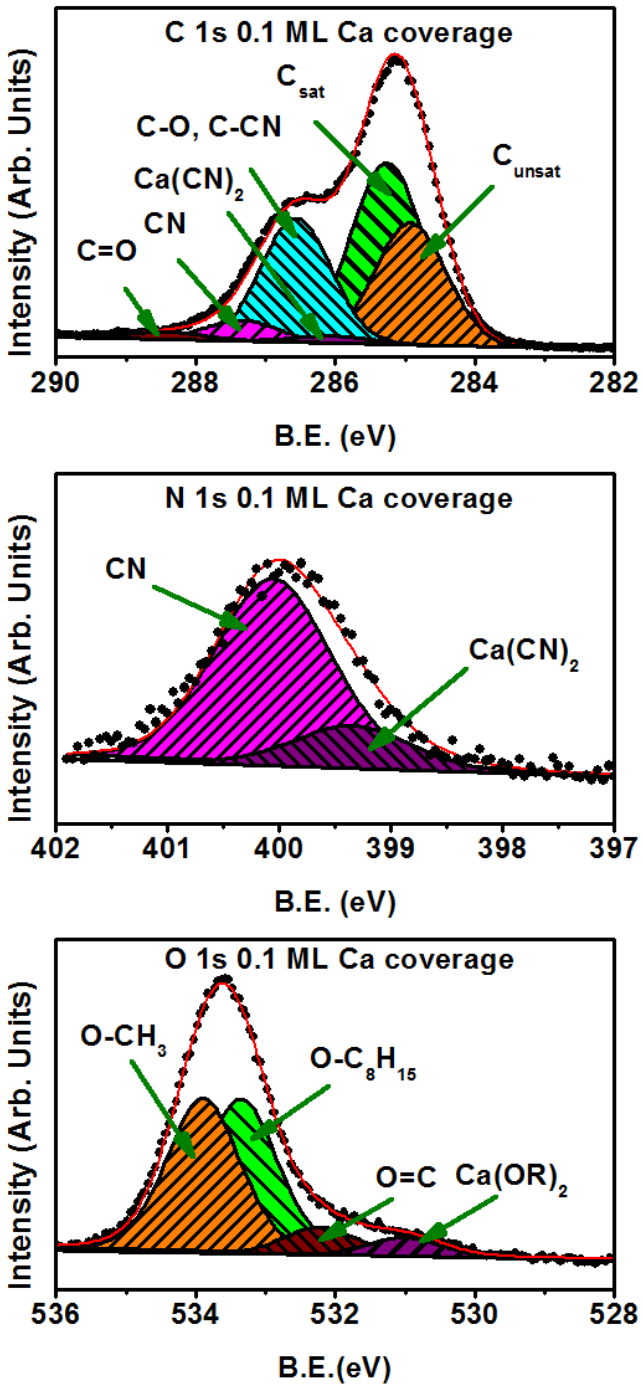

Figure 3.4 XP spectra of the C 1s, N 1s, and O 1s (b) regions for 0.1 ML Ca coverage on MEH-CN-PPV recorded with a photon energy of 1486.6 eV. The formation of new peaks at 286.0 and 399.3 eV are attributed to the formation of $Ca(CN)_2$, and the new peak at 531.0 eV is attributed to Ca alkoxide formation.

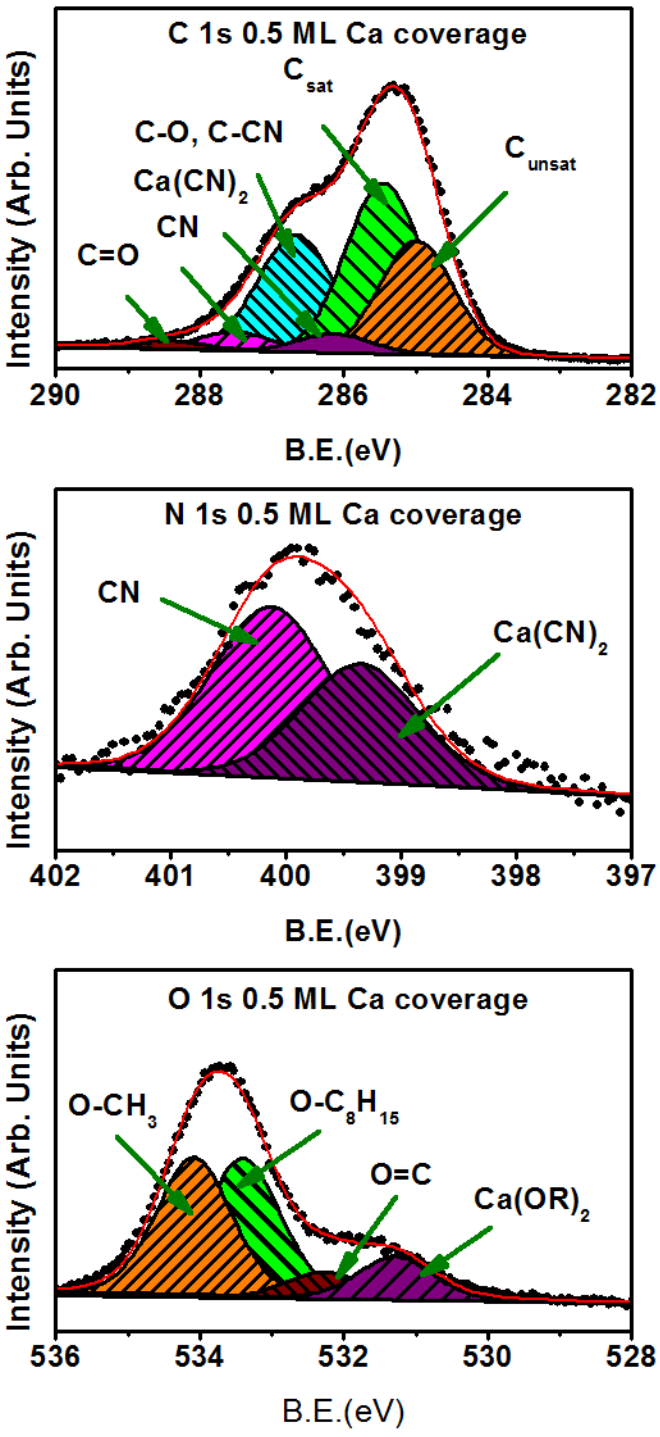

Figure 3.5 XP spectra of the C 1s, N 1s, and O 1s (b) regions for 0.5 ML Ca coverage on MEH-CN-PPV recorded with photon energy of 1486.6 eV. The $Ca(CN)_2$ and $Ca(OR)_2$ peaks increase in intensity relative to the other peaks present.

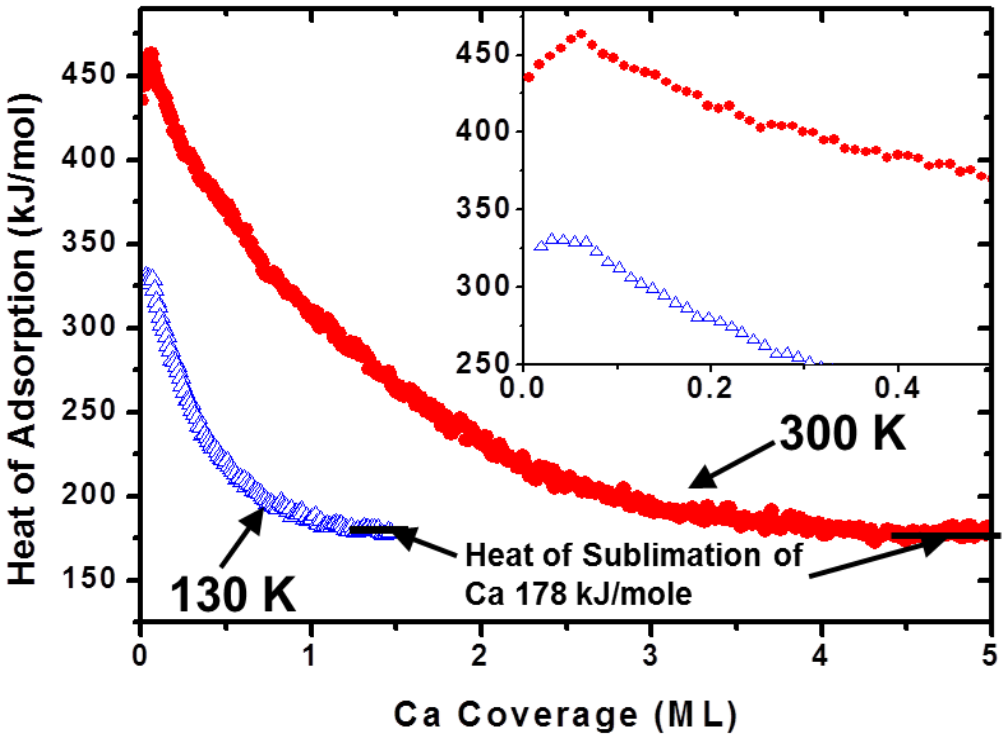

Figure 3.6 The differential heat of adsorption of Ca atoms on MEH-CN-PPV at 130 K and 300 K as a function of Ca coverage. The sublimation enthalpy of Ca, ΔH_{sub}, is displayed as a solid line. The insert shows the low coverage region up to 0.5 ML.

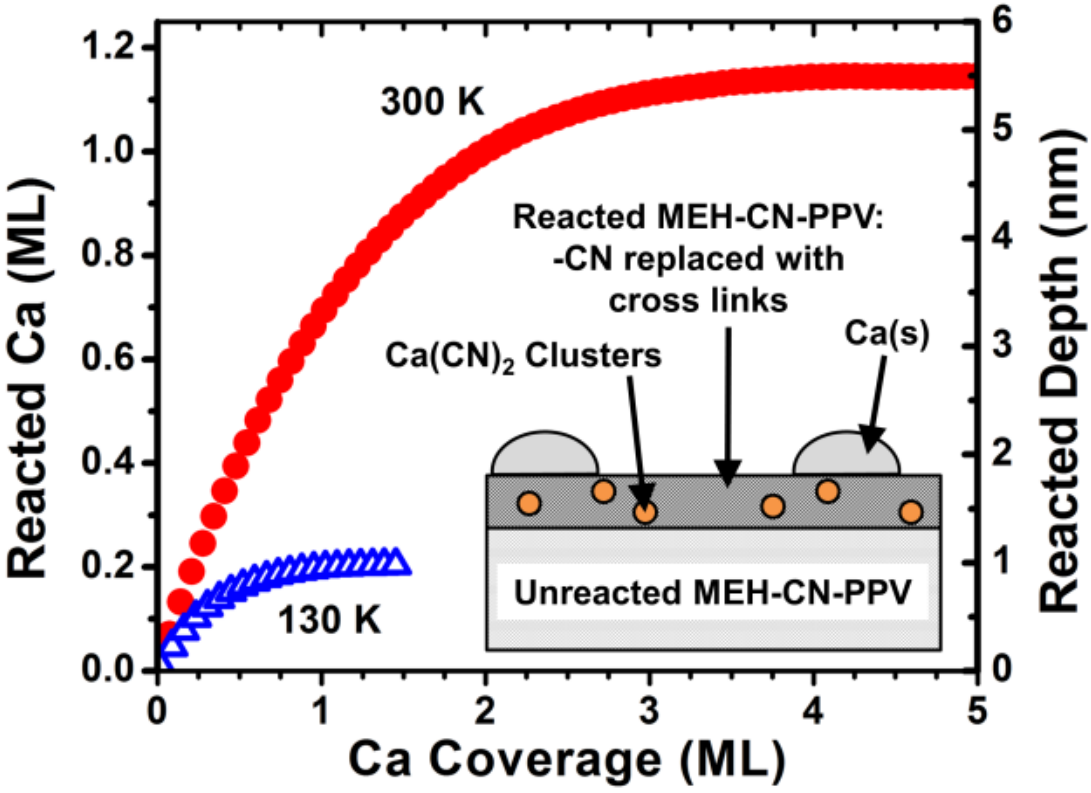

Figure 3.7 The amount of Ca that reacts with subsurface –CN and ether groups of MEH-CN-PPV plotted versus Ca coverage at 300 K and 130 K. The depth of reacted polymer is also shown on the right-hand axis, saturating at 5.6 nm at 300 K but limited to only 1.0 nm at 130 K. Also shown is a schematic of the Ca / polymer interface formed at the highest coverage plotted here.

Chapter 4 Calcium Thin Film Growth on Polyfluorenes: Interface Structure and Energetics

J.C Sharp,[†] X.F. Feng,[£] J.A. Farmer,[†] Y.X. Guo,[£] F. Bebensee,[‡,∥] J.H. Baricuatro,[†] E. Zillner,[‡] J.F. Zhu,[†£,*] H.-P. Steinrück,[‡] J.M. Gottfried[‡§] and C.T. Campbell[†,*]

[†]*Department of Chemistry, University of Washington, Seattle, Washington 98195-1700, USA*

[£]*National Synchrotron Radiation Laboratory, University of Science and Technology of China, Hefei 230029, China*

[‡]*Lehrstuhl für Physikalische Chemie II and Interdisciplinary Center for Molecular Materials, Universität Erlangen-Nürnberg, Egerlandst. 3, 91058 Erlangen, Germany*

[∥]*Institut für Funktionelle Grenzflächen (IFG), Karlsruher Institut für Technologie (KIT), Hermann-von-Helmholtz-Platz 1, D-76344 Eggenstein-Leopoldshafen, Germany*

[§]*Fachbereich Chemie, Philipps-Universität Marburg, Hans-Meerwein-Str., 35032 Marburg, Germany*

Abstract

The adsorption of Ca vapor on two polyfluorenes, poly(9,9-di-*n*-hexyl-2,7-fluorene (PDHF) and poly(9,9-di-*n*-hexyl-2,7-fluorene vinylene (PDHFV), has been studied by adsorption microcalorimetry, low-energy He^+ ion scattering spectroscopy (LEIS), and ultraviolet and X-ray photoelectron spectroscopies (UPS and XPS) at surface temperatures between 130 and ~400 K. At 300 K, the initial heat of adsorption of Ca on PDHF is 250 kJ/mol and on PDHFV is 315 kJ/mol. We ascribe this initial heat to Ca reacting with impurities or defects in the polymers.

The heat of adsorption for both polymers decreases nearly exponentially to the sublimation enthalpy of bulk Ca solid (178 kJ/mol) by 0.75 ML. The observed behavior is attributed to the increasing probability of Ca finding and adding to solid three-dimensional Ca islands which nucleate and grow on the polymer surface, and eventually grow into a continuous solid Ca film on top of the polymer. LEIS, which shows only a slow increase of the signals related to solid Ca, supports this model. Incoming Ca atoms are subject to a kinetic competition between diffusing into the polymer to react with subsurface defects or impurities versus adding to the three-dimensional Ca clusters on the surface. For studies done at 140 K, a similar behavior is observed, with the heat of adsorption starting lower and decreasing more quickly to the heat of sublimation, already by 0.1 ML Ca coverage. This behavior, along with the quicker growth of Ca on the surface of the polymer, is attributed to the slower diffusion of Ca adatoms to subsurface defects/impurities at 140 K than at 300 K. The opposite effect is observed when studied at 400 K. Calcium induces a downward band bending and work function decrease on both polymers, consistent with transfer of electrons from Ca to the polymers.

4.1 Introduction

The interfaces formed between metals and semiconducting, π-conjugated polymers play an important role in organic electronic devices, such as organic light emitting diodes (OLEDs)[1], solar cells[2], and photodiodes.[3] One group of polymers that are of interest for these devices are polyfluorenes, which are relevant due to their blue electroluminescence and thermal stability.[29,31,85,86] Two of the simplest polyfluorenes are poly(9,9-di-*n*-hexyl-2,7-fluorene (PDHF) and poly(9,9-di-*n*-hexyl-2,7-fluorene vinylene (PDHFV) (see Fig. 4.1 for structures). In

photovoltaic and OLED devices based on such polymers, it is often necessary to use a thin film of a low work function metal at the metal/polymer interface to tune the energy level alignment between the electrode and the polymer.[8] Calcium is a commonly used metal in these applications,[27,85-88] often protected by an overcoat of a less reactive metal like Al. Thus, the Ca interfaces to PDHF and PDHFV are interesting from the point of view of OPV and OLED devices. They also serve as prototype systems for the investigation of all metal / polymer interfaces between alkaline earth metals and polyfluorenes. Here we study the formation, structure and interfacial bonding energetics of thin, vapor-deposited calcium films as they grow on clean surfaces of PDHF and PDHFV.

Adsorption microcalorimetry was used to measure the heat of Ca atom adsorption as a function of Ca coverage, and He^+ low energy ion scattering spectroscopy (LEIS) was used to determine the fraction of the polymer surface covered by Ca during growth of the calcium film. X-Ray Photoelectron Spectroscopy (XPS) was used to study film morphology and the electronic character of the Ca, which was also studied by Ultraviolet Photoelectron Spectroscopy (UPS).

To our knowledge, no other studies on the formation of Ca / PDHF or Ca / PDHFV interfaces using LEIS, other surface analysis techniques or adsorption microcalorimetry have been reported. Poly(9,9-dioctyfluorene) (PFO) is identical to PDHF, except that the hexyl groups in PDHF are replaced with octyl groups in PFO. PFO has been widely studied for use in blue emitting OLEDs[27-30] and in blends for solar cells.[31,32] The interface between Ca and PFO has been previously studied by XPS and UPS.[27,33] We find very similar behavior in the XPS and UPS spectra for Ca on both PDHF and PDHFV as reported there for Ca on PFO: Ca induces a decrease in work function and a downward band bending, and gives rise to UPS peaks in the band gap which we interpret here as due to Ca clusters and eventually bulk-like metallic Ca.

The two polymers PDHF and PDHFV differ only by the inclusion of vinylene in the backbone of PDHFV not present in PDHF. Previous theoretical[34] and experimental[16,18] work on poly(*para*-phenylene-vinylene) (PPV) has suggested that the vinylene moiety could be a reactive site for Ca. It should be noted that the PPV derivatives used in those two experimental studies[16,18] had oxygen-containing side groups, while PDHF and PDHFV only consist of carbon and hydrogen. More recent theoretical studies of Ca / PPV without these oxygen-containing side groups show very weak interaction between Ca and the polymer chain.[19]

We find that Ca atoms bind very weakly to these polymer surfaces at 300 K, with the heat of adsorption quickly approaching the heat of sublimation of bulk Ca(s) when only a small fraction of the surface is covered by Ca. We interpret this as due to the rapid formation of thick three-dimensional (3D) Ca(s) particles covering a small fraction of the polymer surface. There is also a high initial heat of reaction for Ca vapor which we attribute to reactions with some subsurface impurity such as residual solvent (chloroform) or polymer chain end-groups. The extent of this reaction is very small, and it can be almost completely suppressed by holding the polymer at 140 K during Ca deposition, or enhanced by deposition above 300 K.

4.2 Experimental

The PDHF and PDHFV polymers were obtained from Sigma Aldrich (purity verified by manufacturer using proton NMR and infrared spectra) and used without further purification. Solutions of 0.5 % w/w polymer in chloroform were prepared and 120 μL was spin-coated directly onto the pyroelectric material used for heat detection at 2000 rpm for 30 s. This yielded a film thickness of ~100 nm, consistent with expectations based on prior work.[61] The film thickness was determined by spin coating the polymer onto a glass slide in exactly the same way,

removing some of the film with a razor blade, and measuring the film height with a profilometer. The samples were immediately transferred to the sample preparation chamber, pumped down to its base pressure of 8 x 10^{-9} Torr and outgassed by heating the polymer at 330 K for ~10 hours to remove trace amounts of solvent. The samples were then transferred into the ultrahigh vacuum (UHV) analysis chamber when needed. No remaining solvent was detected with Auger Electron Spectroscopy (AES).

The UHV system used in these experiments had a base pressure 2 x 10^{-10} Torr and was equipped with a hemispherical energy analyzer (Leybold-Heraeus EA 11/100) for low energy ion scattering spectroscopy and Auger electron spectroscopy, an ion gun (Leybold-Heraeus IQE 12/38), a quartz crystal microbalance (QCM, Inficon), a quadrupole mass spectrometer (UTI 100C), and an adsorption microcalorimeter. This analysis/calorimetry chamber and the pulsed metal atom beam have been described previously.[58] The Ca atomic beam was chopped into 100 ms long pulses which contained ~0.02 ML of Ca at a rate of 0.5 Hz. One monolayer (ML) of Ca is defined here as the Ca(111) packing density, 7.4 x 10^{14} Ca atoms per cm^2. The metal atom microcalorimetry method used in these experiments has been described in detail previously.[20,59] The heat detectors for the calorimeter were 1.3 cm diameter disks cut from a 9 μm thick sheet of β-polyvinylidene fluoride (PVDF) coated on both sides with ~60 nm films of nickel-aluminum that serve as the two electrodes for heat signal measurements (as purchased from Measurement Specialties, Inc.).

The procedure for the calorimetric experiments at elevated or liquid nitrogen temperatures is described in detail elsewhere.[62] Briefly, the temperature of the sample was controlled by flowing dry nitrogen either through liquid nitrogen for cooling, or through a heated

tube for elevated temperature, and then through the thermal reservoir of the calorimeter. The temperature was monitored by a thermocouple spot welded to the calorimeter.

The sticking probability for Ca on PDHF and PDHFV was determined using a quadrupole mass spectrometer (QMS) with the modified King-Wells method described previously.[58] A metal mesh placed between the QMS and the sample was biased at negative 500 volts to avoid any electron damage on the sample.

The growth of Ca on PDHF and PDHFV was studied by LEIS, using $^4He^+$ ions with a primary energy of 1.00 keV and an angle of 45° between the ion source and analyzer axis (i.e., scattering angle = 135°). Ion fluxes were typically 100 nA/cm^2 with a total ion dose of 6 μC/cm^2 per experimental run.

The XPS measurements were carried out in an UHV system which has been described in detail elsewhere.[89] Briefly, the system contains two UHV chambers: an analysis chamber and a sample preparation chamber, whose base pressures are 6×10^{-11} and 1×10^{-10} mbar, respectively. The analysis chamber is equipped with a hemispherical electron analyzer, a SPECS twin anode X-ray source, and a quadrupole mass spectrometer (Pfeiffer QMG 220). The preparation chamber is connected to a sample load-lock system and comprises LEED optics, a cold-cathode ion gun for sample cleaning, and several evaporators. The C 1s and Ca 2p XPS spectra were acquired using a Mg Kα source (hυ = 1253.6 eV) with overall energy resolution of ~0.9 eV at normal emission.

The UPS and work function measurements were conducted using synchrotron radiation with a photon energy of 25 eV. The detailed description of the endstation and beamline can be found elsewhere.[12] For work function measurements, a bias voltage of -6 V was applied to the sample in order to allow the observation of the secondary electron cut-off.

4.3 Results

Ca adsorption on pristine PDHF and PDHFV at 300K.

Sticking Probability. Figure 4.1 shows the sticking probability of Ca on PDHF and PDHFV at 300 K as a function of Ca coverage. The flux of the Ca atomic beam was measured by the calibrated QCM. The Ca coverage was determined by time-integrating the product of the Ca flux times the sticking probability, taking into consideration the chopped Ca beam's "on" time. Each curve in the figure is the average of 3 independent runs.

For Ca on PDHF at 300 K, the sticking probability starts at 0.41 and increases asymptotically towards unity. For Ca on PDHFV at 300 K, the initial sticking probability is 0.53. Then in the low coverage range from 0 to 0.1 ML the sticking probability increases rapidly to 0.60 at 300 K. Between 0.1 and 0.3 ML, the sticking probability decreases to 0.55. After 0.3 ML the sticking probability increases asymptotically towards unity.

The lineshape of the Ca mass spectrometer signal versus time for the atoms which did not stick at 300 K was analyzed and the lack of pulse broadening indicated that they had negligible surface residence time (<10 ms). Assuming that these atoms which did not stick permanently were nevertheless transiently adsorbed as monomers on the polymer surface, this short residence time suggests that they were bonded very weakly to the polymer. Assuming a pre-exponential factor for desorption of 10^{13} s^{-1} at 300 K based upon our entropy approach,[64] this short residence time requires a desorption energy below 64 kJ/mol.

LEIS and XPS. When metal is vapor deposited onto a polymer film, the metal atoms can form 3D islands or a continuous film on the surface, or diffuse below the surface and react with functional groups of the polymer.[12,13,20,65-69,90,91] LEIS using He^+ is a valuable tool for

determining growth modes since it is only sensitive to the topmost atomic layer of the surface, and is element specific. XPS is a quantitative elemental analysis and chemical sensitive technique that also elucidates the growth morphology, but it probes five to ten times deeper than LEIS. Knowledge of the growth mode is essential in the interpretation of the heat of adsorption of Ca on these polymers.

Figure 4.2 shows the evolution of the normalized Ca LEIS signal on PDHF and PDFHV at 300 K. Sample degradation by exposure to the He^+ ion beam was determined to be negligible by comparing measurements with shorter acquisition times, yielding similar results. As shown in Fig. 4.2, Ca grows slower on the surface than would be expected for a layer-by-layer growth mode at all temperatures. Below 0.5 ML for both polymers at 300 K, the Ca LEIS signal grows at a rate that is less than 5% of that expected for layer-by-layer growth. This will be attributed to Ca diffusing below the surface and binding to subsurface reactive site(s) which, as we show below, also give higher heats of adsorption. This assignment is based on similar behavior observed with other polymer systems we have studied.[12,20,82] The faster growth rate after 0.5 ML but not as fast as a layer-by-layer model is indicative of Ca forming 3D islands on the surface, also consistent with the heat of adsorption being very close to the heat of sublimation of pure Ca(s). The Ca LEIS signal does not reach its maximum intensity until ~ 30 ML of Ca coverage, showing that these 3D islands of Ca(s) grow thicker as the coverage increases, while their footprint parallel to the surface only grows slowly, and that patches of Ca-free polymer surface persist even when the Ca islands are >20 ML thick.

The C 1s XPS intensity for both PDHF and PDHFV decreased more slowly with Ca coverage than expected based on a layer-by-layer growth model. Using an estimated electron mean free path of 3.4 nm for the 968 eV kinetic energy of these photoelectrons through Ca,[92] the

average slope of the C 1s intensity (relative to its starting intensity) versus Ca coverage from 0 to 5 ML is predicted to be -0.080 per ML for layer-by-layer growth. The measured average slope was only -0.031 per ML for PDHF and -0.028 per ML for PDHFV at 300 K. This is consistent with the LEIS results, which suggest that Ca(s) grows as thick islands that cover only a small fraction of the polymers.

Heat of Adsorption. Figure 4.3 shows the differential heat of adsorption of Ca on PDHF and PDHFV at 300 K as a function of Ca coverage. Each of the curves is the average of three independent runs. The measured heats plotted here were corrected for gas velocity as described previously,[58] so that they represent the standard enthalpies of adsorption at 300 K. For Ca on PDHF, the initial heat of adsorption is 250 kJ/mol at 300 K. As shown, the heat of adsorption decreases from its initial value until ~0.25 ML, where it reaches within 4 kJ/mol the heat of sublimation of bulk Ca(s), ΔH_{sub}, = 178 kJ/mol[93], and remains steady thereafter. For Ca on PDHFV, the initial heat of adsorption is 315 kJ/mol at 300 K. The heat of adsorption also decreases until ~0.8 ML, where it reaches ΔH_{sub} within 4 kJ/mol, and remains steady thereafter.

The initial heat of adsorption is high and rapidly decreases with coverage below 0.25 ML for both polymers. This behavior can be explained by a simple two-state model, where Ca can either react to make some state with a high heat or make Ca(s) with a heat equal to ΔH_{sub}. The decrease in heat with coverage is due to the consumption of sites on or below the polymer surface that give rise to the high-heat state by Ca. According to this model and the data of Fig. 4.3, the maximum amount of Ca that reacts in the high-heat state is less than 0.06 ML for both polymers (see Discussion). Polymers that have heteroatoms in their repeat unit have been shown to have a much greater extent of high-heat reaction with Ca, with between 1.2 and 1.6 ML of reacted Ca reported for poly(methyl methacrylate),[20,90] a polythiophene,[12,82] and a cyano-

poly(phenylene vinylene).[91] In all these cases, the high-heat reaction was proven to be due to bond-breaking reactions near the heteroatoms, which are below the polymer surface. The extent of reaction is 20 to 26-fold less here, suggesting instead some reaction with minority species, either impurity or defects in the polymer, that contain heteroatoms. We therefore attribute the high initial heat to the reaction of Ca with some low concentration of subsurface defects in the polymers or some impurity like residual solvent.

No impurities were observed by XPS on the starting polymers' surfaces. The presence of residual solvent or other impurities was checked also by AES on both the starting and Ca-reacted polymers. No chlorine could be detected within the probe depth of AES. However, the downward diffusion of Ca below the AES or XPS probe depth could allow more impurity to react than that detected in AES or XPS, and the amount of Ca that reacts with high heat is tiny (<0.06 ML). So this does not rule out reaction with impurities as the high-heat process.

For PDHFV, Ca reaction with the vinylene moiety has also been suggested as a possibility,[16,18,34] but the low extent of Ca reaction relative to the large number of vinylene groups present within the probe depth suggests this reaction does not occur. Also, XPS shows no evidence for such a reaction with C atoms in the polymer (see below). Finally, quantum mechanical calculations show that Ca has very weak interactions with pure hydrocarbon functionalities even when these have C=C bonds.[12,19]

After all these defect or impurity sites have been reacted, the dominant reaction is Ca binding to Ca(s) clusters, with the expected heat of adsorption of 178 kJ/mol.

Ca adsorption on PDHF and PDFHV at different temperatures. Our experimental apparatus allows for the study of metal growth on polymer surfaces at various temperatures.

Previous work has shown that significant diffusion of Ca into the polymer surfaces occurs at 300 K.[14] By lowering the temperature of the polymer surface, we can limit the extent of diffusion of Ca in the polymer.[82]

Sticking Probability. Figure 4.4 shows the sticking probability of Ca on PDHF at 140, 300 and 370 K, and on PDHFV at 140, 300 and 410 K, as a function of Ca coverage. The initial sticking probability increases with decreasing temperature. As shown below, the initial heat of adsorption does just the opposite, decreasing with decreasing temperature. In general, the sticking probability increases with decreasing temperature for both polymers, except for PDHF at coverages above 0.15 ML at 370 to 300 K, where the sticking probability is slightly larger at 370 K.

For Ca on PDHF, all curves exhibit the same basic shape, that is, they start at an initial sticking value and increase asymptotically towards unity. The initial sticking probability is 0.93 at 140 K, 0.41 at 300 K and 0.32 at 370 K. The sticking probability at 330 K increases faster than at 300 K and then slows its rate of increase around 1.0 ML.

For Ca on PDHFV, the sticking probability at 140 K is similar to that of PDHF. It has an initial value of 0.94 and increases asymptotically towards unity. At 300 and 410 K, the sticking probabilities start at 0.53 and 0.46 respectively. Then in the low coverage range from 0 to 0.1 ML the sticking probability increases rapidly to 0.60 at 300 K and 0.55 at 410 K. Between 0.1 and 0.5 ML, the sticking probability decreases to 0.55 at 300 K and 0.50 at 410 K. After 0.5 ML both curves increase asymptotically towards unity.

Low Energy Ion Scattering. Figure 4.5 shows the evolution of the normalized Ca LEIS signal on PDHF at 140, 300 and 370 K, and on PDFHV at 140, 300 and 410 K. At 370 or 410 K, the Ca signal increases with coverage in almost the same way on both polymers as that shown in

Figure 4.2 for 300 K, which was already discussed. At 140 K, the Ca signal grows at a higher rate than at those elevated temperatures, but is still much slower than the layer-by-layer model, again indicative of Ca growing as 3D islands of Ca(s) on the surface even up to quite high coverages. At 300 K and higher, the Ca LEIS signal does not reach its maximum intensity until ~ 30 ML of Ca. For the measurement taken at 140 K, the Ca LEIS signal grows at a much faster rate, reaching nearly the maximum signal intensity already below ~10 ML for both polymers.

Heat of Adsorption. Figure 4.6 shows the differential heat of adsorption of Ca on PDHF at 140, 300, and 370 K, and on PDHFV at 140, 300 and 410 K, as a function of Ca coverage. Each of the curves is the average of three independent runs. The measured heats represent the standard enthalpies at the given temperatures.

For Ca on both polymers, the heats decrease quickly with Ca coverage. Both the initial heat of adsorption and the Ca coverage at which the heat drops below 190 kJ/mol (i.e., within 7% of ΔH_{sub}) decrease rapidly with decreasing temperature. We attribute this to the slower rate of diffusion of Ca into the polymer with subsurface reaction at lower temperature, relative to its rate of non-activated nucleation and growth into 3D Ca clusters on the surface.

For Ca on PDHF, the initial heats are 192 kJ/mol at 140 K, 250 kJ/mol at 300 K, and 269 kJ/mol at 370 K. For Ca on PDHFV, the initial heats are 263 kJ/mol at 140 K, 315 kJ/mol at 300 K, and 698 kJ/mol at 410 K. The initial heats are much larger for PDHFV than PDHF, especially at elevated temperatures.

After the defect or impurity sites have been reacted with, the primary reaction occurring is Ca binding to Ca. This should lead to an expected heat of adsorption of 178 kJ/mol. Instead, the heat of adsorption is lower than expected. This is related to the size of the Ca islands formed. Smaller metal particles are known to have lower heats of adsorption than the bulk values.[78].

After 1.0 ML, the Ca islands are large enough such that the heat of adsorption approaches the heat of sublimation of Ca. At elevated temperatures, this behavior is not seen because it is hidden by the greater extent of reaction with subsurface defects or impurities.

The large increase in the initial heat of adsorption at 370 K for PDHF and 410 K for PDHFV is attributed to Ca reacting with more subsurface defects or impurities at higher temperatures. Since both Ca and impurities can diffuse faster at higher temperature, one expects a greater extent of such reactions. The higher initial heat for PDHFV at 410 K than for PDHF at 370 K could be due to a combination of the higher temperature and differences in solubility and mobility of Ca and the impurity in the different polymers, or differences in the chemical nature of their defects or end-groups.

UPS, Work Function, XPS and Band Bending Measurements

Figure 4.7 shows the evolution of the UPS spectrum with increasing Ca coverage on both PDHF and PDHFV at 300 K. The spectra show a new feature in the 0-3 eV binding energy (B.E.) range that grows with Ca coverage and shifts towards lower B.E.. This is characteristic of the nucleation of small metal clusters that grow in size. The Ca-induced feature very slowly evolves to that characteristic of the bulk metal, which is characterized by its intensity cutoff at the Fermi edge (0 eV B.E.).[35] A similar behavior was observed for Ca on another polyfluorene, PFO.[27]

The onset of the secondary electron distribution in these UP spectra was used to measure the change in work function with Ca coverage, as shown in Fig. 4.8 for PDHF and Fig. 4.9 for PDHFV. As can be seen, the work function decreases by a total of ~0.8±0.1 eV in both cases,

decreasing more quickly at first but then leveling off after 0.6 ML for PDHF and 1 ML for PDHFV.

These figures also show the effect of Ca adsorption on band bending, measured by the shift in the centroid of the C 1s XPS peak. Band bending induced by metal adsorption on semiconductor surfaces reflects the change in the long-range dipole moment at the surface associated with transfer of charge from the adsorbate into the carrier depletion or accumulation layer.[35] The 0.2 to 0.3 eV increase in the C 1s B.E. (i.e., downward band bending) seen upon the addition of 0.1 to 0.2 ML of Ca for both polymers indicates that Ca initially contributes electron density to the polymers' depletion or accumulation layer, and the Ca is slightly positively charged below 0.1-0.2 ML. Thereafter, there is not much change, which means that long-range charge transfer is not significant at higher coverages. Besides this band bending, there were no new peaks that appeared in the XP spectrum upon Ca adsorption nor was any new shoulder seen on the single C 1s peak that might suggest specific reactions of Ca with selected C atoms in either polymer. Thus, the UPS and XPS data indicate that adsorption of Ca at low coverages induces a decrease in work function and a downward band bending on both PDHF and PDHFV. Similar work function changes and band bending have been observed for Ca on PFO, another polyfluorene.[27]

The sum of the work function and band bending values is also shown in Figs. 4.8 and 4.9. The slope of this band-bending-corrected work function, or sum curve directly reflects changes in the local surface dipole.[35] This is exactly what is measured by work function changes alone on metal substrates, so it can be interpreted in the same way that adsorbate-induced work function changes are interpreted on metallic surfaces. Thus, the magnitude of the slope gives the local dipole moment for the adsorbate-substrate complex, using the Helmholtz equation. This

sum stays nearly constant or increases slightly in the first 0.1 ML, and then decreases rapidly until it levels off ~0.4 eV below the starting value. This steep decrease indicates transfer of electron density from Ca to nearby atoms on the polymer surface, so that the adsorbed Ca is slightly positively charged when the slope is most negative (i.e., in the 0.1 to 0.5 ML coverage range). At higher coverages, the Ca that adsorbs is essentially neutral, consistent with the growth of Ca(s) as the only significant process above ~0.5 ML. The Ca 3p XPS peak's lineshape eventually shows the strong plasmon losses expected for metallic Ca(s) at higher Ca coverages. Initially, the sum's value is nearly constant in the same coverage range where the heat of adsorption is highest (below 0.1 ML). This is consistent with Ca reacting with subsurface impurities or defects in this coverage range, whereby any dipoles that are formed would have random orientation.

4.4 Discussion

For Ca adsorption on the two studied polyfluorenes, PDHF and PDHFV, four observations are evident:

(1) The initial heat of adsorption is larger than the heat of sublimation of bulk Ca(s) (178 kJ/mol), and it grows rapidly with increasing temperature.

(2) The Ca coverage required to decrease the heat of adsorption to within 10 kJ/mol of this 178 kJ/mol sublimation enthalpy is small and decreases rapidly with decreasing temperature.

(3) No significant new features appear in the C 1s XPS that suggest aggressive reactions of Ca with the polymer.

(4) At 300 K, the Ca LEIS signal remains below 1% of the value expected for layer-by-layer growth (up to ¼ ML for PDHF and ½ ML for PDHFV, which is the coverage range where the heat of adsorption remains substantially larger than ΔH_{sub}.

We propose a simple two-state model that is consistent with these observations, whereby Ca atoms can bind in one of two states A and B: (A) a state associated with some low concentration of subsurface defect or impurity sites that has a high heat of adsorption, ΔH_A, and (B) Ca in 3D Ca(s) particles that have a heat of adsorption approximately equal to the heat of sublimation of bulk Ca(s), ΔH_{sub} = 178 kJ/mol. At high temperature, the Ca initially binds mainly in state A, explaining the low Ca LEIS signal. After these subsurface type A sites are occupied within the diffusion range of Ca, the dominant path of Ca adsorption is to occupy state B and to form the 3D Ca(s) particles.

We now analyze the temperature-dependent heat data in Fig. 4.6 with this simple two-state model where the heat at any coverage is a sum of the heats for producing the two states, each weighted by the fraction of the Ca that sticks in that pulse which adsorbs into each state:

$$\Delta H_{ad} = f_A (\Delta H_A) + (1- f_A) (178 \text{ kJ/mol}).$$

We assume that ΔH_A is the highest heat of adsorption observed for that polymer: 265 kJ/mol for PDHF and 700 kJ/mol for PDHFV. These values could be larger, which means that the fraction that reacts in A sites, f_A, estimated in this way is really an upper limit to the real fraction. This fraction is shown versus coverage for 370 K for PDHF and 410 K for PDHFV in Fig. 4.10. For both polymers, the only reaction occurring is Ca(s) cluster formation (i.e., $f_A = 0$) above 0.75 ML Ca coverage. Multiplying f_A by the amount of Ca that adsorbed in that pulse and integrating with time gives the total amount of "reacted Ca" (i.e., Ca in state A) at that coverage. Also shown in Fig. 4.10 is this amount of reacted Ca versus Ca coverage.

For both polymers, Fig. 4.7 shows that less than 0.15 ML of Ca reacts with polymer even at elevated temperatures. This is only ~5% or less of the amount of Ca that reacts aggressively (i.e., with heats of adsorption much larger than ΔH_{sub}) at 300 K with polymers that have heteroatoms (O, S, N) in their repeat unit, as we previously reported for polymers that contain ester,[20,90] thiophene[12] or cyano groups.[91] In those studies, we found that Ca directly attached to these functional groups that contained heteroatoms, but did not bond strongly to the pure hydrocarbon parts on the polymers, even if unsaturated. This is also consistent with quantum mechanical calculations which show that Ca has very weak interactions with pure hydrocarbon functionalities even when these have C=C double bonds.[12,19]

The high initial heat of adsorption and its very rapid decrease to the negative heat of sublimation of Ca(s) seen for both PDHF and PDHFV corresponds to such a small amount of Ca that we attribute it to some sort of defect site or impurity in the polymer. The most likely reaction occurring is Ca reacting with residual of solvent ($CHCl_3$) or heteroatoms in the polymer chain end-groups that are present in concentrations below the detection limits of AES. That these type A sites (defects or impurities) are subsurface is consistent with our observation that the extent of this reaction is suppressed as the polymer temperature is decreased, such that it is almost completely eliminated by 140 K, and is greatly enhanced when heating the polymer above 300 K. The difference in the initial heat of adsorptions and initial sticking probability between the two polymers is likely due to either Ca being able to more readily diffuse subsurface on PDFHV than PDHF, the presence of a higher concentration of A type sites in PDHFV than PDHF, or defect sites with a larger value of ΔH_A for PDHFV than PDHF. If Ca can diffuse faster in PDHFV, then it can react with more type A sites so that the ratio of A-site to B-site heats will be higher in the first pulses, so the initial heat will be higher, even if the A-site heats

are the same in both polymers. This emphasizes that the initial heat is a lower limit on the A-site heat, so that the reacted amounts and fractions in Fig. 4.10 are really upper limits.

A 4 nm-thick "interface region" was reported to be formed between another polyfluorene (PFO) and a vapor-deposited Ca film on the basis of UPS and XPS measurements and that was proposed to be associated with poor OLED device performance.[27] As noted above, similar trends to those UPS and XPS results for Ca on PFO were observed here for both PDHF and PDHFV. Also reaction with type A sites (defects or impurities) was probably also present in that PFO study, it would not have been seen due to the lack of measurements like calorimetry that are sensitive to this. Our results indicate that that these band bending and work function changes seen in UPS and XPS are related to the reaction with type A sites, since this reaction is most prevalent below 0.2 ML when the band bending and work function changes are the strongest.

The variations in the sticking probability (S) with Ca coverage and temperature on PDHF and PDHFV (Figs. 4.1 and 4.4) can be understood within this two-state model as well. The initial sticking probability represents the intrinsic sticking probability of Ca on that polymer, S_0, which is about 0.4 for PDHF and 0.5 for PDHFV. Initially, adsorption at 300 K is dominated by binding to A sites (Fig. 4.10), so S_0 represents the competition between a transiently-adsorbed Ca atom finding a subsurface A site and binding to it, versus desorbing back into the gas. Finding an A site is slightly more probable on PDHFV, due to either a higher concentration of A sites or slower desorption. The increase of S with coverage (Fig. 4.1) is dominated by the effect of Ca(s) particles (B sites) on S. It is known that S is 1.0 on Ca(s) at 300 K,[23, 26] so that S must increase to 1.0 as the surface gets more and more covered by Ca(s). Thus S should correlate with the fraction of the surface covered by Ca(s), X_{Ca}, which is directly given by the normalized Ca LEIS signal (Fig. 4.2).

Plots of $S-S_0$ versus X_{Ca} for the data in the first Ca monolayer from Figs. 4.1 and 4.2 are shown in Fig. 4.11. These are approximated by directly proportional lines with slopes of 12 for PDHF and 9 for PDHFV, with a maximum deviation in $S-S_0$ from the line of 0.03 for PDHF and 0.05 for PDHFV. These large slopes prove that the increase in S is not simply equal to the increase in the fraction of the surface covered by Ca(s), but instead it increases by 12- and 9-fold that fraction. This is due to the fast diffusion of the transiently adsorbed Ca atom across the surface, which allows them to find the Ca(s) particles, which thus have capture zones that are 12- and 9-fold larger than their actual areas. For PDHFV, S initially increases by 0.05 above the simple proportional model and then decreases below it by a similar amount, but rejoins it already when only ~1% of the surface is coverage by Ca. This oscillation could have many explanations, but since the dominant reaction at the lowest coverage is Ca reacting with subsurface A sites, it probably is due to the effect of that reaction on the binding of Ca atoms to the polymer surface. For example, that reaction may initially make it easier for a diffusing Ca atom to find A sites or lower the barrier for it to react with A sites, possibly due to some cooperative binding, but then, after the A sites in the near-surface region are consumed, the sticking probability drops down to the lower, intrinsic value that would obtain for PDHFV in the absence of any A sites. At higher coverage than shown in Fig. 4.11, S asymptotically approaches its value for Ca(s), 1.0.

As with any adsorbate, decreasing temperature causes Ca adatoms to diffuse more slowly, but to desorb <u>much</u> more slowly. Thus, S should increase with decreasing temperature, as indeed observed: S is much higher at 140 K and lower above 300 K than at 300 K (Fig. 4.4), except for PDHF at 370 K and intermediate coverages, where S is very slightly larger than at 300 K. We have no simple explanation for this small deviation from expectation.

4.5 Conclusions

The formation of interfaces between vapor-deposited Ca and the surfaces of PDHF and PDHFV was studied by microcalorimetry, LEIS, UPS and XPS. Adatoms of Ca deposited on the surface can desorb, diffuse across and into the surface, and react with defects in PDHF and PDFHV, or bond with other Ca atoms on the surface to form 3D islands. At low coverages of Ca (<0.75 ML), reaction with subsurface defects and desorption without sticking are the predominant processes. These defects may be impurities or polymer end groups. After 0.75 ML of Ca coverage, the heat of adsorption is equal to the heat of sublimation of Ca and Ca grows on the surface as 3D islands with UP and XP spectra characteristic of Ca(s). At 300 K, the surface is only fully covered by Ca after 30 ML. The experiments at 140 K show that the reaction with defects can be suppressed by depositing Ca onto cold PDHF or PDHFV. Depositing at low temperatures significantly decreases the subsurface diffusion / reaction of Ca, thus increasing the growth of Ca(s) on the surface. Low temperature deposition also decreases Ca desorption and thus increases the sticking probability. High temperature deposition shows an increase in the initial heat of adsorption due to the increased ability of Ca atoms to diffuse subsurface and react with defects.

Acknowledgments

C.T.C. and J.C.S. thank the US National Science Foundation for financial support under CHE-1010287. J.F.Z. gratefully acknowledges the financial support from the National Natural Science Foundation of China (Grant No.21173200) and the Specialized Research Fund for the Doctoral Program of Higher Education of Ministry of Education (Grant No. 20113402110029).

F.B. and J.M.G. thank the Deutscher Akademischer Austauschdienst (DAAD) for support through the PPP-USA contracts D/06/29404 and D/08/11868. Financial support by the Deutsche Forschungsgemeinschaft (DFG) through Sonderforschungsbereich 1083 is gratefully acknowledged. H.-P.S. thanks the Cluster of Excellence 'Engineering of Advanced Materials' (www.eam.uni-erlangen.de) at the Universität Erlangen-Nürnberg for support.

4.6 Figures

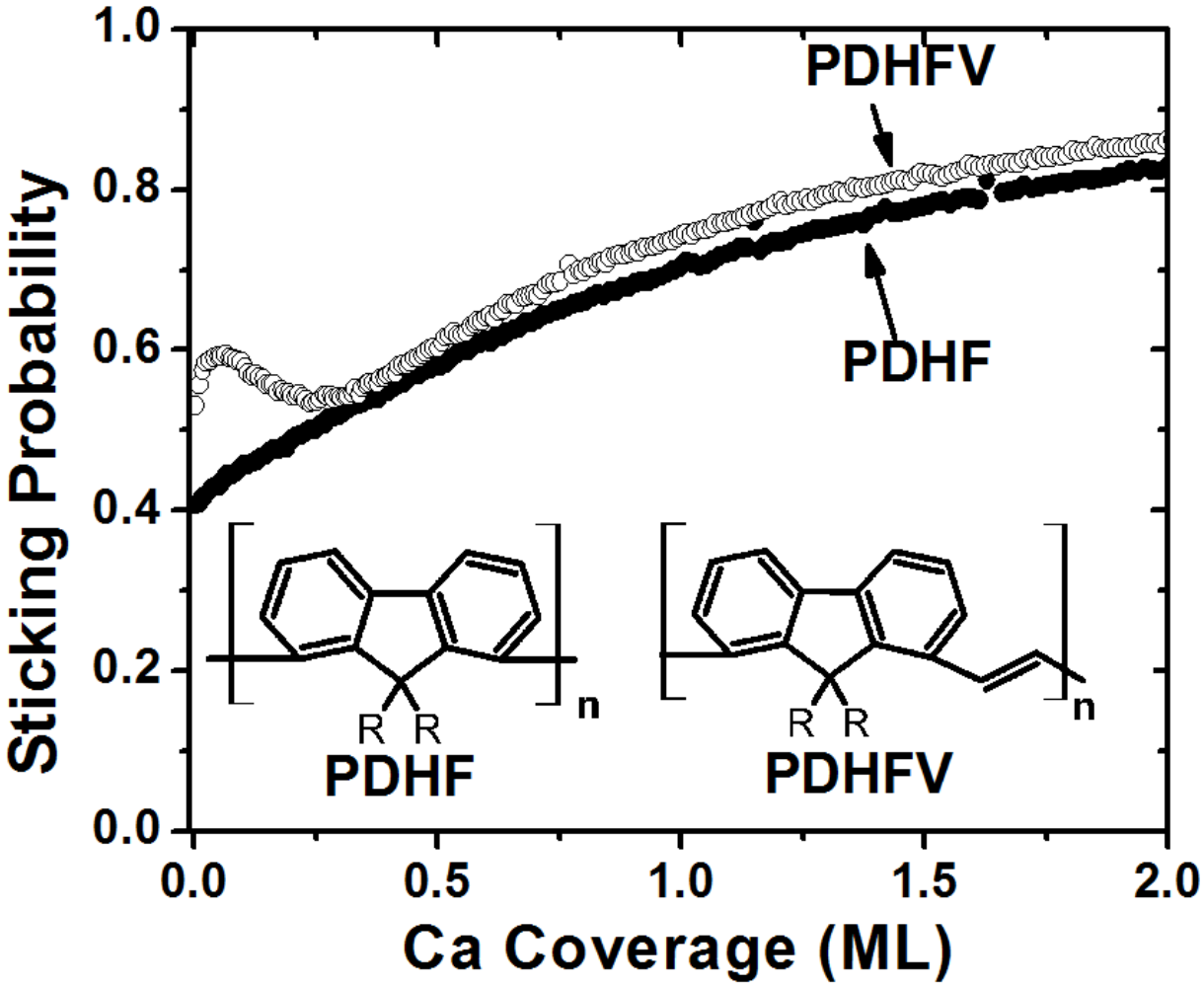

Figure 4.1 Sticking probability of Ca gas on PDHF and PDHFV at 300 K plotted as a function of Ca coverage. One monolayer is defined as 7.4×10^{14} Ca atoms per cm^2, the Ca(111) packing density. The inserts show the molecular structure of the polymers, where R is $-CH_2(CH_2)_4CH_3$.

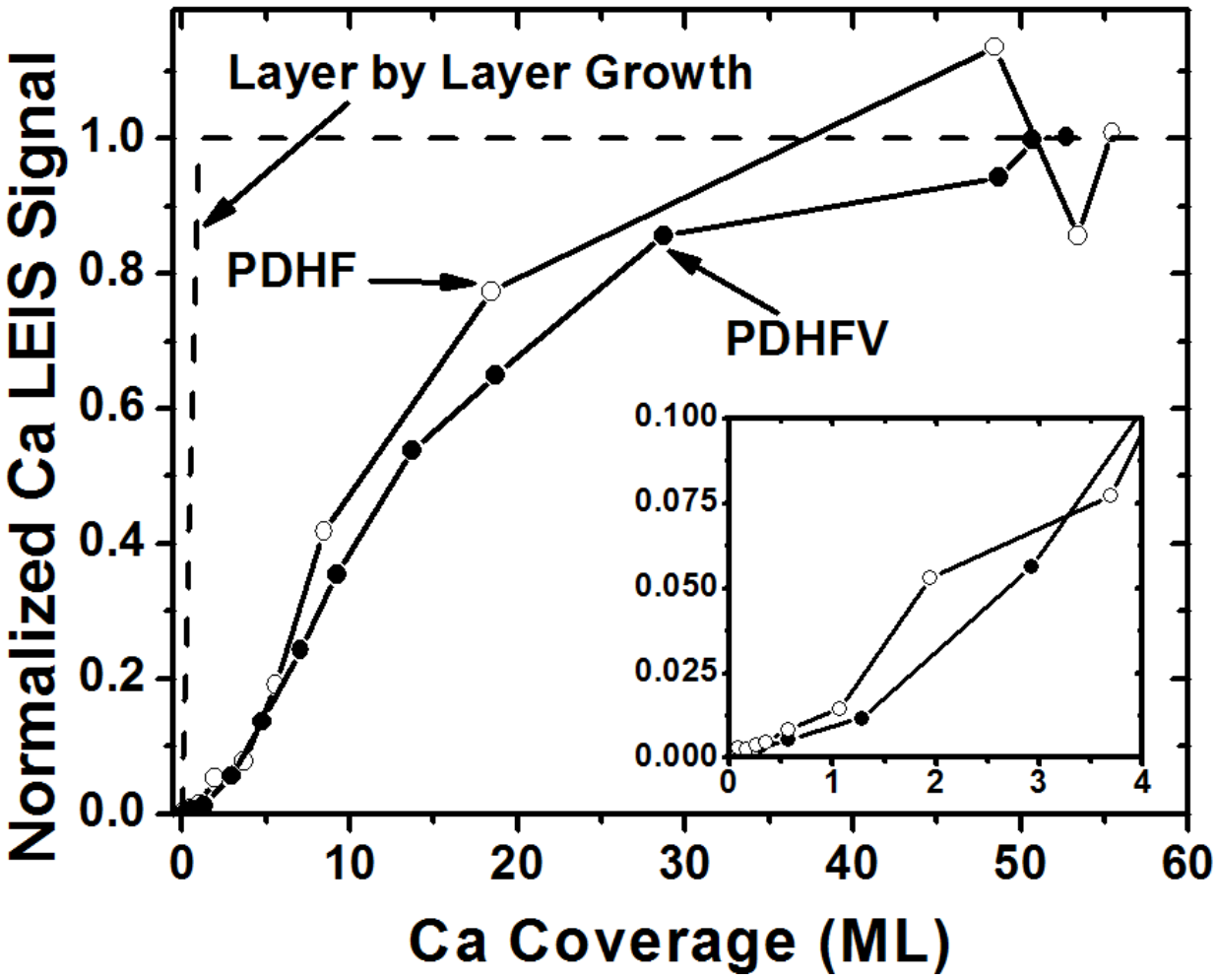

Figure 4.2 He^+ LEIS measurements of Ca signal versus Ca coverage on PDHF and PDHFV at 300 K. All intensities were normalized with respect to the saturation signal obtained for high Ca coverages. This normalized, integrated Ca LEIS peak intensity directly reflects the fraction of the polymer's surface area which is covered by Ca. The black dashed line indicates the expected trace for layer-by-layer growth. The inset shows an enlarged plot of the low-coverage region.

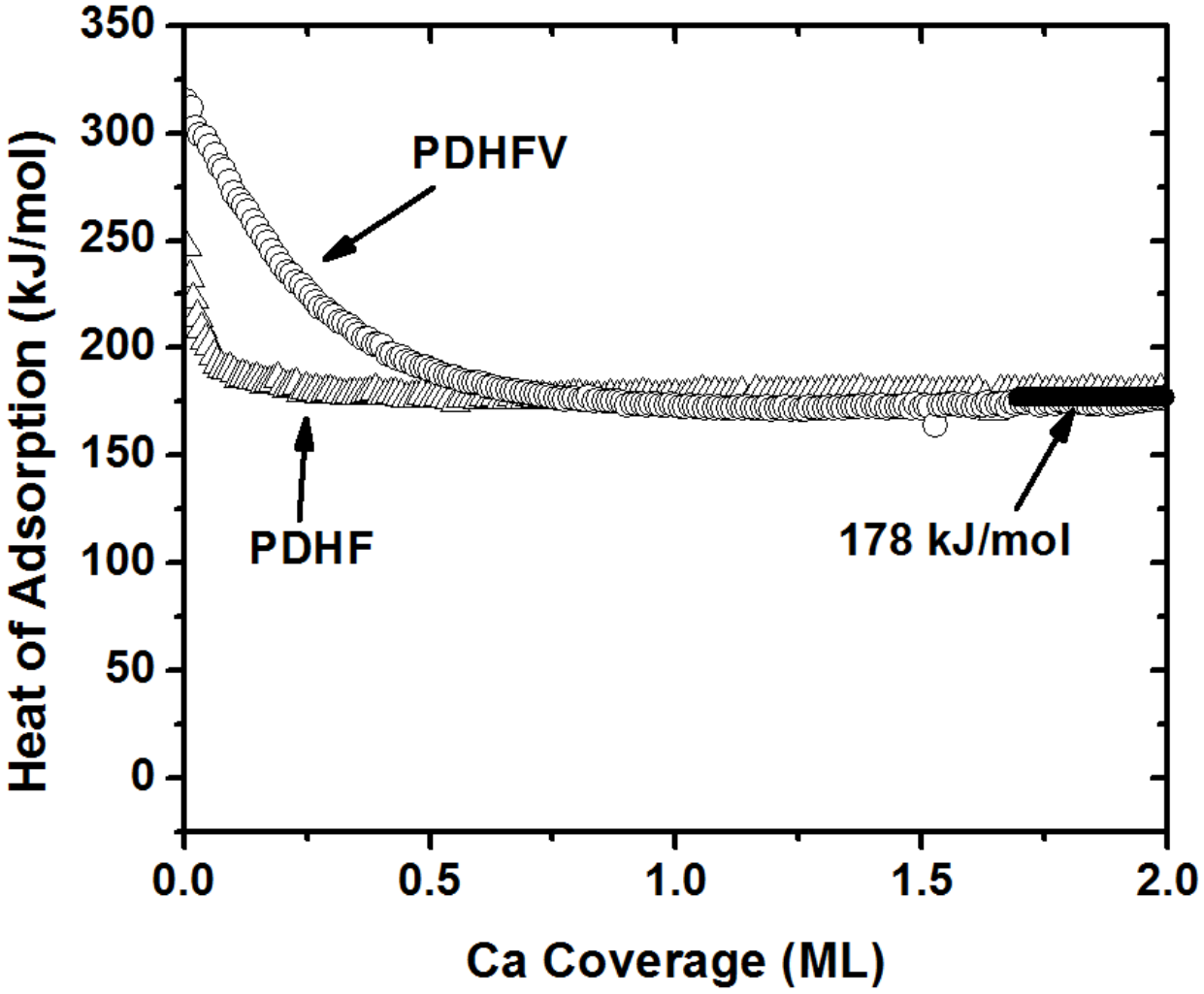

Figure 4.3 The differential heat of adsorption of Ca atoms on PDHF and PDHFV at 300 K as a function of Ca coverage. The sublimation enthalpy of Ca, $\Delta H_{sub}(Ca)$, is displayed as black solid horizontal line.

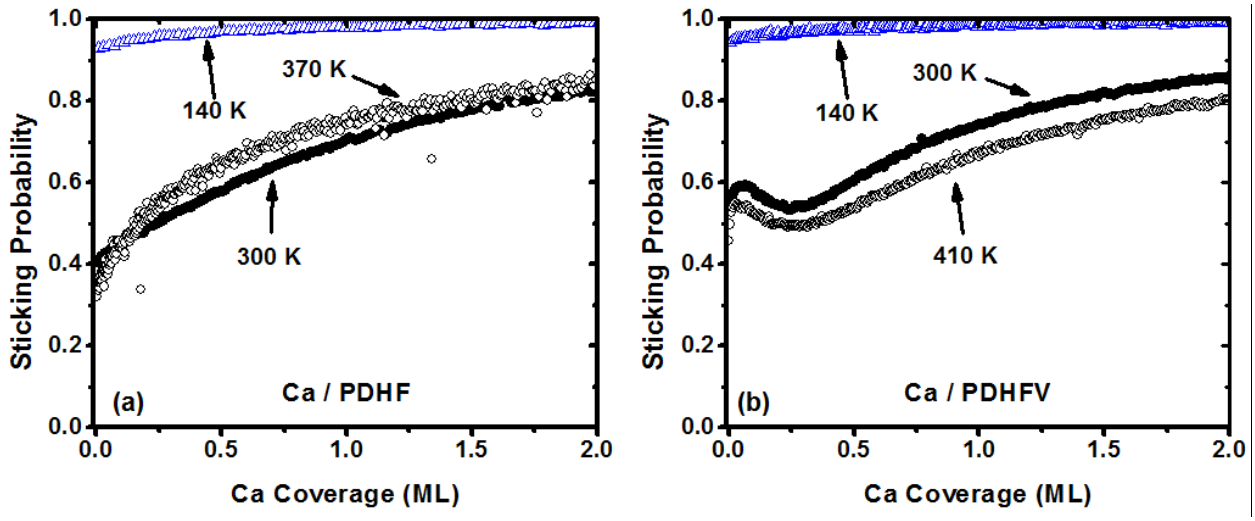

Figure 4.4 Sticking probability of Ca on (a) PDHF at 140, 300 and 370 K, and (b) PDHFV at 140, 300 and 410 K, plotted as a function of Ca coverage. One monolayer is defined as 7.4×10^{14} Ca atoms per cm^2, the Ca(111) packing density.

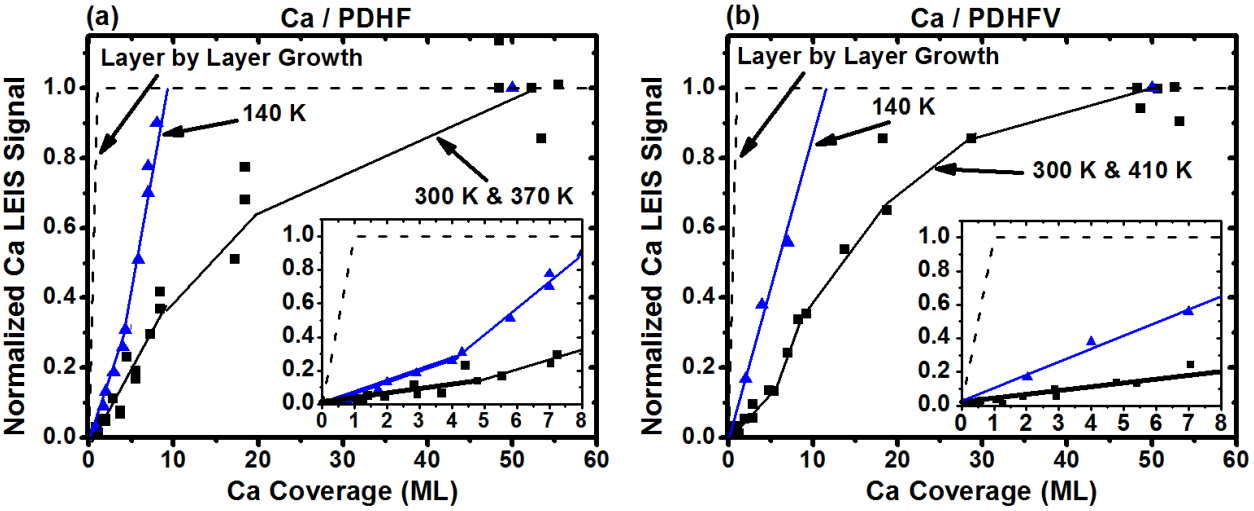

Figure 4.5 He^+ LEIS measurements of Ca signal versus Ca coverage on: (a) PDHF and (b) PDHFV, at 140, 300, and 370 or 410 K. The lines are drawn to aid the eye, not as a fit to the data. The dashed lines show the behavior that would be exhibited for a layer-by-layer growth model. The insets show enlarged plots of the low-coverage region.

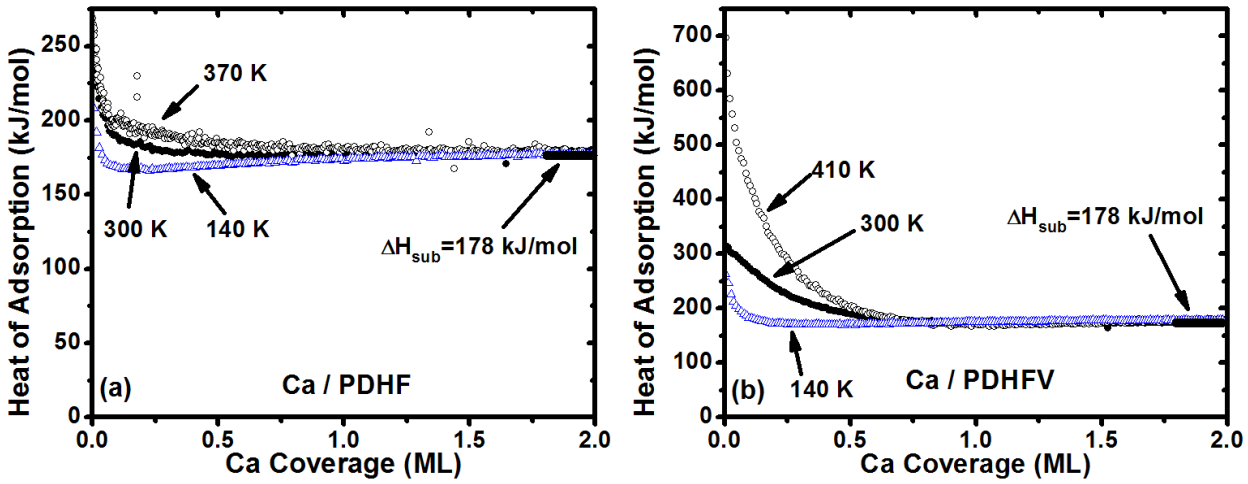

Figure 4.6 The differential heat of adsorption of Ca atoms on: (a) PDHF at 140, 300 and 370 K, and (b) PDHFV at 140, 300 and 410 K, as a function of Ca coverage. The sublimation enthalpy of bulk Ca(s), ΔH_{sub}, is marked with a short solid line.

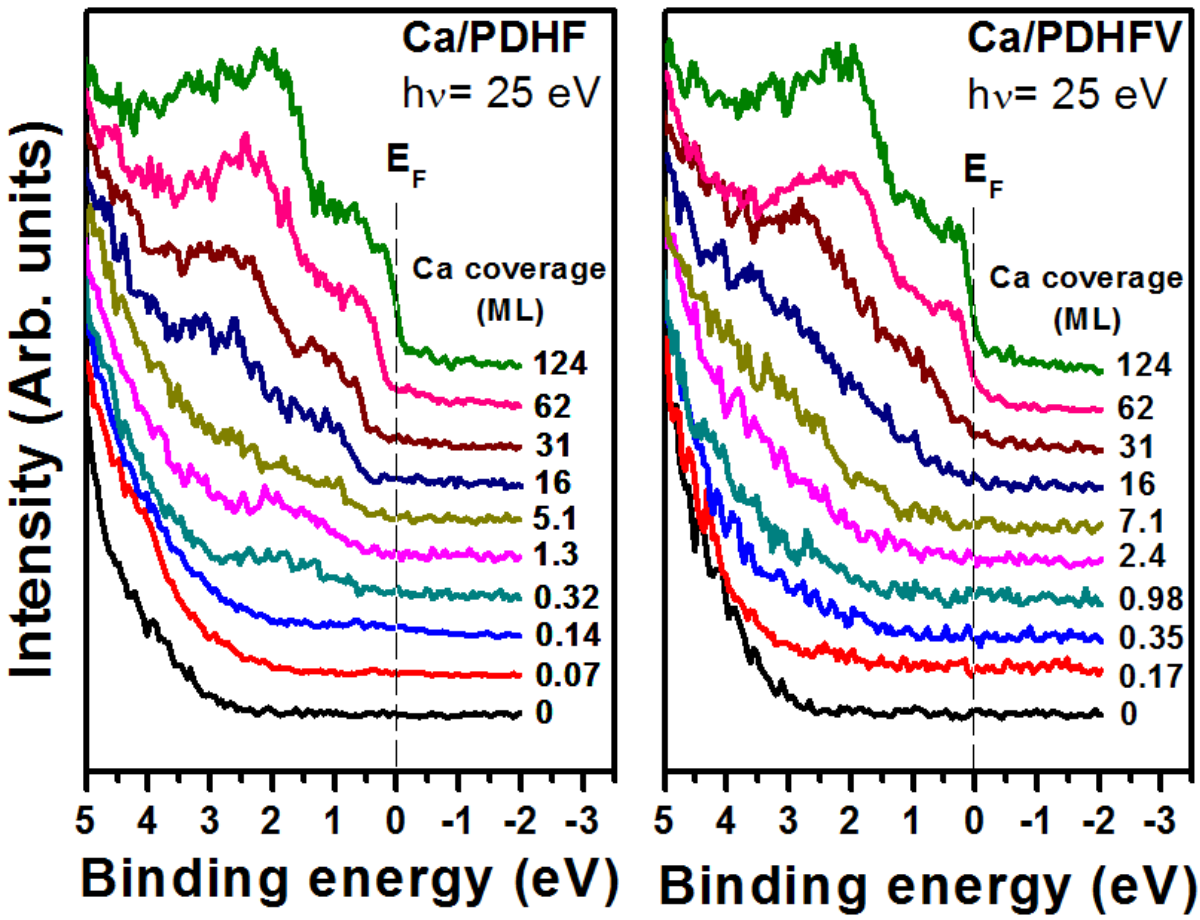

Figure 4.7 UPS spectra after Ca adsorption on PDHF and PDHFV at 300 K using 25 eV photon energy.

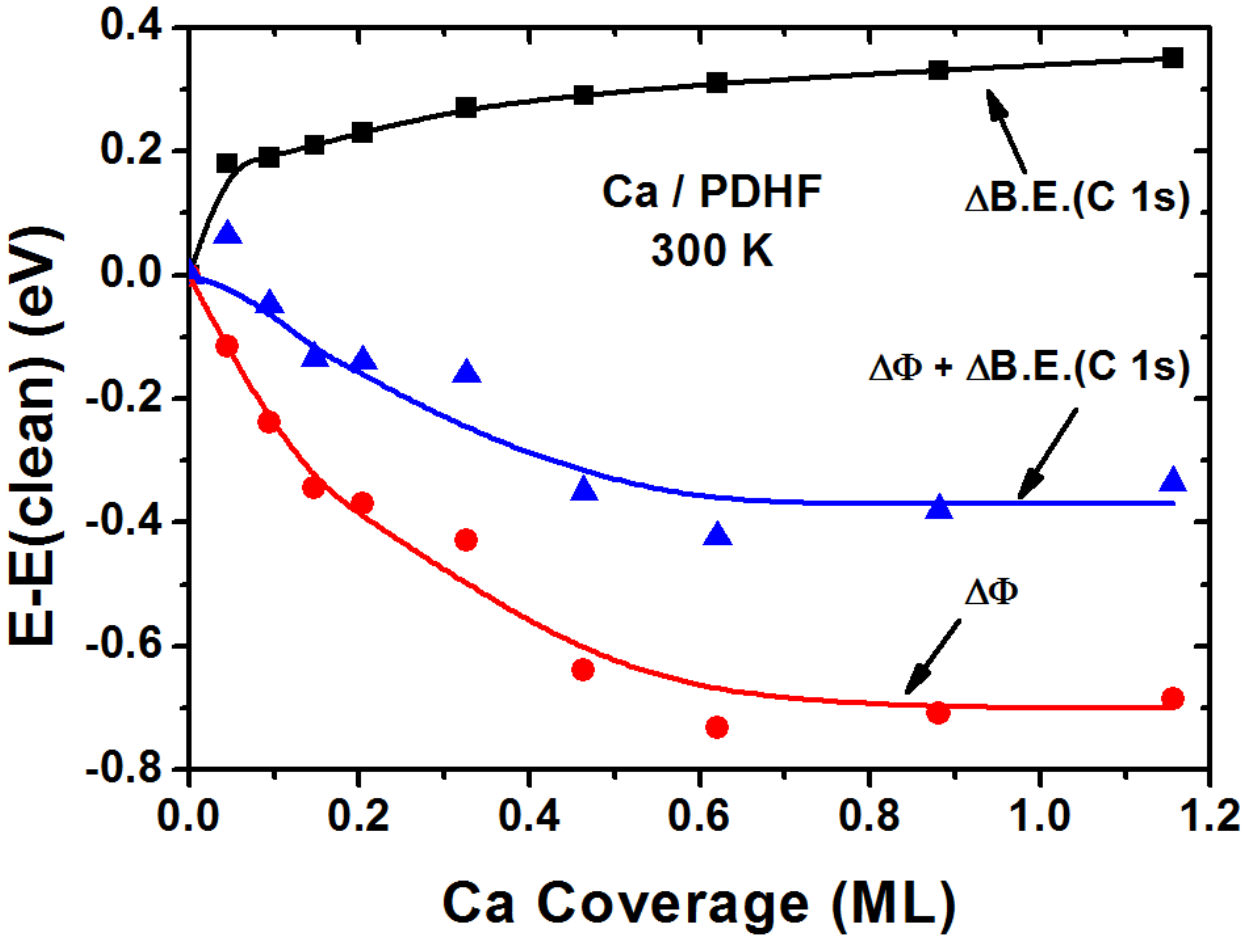

Figure 4.8 Changes with Ca coverage in the work function ($\Delta\phi$) and the binding energy of the C 1s XPS peak relative to the Fermi level (E_F) during deposition of Ca on PDHF at 300 K. The latter value reflects the long-range Ca-induced band bending (with the increase in B.E. reflecting downward band bending). Also shown is the sum of these two values, which gives the Ca-induced shift in the position of the valence band maximum (VBM) relative to the vacuum level.

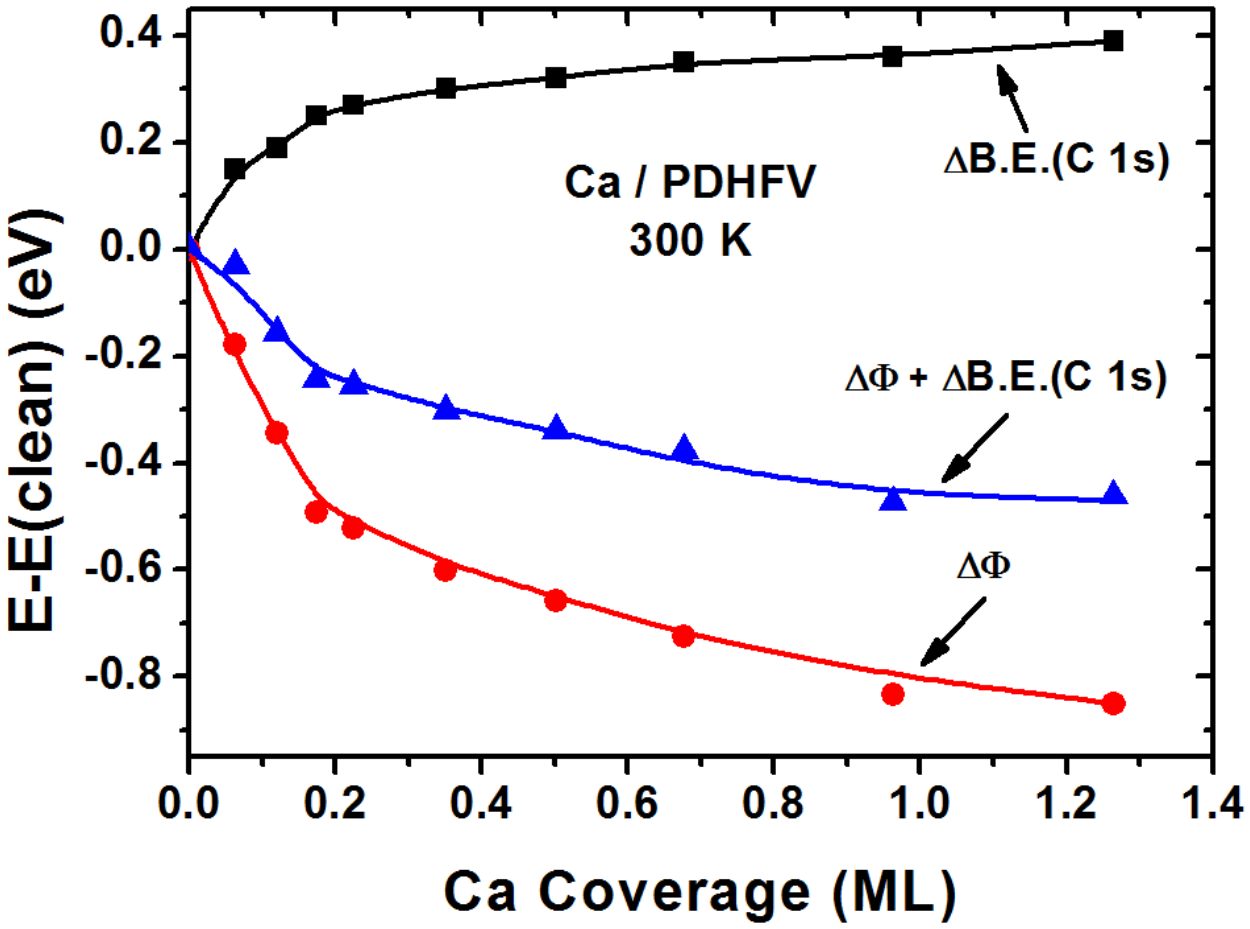

Figure 4.9 Changes with Ca coverage in the work function ($\Delta\phi$) and the binding energy of the C 1s XPS peak relative to the Fermi level (E_F) during deposition of Ca on PDHFV at 300 K. The latter value reflects the long-range Ca-induced band bending (downward for the increasing B.E. seen here). Also shown is the sum of these two values, which gives the Ca-induced shift in the position of the valence band maximum (VBM) relative to the vacuum level.

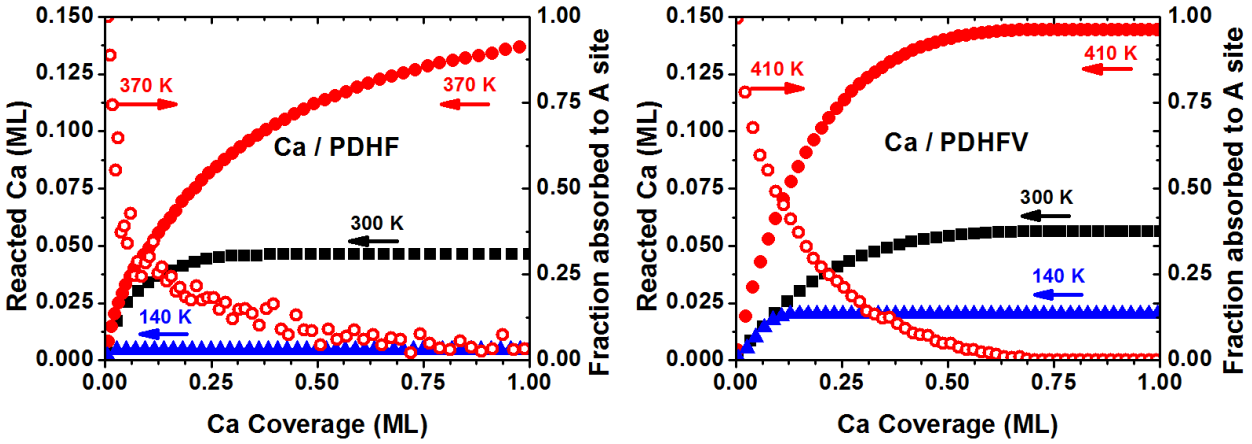

Figure 4.10 The integrated amount Ca which has reacted with A sites, estimated from the heats of Ca adsorption using the two-state model, plotted versus Ca coverage for different temperatures on PDHF (left) and PDHFV (right). The fraction of the adsorbed Ca in each pulse which reacted with A sites is also show for the highest-temperature curve in each case, as open circles.

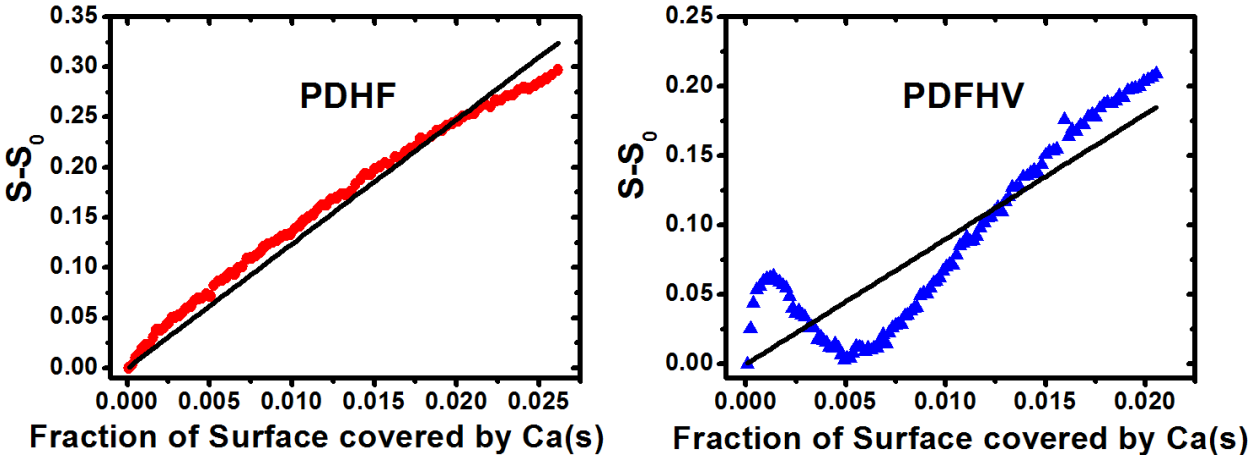

Figure 4.11 The difference between the sticking probability of Ca vapor at 300 K and its initial sticking probability, $S-S_0$, plotted versus the fraction of the surface covered by Ca(s), X_{Ca}, for Ca coverages below 1 ML. For PDHF, the slope of the best-fit proportional line shown is 12, and for PDHFV it is 9. The values for X_{Ca} used here were determined from the best-fit straight lines to the data in Fig. 2 below 1 ML Ca.

Chapter 5 Interface formation between Calcium and Electron-Irradiated Polyfluorenes

J.C Sharp, J.A. Farmer, J.H. Baricuatro, and C.T. Campbell*

Department of Chemistry, University of Washington, Seattle, Washington 98195-1700, USA

Abstract

The adsorption of Ca vapor on pristine and electron-damaged polyfluorenes, poly(9,9-di-*n*-hexyl-2,7-fluorene) (PDHF) and poly(9,9-di-*n*-hexyl-2,7-fluorene vinylene) (PDHFV), has been studied by adsorption microcalorimetry and low-energy He^+ ion scattering spectroscopy (LEIS) at 300 K. The Ca grows mainly as three-dimensional Ca(solid) particles that cover a small fraction of the surface below 10 monolayers (ML) of Ca, with a small amount of Ca diffusing subsurface to react with defects or impurities in the polymer at low coverages. The initial heat of adsorption of Ca is 250 kJ/mol onto pristine PDHF and 315 kJ/mol onto pristine PDHFV. These high initial heats are due to reactions with subsurface defects or impurities. The heats of adsorption for both polymers decreased nearly exponentially with Ca coverage to the sublimation enthalpy of bulk Ca(solid) (178 kJ/mol) by ~0.75 ML. Electron damage increases the sticking probability for Ca by ~0.1 to 0.2 and slightly increased the heat of adsorption of Ca at low coverages on both PDHF and PDHFV, with the largest increase in heat (by 65 kJ/mol) seen on PDHFV at the lowest Ca coverage, up from 380 kJ/mol. These increases are attributed to electron damage disrupting the polymer structure to enable faster Ca diffusion through the polymer. Electron damage does not significantly alter the morphology of the growing Ca(solid) particles on the surface of these polyfluorenes.

5.1 Introduction

Electron or ion beam damage has been shown to increase the reactivity of a polymer surface toward metals and improve the adhesion of metal films to their surfaces.[59,69,94-96] Ion beam damage has been shown to create additional metal atom adsorption sites on polymers.[69] Electron damage can cause mass loss of the polymer, chain scission, and cross-linking of polymer chains.[97-100] The effect of electron damage on Ca adsorption has been studied on poly(methyl methacrylate)[20] (PMMA) and poly(3-hexylthiophene)[13] (P3HT). For PMMA the electron damage increased the sticking probability at all coverages, decreased in the heat of adsorption, and increased the amount of Ca on the surface. For P3HT the electron damage increased the sticking probability at all coverages, the heat of adsorption was independent of electron damage except for below 0.1 ML of Ca coverage, and the growth of Ca on the surface was not significantly affected. The effect of electron damage on PDHF has been studied previously.[100,101] It was found that electron damage caused cross-linking of polymer chains or scission of the polymer backbone.

The interfaces formed between metals and semiconducting, π-conjugated polymers play an important role in organic electronic devices, such as organic light emitting diodes (OLEDs)[1], solar cells[2], and photodiodes.[3] One group of polymers that are of interest for these devices are polyfluorenes, which are relevant due to their blue electroluminescence and thermal stability.[29,31,85,86] Here, we study the effect of electron damage on the adsorption of Ca vapor on two polyfluorenes, poly(9,9-di-*n*-hexyl-2,7-fluorene) (PDHF) and poly(9,9-di-*n*-hexyl-2,7-fluorene vinylene) (PDHFV).

In our previous work[102], we studied the formation, structure and bonding energetics of the interface of calcium with these two polymers at temperatures from 140 to 400 K using Ca adsorption microcalorimetry, LEIS, and ultraviolet and X-ray photoelectron spectroscopies (UPS and XPS). . At 300 K, the initial heat of adsorption of Ca was found to be 250 kJ/mol on PDHF and 315 kJ/mol on PDHFV. This initial heat was assigned to Ca reacting with impurities or defects in these polymers. The heat of Ca adsorption on both polymers decreased nearly exponentially with coverage to the sublimation enthalpy of bulk Ca(solid) by 0.75 ML, which was attributed to the increasing probability of Ca finding and adding to solid three-dimensional (3D) Ca islands which nucleate and grow on the polymer surface. The temperature dependence showed that incoming Ca atoms are subject to a kinetic competition between diffusing into the polymer to react with subsurface defects or impurities versus adding to the three-dimensional Ca clusters on the surface, with slower diffusion of Ca adatoms to subsurface defects/impurities at lower temperatures.

In this present work, we employ LEIS and adsorption microcalorimetry to study the effect of electron damage on Ca adsorption onto these same polymer surfaces.

5.2 Experimental

The apparatus and procedures were identical to those used previously.[102] Briefly, the PDHF and PDHFV polymers were spin-coated directly onto the pyroelectric material used for heat detection. This process yielded a film thickness of ~100 nm, consistent with expectations based on prior work.[61] The samples were immediately transferred to the sample preparation chamber, pumped down to its base pressure of 8×10^{-9} Torr and outgassed while the polymer

was heated at 330 K for ~10 hours to remove trace amounts of solvent. The samples were then transferred into the ultrahigh vacuum (UHV) analysis chamber when needed. No remaining solvent was detected with Auger Electron Spectroscopy (AES). The Ca was dosed from an atomic beam that was chopped in to 100 ms long pulses which contained ~0.02 ML of Ca at a rate of 0.5 Hz. One monolayer (ML) of Ca is defined here as the Ca(111) packing density, 7.4 x 10^{14} Ca atoms per cm^2. LEIS was performed using $^4He^+$ ion with a primary energy of 1 KeV and an angle of 45° between the ion source and detector. Ion fluxes were typically 100 nA/cm^2 with a total ion dose of 6 mC/cm^2 per experiment.

The electron irradiation was performed by using the QMS filament as the electron source. The sample was biased with respect to the filament, such that the kinetic energy of the electrons to sample was 100 eV. The electron dose was determined by the measurement of the current to the sample.

5.3 Results and Discussion

Sticking Probability. The sticking probability of Ca on PDHF and PDHFV surface at 300 K with 10 ML electron damage (1 ML = 7.4 x 10^{14} electron per cm^2) and without electron damage as a function of Ca coverage is shown in Figure 1. The flux of the Ca atomic beam was measured by the calibrated QCM. The Ca coverage was determined by time-integrating the product of the Ca flux times the sticking probability, taking into consideration the chopped Ca beam's "on" time. Each curve in the figure is an average of three independent runs.

For PDHF, electron damage increased the initial sticking probability. The initial sticking probability on the pristine surface, 0.41, increased to 0.56 on the 10 ML electron damage film.

Similar results have been seen for Ca on PMMA[20] and Pb on PMMA.[59] The electron-irradiated curve showed a similar behavior to that of pristine PDHF, in that from its initial sticking it increases asymptotically to unity.

For Ca on PDHFV, electron irradiation also increased the initial sticking probability. The initial sticking probability on the pristine surface, 0.53, increased to 0.72 on the 10 ML electron damage film. Electron damage also eliminated the initial increase in the sticking probability seen in the pristine PDHFV. The electron-irradiated surface showed a slight decrease from the initial sticking probability with coverage below 0.2 ML, followed by an increase to asymptotically approach unity at high coverages.

Low Energy Ion Scattering. When metal is vapor deposited onto a polymer film, the metal atoms can form 3D islands or a continuous film on the surface, or diffuse below the surface and react with functional groups of the polymer.[12,13,20,65-69,90] Figure 2 shows the normalized Ca LEIS signal as a function of Ca coverage for both pristine and 10 ML of electron damage films of PDHF and PDHFV at 300 K. As observed for the pristine polymers, the growth of Ca LEIS signal on the electron-damaged polymers was much slower than expected for layer-by-layer growth (for which model the expected growth curve is shown), which was attributed to the growth of 3-D Ca(solid) particles that cover only a small fraction of the surface below 5 ML Ca.[102] For Ca on PDHF, electron irradiation did not significantly affect the growth mode in the low coverage range (<3 ML). For Ca on PDFHV, at low coverage the coverage of the surface are by 3-D Ca(s) islands is slightly faster on the damaged surface.

Heat of Adsorption. Figure 3 shows the differential heat of adsorption of Ca on PDHF at and PDHFV at 300K for pristine and electron-irradiated films (10 ML electron) as a function of Ca coverage. Each curve in the figure is an average of 3 independent runs. As noted above,

the high initial heat of Ca adsorption on these surfaces without electron damage was assigned previously to Ca reacting with subsurface impurities or defects in both these polymers, with the incoming Ca atoms experiencing a kinetic competition between diffusing into the polymer to react with these defects / impurities versus nucleating or adding to 3D Ca clusters on the surface..[102] The latter process gets more and more probable as coverage increases, so that the heat decreases exponentially to eventually reach the bulk heat of Ca sublimation.

For Ca on PDHF at 300 K, electron damage does not change the initial heat of adsorption of 247 kJ/mol, but increases the amount of Ca needed to reach the heat of sublimation of Ca. For the pristine film, the heat of sublimation of Ca is reached by about 0.75 ML Ca coverage and for the 10 ML electron-irradiated film, it is reached by about 1 ML Ca. For Ca on PDHFV at 300 K, electron damage increased the initial heat of adsorption slightly, from 315 kJ/mol to 380 kJ/mol on electron damaged surfaces. The effect of electron damage is much smaller than the effect of increasing temperature on the pristine PDHFV to 410 K, which increased the initial heat to 700 kJ/mol.[102] This suggests that at least part of the apparent 65 kJ/mol increase in the initial heat with electron damage instead may be due to slight temperature differences between "room temperature" (300 K) in these studies.

For both polymers, electron damage has an effect that is similar to that of a small increase in temperature: it increases the probability for Ca diffusion to react with subsurface defects/impurities in its kinetic competition with Ca nucleating or adding to 3D Ca(solid) clusters on the surface. This suggests that electron damage disrupts the polymer structure to enable faster Ca diffusion through the polymer. This would also explain its increase in the sticking probability of Ca (Fig. 1), since this would also increase the probability that Ca react in

its kinetic competition with simple Ca desorption. The electron-induced disruption of the polymer may result from localized bond breaking or charging by the incident electrons.

5.4 Conclusions

Electron damage increases both the sticking probability for Ca gas atoms and their heat of adsorption at low Ca coverages on both PDHF and PDHFV. This is attributed to electron-induced disruption of the polymer structure so that Ca diffuses faster through the polymer. LEIS shows that electron damage does not significantly alter the growth morphology of Ca(s) on the surface of these polyfluorenes.

Acknowledgments

C.T.C. and J.C.S. thank the US National Science Foundation for financial support under CHE-1010287

5.5 Figures

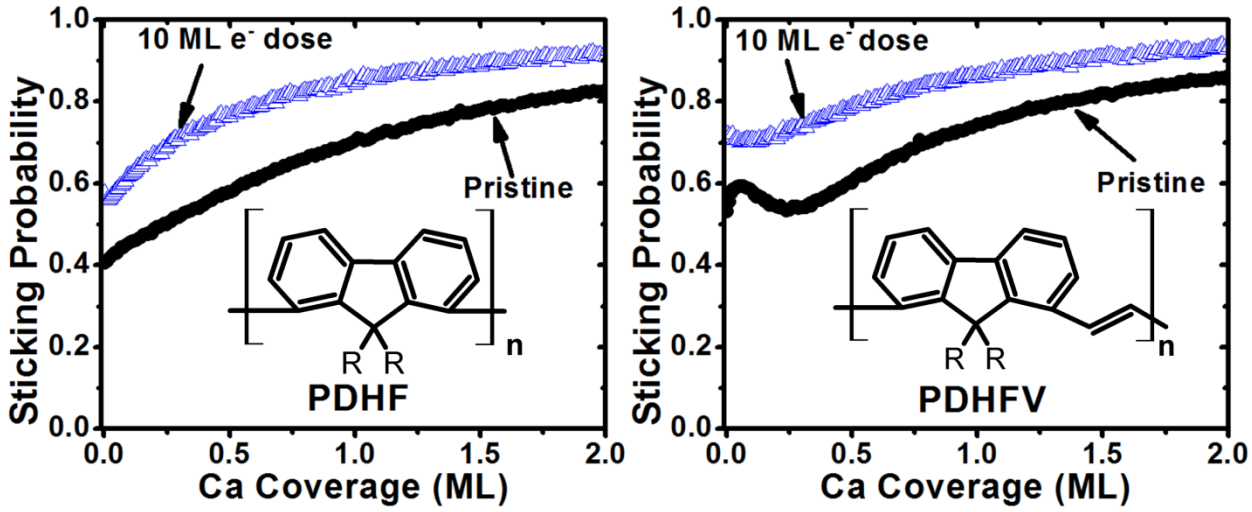

Figure 5.1 Sticking probability of Ca vapor on PDHF and PDHFV films at 300 K plotted as a function of Ca coverage for the pristine and electron-irradiated surfaces. One monolayer is defined as 7.4×10^{14} Ca atoms per cm^2, the Ca(111) packing density, for Ca coverage and electron dose. The inserts show the molecular structure of the polymers, where R is $-CH_2(CH_2)_4CH_3$.

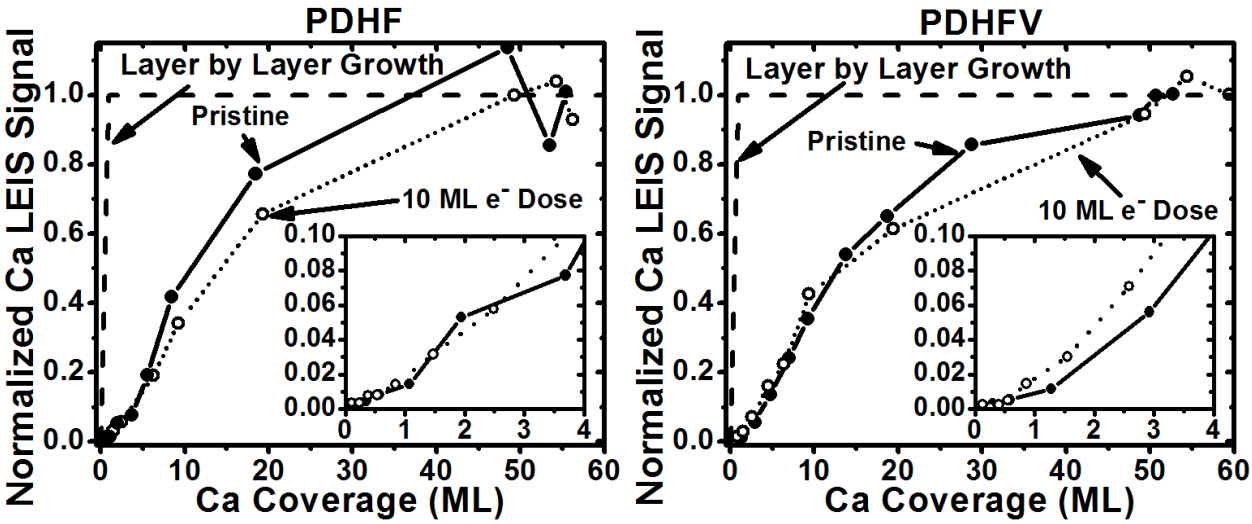

Figure 5.2 He^+ LEIS measurements of Ca on PDHF and PDHFV on pristine and electron-irradiated surfaces. The normalized integrated Ca ISS peak intensity is displayed as a function of Ca coverage. All intensities were normalized with respect to the saturation signal obtained for high Ca coverages. The lines are drawn to aid the reader in visualization, not as fit to the data. The black dashed lines show the behavior that would be exhibited for a layer-by-layer growth model. The insets show enlarged plots of the low Ca coverage region.

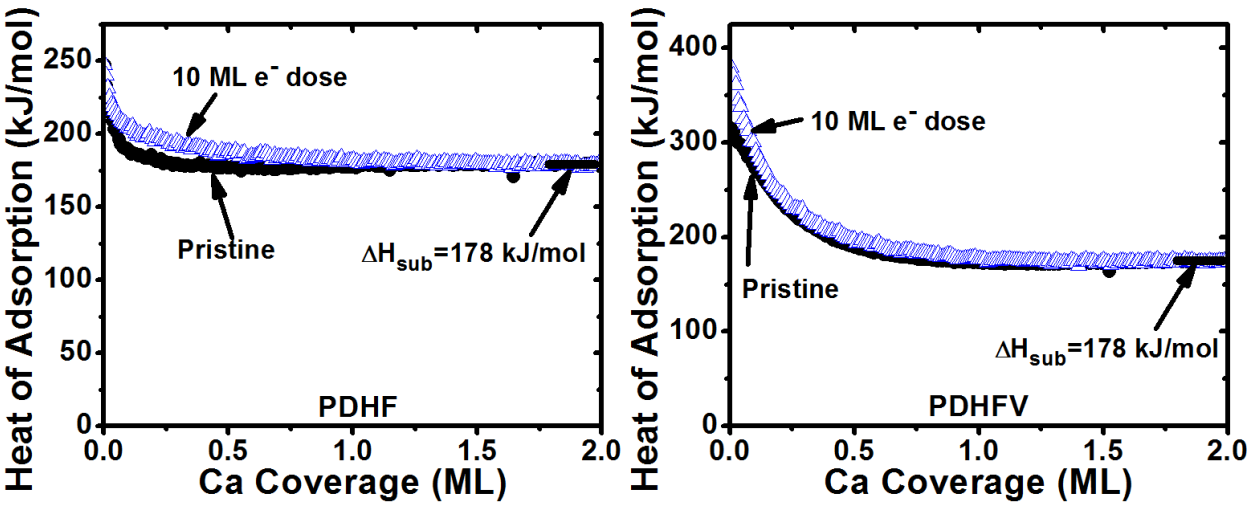

Figure 5.3 Differential heat of adsorption of Ca gas atoms on PDHF and PDHFV, for both pristine and electron-irradiated surfaces, as a function of Ca coverage at 300 K. The sublimation enthalpy of Ca, ΔH_{sub}=178 kJ/mol, is displayed as black solid horizontal line.

Chapter 6 Silver Nanoparticles on Fe3O4(111): Energetics by Ag Adsorption Calorimetry and Structure by Surface Spectroscopies

James C. Sharp Y. X. Yao and Charles T. Campbell*

Departments of Chemistry

University of Washington

Seattle, WA 98195-1700 USA

Abstract

The heat of adsorption of Ag atoms and the growth morphology of the resulting silver particles on the $Fe_3O_4(111)$ surface at 300 K were studied by adsorption microcalorimetry, Auger electron spectroscopy (AES) and low energy ion scattering spectroscopy (LEIS). Thin films (~6 nm thick) of $Fe_3O_4(111)$ were grown on a Pt(111) single crystal. The changes in AES and LEIS signals versus Ag coverage during Ag vapor deposition onto $Fe_3O_4(111)$ were indicative of Ag growing as 3D particles with a fixed density of ~4 x 10^{12} particles/cm^2. The heat of Ag adsorption increased with Ag coverage from ~230 kJ/mol initially up to within a few percent of the heat of sublimation of bulk Ag (285 kJ/mol) by ~2 ML Ag. This corresponds to an increase in Ag atom stability (decrease in chemical potential) by ~55 kJ/mol as the Ag particle size grows from <1 to ~4 nm effective diameter on $Fe_3O_4(111)$. The Ag(solid) / $Fe_3O_4(111)$ adhesion energy for the 4 nm particles was estimated from the integral heat of adsorption to be 2.5±0.3 J/m^2. The sticking probability of Ag atoms was ~0.96 initially and increased to ~0.99 by ~1.0 ML and above.

6.1 Introduction

Nanoparticles of late transition metals dispersed across the surface of oxide support materials are the key ingredients in many heterogeneous catalysts, fuel cells, other electrocatalysts and photocatalysts, which are crucial for energy, fuel and environmental technologies and chemical processing. In such materials, the nature and strength of the chemical bonding interactions at the interface between the metal nanoparticle and the oxide surface are very important to the material's performance, such as its catalytic activity, selectivity and long-term stability against deactivation by sintering.[4-6] The strength of the interaction for metal adsorption and adhesion onto oxide surfaces is not known for many systems, yet this determines the chemical potential of the metal atoms in the supported nanoparticles, which we showed directly correlates with their resistance to sintering and their chemical and catalytic reactivity.[6]

Iron oxides are promising materials for many of these applications. In particular, late transition metal nanoparticles supported on iron oxides form the basis for new materials that are being intensively investigated for use in catalysts, fuel cells, other electrocatalysts and photocatalysts. To understand these systems, many have used a model catalyst approach, whereby nanoparticles of the late transition metal are vapor deposited onto the surface of a clean single-crystalline surface of the oxide support[4-6]. This allows better control of the structure of the nanoparticles and their interface to the oxide support. Thus, to understand catalysts that use iron oxide supports, many researchers have studied metal nanoparticles supported on the magnetite $Fe_3O_4(111)$ surface.[42-49] For example, gold supported on $Fe_3O_4(111)$ has been studied for carbon monoxide oxidation and water gas shift.[49] Water gas shift has also been studied over copper on $Fe_3O_4(111)$.[48] Palladium on $Fe_3O_4(111)$ has been studied for CO oxidation.[42-44]

Silver, usually supported on other oxides, is known to be a catalyst for epoxidation of olefins[51,103], partial oxidation of methanol,[104] and oxidation of carbon monoxide at low temperatures.[50]

In this work, we report calorimetric measurements of the heat of adsorption of Ag vapor onto a clean and well-ordered Fe_3O_4(111) surface, wherein the Ag particle morphology is characterized by Auger electron spectroscopy (AES), and low energy ion scattering spectroscopy (LEIS). The results are analyzed to provide the relative enthalpy and chemical potential of the Ag atoms versus Ag nanoparticle size on Fe_3O_4(111), and the Ag / Fe_3O_4(111) adhesion energy. The results are compared to similar measurements of Ag particles on MgO(100) and CeO_2(111).[105,106] To our knowledge, no other report exists of the heat of adsorption of any metal on any iron oxide surface. A preliminary report of some of these results has appeared.[107] The morphology of Ag growth on Fe_3O_4(001) at 200 °C, 400 °C, and 750 °C has been study by Reflection High Energy Electron Diffraction, X-ray reflectivity and diffraction, High Resolution Transmission Electron Microscopy, and Atomic Force Microscopy.[50]

6.2 Experimental

The details of the calorimetric measurement of Ag gas atom adsorption energies onto oxide supports has been presented in detail elsewhere.[106] The calorimeter was housed in an ultrahigh vacuum chamber, with a base pressure of ~2 $\times 10^{-10}$ Torr (rising to ~1 $\times 10^{-9}$ Torr, which was mainly H_2, during Ag deposition). It was equipped with low energy electron diffraction (LEED), Auger electron spectroscopy (AES), low-energy ion scattering spectroscopy (LEIS), a quadrupole mass spectrometer (QMS), and a quartz crystal microbalance (QCM). AES was

carried out using 1.6 keV electrons from a PHI LEED system (15-120), and a Leybold-Heraeus EA11 hemispherical energy analyzer. ISS was carried out using He^+ ions with 1 keV primary energy from a de-focused ion gun (Leybold-Heraeus IQE 12/38). The calorimeter consists of a pulsed metal atom beam and a pyroelectric polymer (polyvinylidenefluoride, PVDF) ribbon pressed against the back of the single crystal for heat detection. The 4-mm diameter, chopped Ag atom beam is produced from a high-temperature effusion cell. The Ag was purchased from Alfa Aesar with 99.999 % purity. The metal atom beam is chopped to provide 100 ms pulses containing ~0.02 ML of Ag atoms every two seconds. One monolayer (ML) is defined throughout as 1.42×10^{15} atoms/cm^2, which is the number of oxygen atoms exposed to the vacuum per unit area for Fe_3O_4(111). The absolute beam flux is measured by using a calibrated QCM. The sticking probability is measured by a modified King–Wells method, using a line-of-sight quadrupole mass spectrometer (QMS) to measure the fraction of metal atoms which strike the surface but do not adsorb. The mass spectrometer signal was calibrated by measuring the integrated desorption signal from a known amount of Ag reflected from a hot Ta foil (1100 K to 1200 K), located at the same position as the sample and corrected for average velocity.

The typical operating temperature of the effusion cell was ~1380 K, which generated some thermal radiation that impinged on the sample and also was detected by the calorimeter. This thermal radiation was measured by inserting a BaF_2 flag between this cell and the sample. The flag blocks the Ag atoms but allows almost all the thermal radiation to pass. The measured thermal radiation was then corrected for the transmittance of the BaF_2 flag (~92%). The heat signal for Ag adsorption was corrected for this thermal radiation by subtraction, and the heat detector was calibrated using light pulses from a He-Ne laser, as described elsewhere [58,106]. The amount of light adsorbed per pulse from this He-Ne laser for pulses of fixed energy was

measured and found to decrease nearly linearly with Ag coverage, from its starting value on the Ag-free Fe_3O_4(111) to 69±3% of its starting value by 3 ML Ag, and remain constant afterwards. By setting the final reflectivity of thick multilayer Ag to the literature value for bulk Ag of 94%[106], we estimate that the initial reflectivity for the starting Fe_3O_4(111) thin film was 91±1% using this 31% decrease in absorbed light.

To convert the calorimetrically measured internal energy changes into standard enthalpy changes at the sample temperature (300 K), the excess translational energy of the metal gas atoms at the oven temperature, above that for a 300 K Maxwell–Boltzmann distribution (~0.3 μJ/pulse), is subtracted, and a small pressure–volume work term (RT per mole) is added, as described elsewhere.[58] The corrected enthalpy of adsorption is thus the standard molar enthalpy of adsorption at 300 K, which at high coverage, where the atoms are adding to bulk-like sites, can be compared directly to the standard heat of sublimation of the metal. The measured heats are expressed as the enthalpy of adsorption on a "per mole of adsorbed Ag" basis by correcting for the sticking probability.

The preparation of the 1 μm-thick Pt(111) single-crystal was described previously [106,108]. The preparation of Fe_3O_4(111) thin films on Pt(111) was based on the recipe of Zscherpel et al. [109]. In brief, ~1 monolayer of FeO is first grown by depositing ~1 ML of Fe on Pt(111) at 300 K and annealing for 5 minutes at 900 K in 5 x 10^{-7} Torr O_2. Then ~20 ML of Fe is deposited in 2 x 10^{-7} Torr O_2 at 300 K, and subsequently annealed at 800 K in 5 x 10^{-7} Torr O_2 for 5 minutes. This led to a Fe_3O_4(111) film of ~6 nm thickness, whose composition, cleanliness and order were verified by AES and LEED.

6.3 Results and Discussion

Characterization of the Fe_3O_4(111) Thin Films. The Fe_3O_4(111) thin films were characterized by AES and LEED. The AES spectra matched spectra previously reported for Fe_3O_4(111).[110] Figure 6.1 shows a typical LEED pattern for the grown Fe_3O_4(111) thin film. The p(2x2) LEED image is comparable to previous reports.[111]

Sticking Probability of Ag on Fe_3O_4(111). Figure 6.2 shows the sticking probability as a function of Ag coverage at 300 K. The initial sticking starts at 96% and increases to ~99% by 1.0 ML Ag coverage. The flux of the Ag atomic beam was measured by the calibrated QCM. The Ag coverage was determined by time-integrating the product of the Ag flux times the sticking probability, taking into consideration the chopped Ag beam's "on" time. This figure is the average of three independent runs

Morphology of Ag Islands on Fe_3O_4(111). The morphology of the growing Ag film on Fe_3O_4(111) was studied by AES and LEIS. Figure 6.3 shows the AES measurements for Ag on Fe_3O_4(111). The circles represent the integrated intensity of the Ag(MNN) Auger peak at 351 eV normalized to the signal from a thick, bulk-like Ag film (>30 ML). The triangles represent the integrated intensity of the oxide's O(KVV) peak at 515 eV normalized to the signal from O(KVV) AES signal from Fe_3O_4(111) with no Ag deposited.

The dashed lines in Fig. 6.3 also show the theoretical intensities expected for O(KVV) and Ag(MNN) if Ag grew in a layer-by-layer fashion[112] on Fe_3O_4(111). The measured AES signals change much more slowly than in layer-by-layer growth, indicating 3D island growth. The solid lines show a fit of the data to a hemispherical cap model.[52,83] As shown in Figure 6.3 the hemispherical cap model fits the data well. The hemispherical cap model assumes Ag

growth as 3D particles on the surface in the shape of hemispheres of fixed diameter at any given coverage, and a number density that is constant, independent of Ag coverage.[52] The model represented by solid lines uses a density of 4 x 10^{12} particles /cm^2. The model was only fit up to the Ag coverage of 2.1 ML, because after approximately 35% of the surface area is covered by Ag islands, they can begin to overlap and the assumption that the hemispheres are isolated is no longer valid.

Figure 6.4 shows the growth morphology of Ag on Fe_3O_4(111) as probed using He^+ LEIS. The integrated intensity of the Ag peak (circles) versus Ag coverage is shown. The normalized Ag LEIS signal provides a direct measure of the fraction of the surface that is covered by Ag, since it is sensitive to only the topmost atomic layer. Thus, at any Ag coverage, the Ag coverage divided by this fractional signal is equal to the average thickness on the Ag islands, in ML. Beam damage from the ion beam was minimized by measuring only a small kinetic energy range corresponding to the Ag peak and using a small ion beam exposure for each data point. The lack of ion beam effects was proven in control experiments performed with large coverage increments, which were indistinguishable from the experiments in Figure 6.4. This indicates that beam damage did not impact the growth measurement within the accuracy of the LEIS experiment. Also shown is the expected curve for layer-by-layer growth (dashed line) and hemispherical cap (solid line) growth with a density of 4 x 10^{12} particles per cm^2. As with the AES data, the growth of Ag on Fe_3O_4(111) fits the hemispherical cap model well. Previously, 3D island growth was reported for Ag growth on Fe_3O_4(001) at 200 °C.[50]

Heat of Adsorption of Ag on Fe_3O_4(111). Figure 6.5 shows the differential heat of adsorption of Ag on Fe_3O_4(111) as a function of coverage. The curve is the average of three experimental runs. The insert shows the low coverage region (0-0.8 ML) in more detail. The

pulse-to-pulse standard deviation at high Ag coverages (where the heat of adsorption was constant) was 6 kJ/mol and the experiment-to-experiment standard deviation was 16 kJ/mol (6%). To rule out possible effects on the heat of adsorption due to surface damage by electrons (from doing AES and LEED after Fe_3O_4(111) film growth), a control experiment of Ag adsorption on Fe_3O_4(111) was done without doing AES or LEED before the calorimetry experiment, and no difference was observed compared to experiments where LEED and/or AES were done after film growth.

The heat of adsorption starts at ~230 kJ/mol and rises to ~277 kJ/mol by 0.5 ML, then slowly increases to the heat of sublimation of Ag (285 k/mol[77]) by ~2 ML. The low initial heat of adsorption shows that Ag binds more weakly (~55 kJ/mol) to the Fe_3O_4(111) surface than the surface of Ag(solid) bulk. The near unity sticking probability and the fact that Ag grows as 3D particles indicate that Ag adatoms are adsorbed in very mobile precursor state and diffuse to nucleate a new Ag cluster or find and attach to an existing Ag cluster, and only a very few desorb back into the gas. The rise in the measured heat up to the heat of sublimation by 2 ML can be attributed to the effect of particle size on the binding energy of Ag to Ag nanoparticles, similar to what we have reported for Pb, Ag, and Cu on Mg(100)[113,114] and Ag on CeO_{2-x} (111).[106]

Heat of Ag Atom Adsorption versus Ag Particle Size. Based on the heat of adsorption data and the Ag hemispherical particle density measured using AES and LEIS, the heat of adsorption versus particle size can be determined. To do this, we divided the best-fit Ag particle density (4 x 10^{12} particles /cm^2) by the Ag coverage (in atoms /cm^2) to get the average Ag particle size (in atoms), which is easily converted to an average volume and effective diameter using the bulk Ag density and the relationship between diameter and hemisphere volume, as described previously.[78] Figure 6.6 shows the heat of adsorption versus average Ag particle size

and number of Ag atoms already in the particle. As shown in Fig. 6.6, the heat of adsorption grows rapidly with particle size below 2.5 nm but, after reaching a particle diameter of ~4 nm, the heat of adsorption approaches within the noise of the data to the heat of sublimation of bulk silver solid (285 kJ/mol). This ~55 kJ/mol increase in heat of adsorption corresponds to a ~55 kJ/mol decrease in the chemical potential of Ag atoms in Ag nanoparticles supported on Fe_3O_4(111) as their particle size increases from ~0.6 nm to 4 nm. (This assumes that entropic differences with particle size are small compared to these large enthalpic effects.) Much more dramatic changes in chemical potential with particle size were seen for Ag on MgO(100), but Ag on slightly reduced CeO_2(111) surfaces behaved quite similar to these present results on Fe_3O_4(111).[39]

The implications of these results with respect to the effect of Ag particle size on the catalytic properties for Au in relation to Ag on Fe_3O_4(111), ceria, reduced ceria and MgO(100) has been discussed elsewhere, when we gave a preliminary report of these results.[107]

Adhesion Energy of Ag Solid onto Fe_3O_4(111). Using the data in Figs. 6.5 and 6.6, the adhesion energy of 3.6 nm diameter Ag particles to Fe_3O_4(111) can be calculated to be 2.5±0.3 J/m^2 using the simple thermodynamic cycle previously derived.[35,115] This result is much larger than the adhesion energy for Ag nanoparticles to MgO(100) surfaces (0.3±0.3 J/m^2) and similar to that for Ag nanoparticles on CeO_{2-x}(111) surfaces (2.3 to 2.6 J/m^2).[78] The value of 2.5±0.3 J/m^2 is statistically indistinguishable from the value for Ag to itself (i.e., twice the surface energy of pure Ag solid, 2.44 J/m^2 [105]). This indicates very strong bonding at the Ag/ Fe_3O_4(111) interface. The same effects of lattice mismatch discussed regarding Ag nanoparticle binding to CeO_{2-x}(111) surfaces[78], and the resulting change in adhesion energy as Ag particle size grows, are also likely to occur for Ag on Fe_3O_4(111).

6.4 Conclusions

Silver atoms adsorb onto $Fe_3O_4(111)$ with an initial heat of adsorption of ~230 kJ/mol, increasing with coverage to the heat of sublimation of bulk Ag (285 kJ/mol) by ~2 ML. This initial heat of adsorption is ~55 kJ/mol weaker than Ag bonding to bulk Ag. The sticking probability was found to be ~0.96 initially and increase to ~0.99 by ~1.0 ML. Based on AES and LEIS data, Ag grows as 3D islands on $Fe_3O_4(111)$ with a fixed particle density of 4×10^{12} particles/cm^2. Using this particle density, the average size of Ag particles was calculated at each Ag coverage, and the heat of adsorption versus Ag particle size was determined. From this, it was found that the Ag atoms in Ag nanoparticles supported on $Fe_3O_4(111)$ increase in stability (decrease in chemical potential) by ~55 kJ/mol as the Ag particle size grows from ~0.6 nm to ~4 nm, but stabilizes near the chemical potential in bulk Ag solid after reaching a diameter of ~4 nm. The adhesion energy for ~4 nm Ag(solid) particles to $Fe_3O_4(111)$ was found to be 2.5±0.3 J/m^2, similar to values found for Ag on $CeO_{2-x}(111)$ surfaces.

Acknowledgements

The authors acknowledge the Department of Energy, Office of Basic Energy Sciences, Chemical Sciences Division under Grant No. DE-FG02-96ER14630, for support of this work.

6.5 Figures

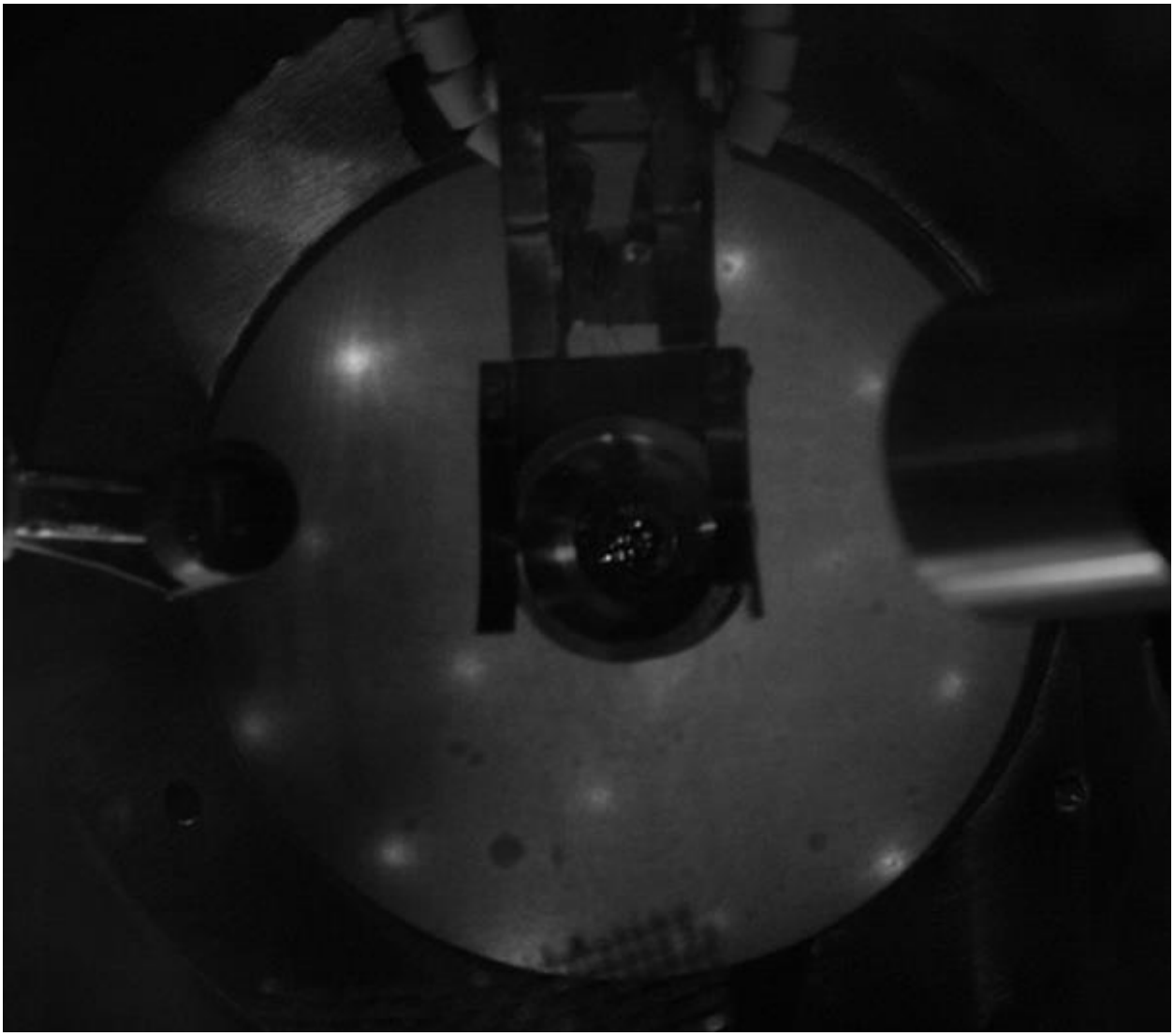

Figure 6.1 LEED Pattern at 60 eV of 6 nm thick Fe_3O_4(111) film grown on Pt(111). The (0,0) spot is near the center but hidden by the sample holder.

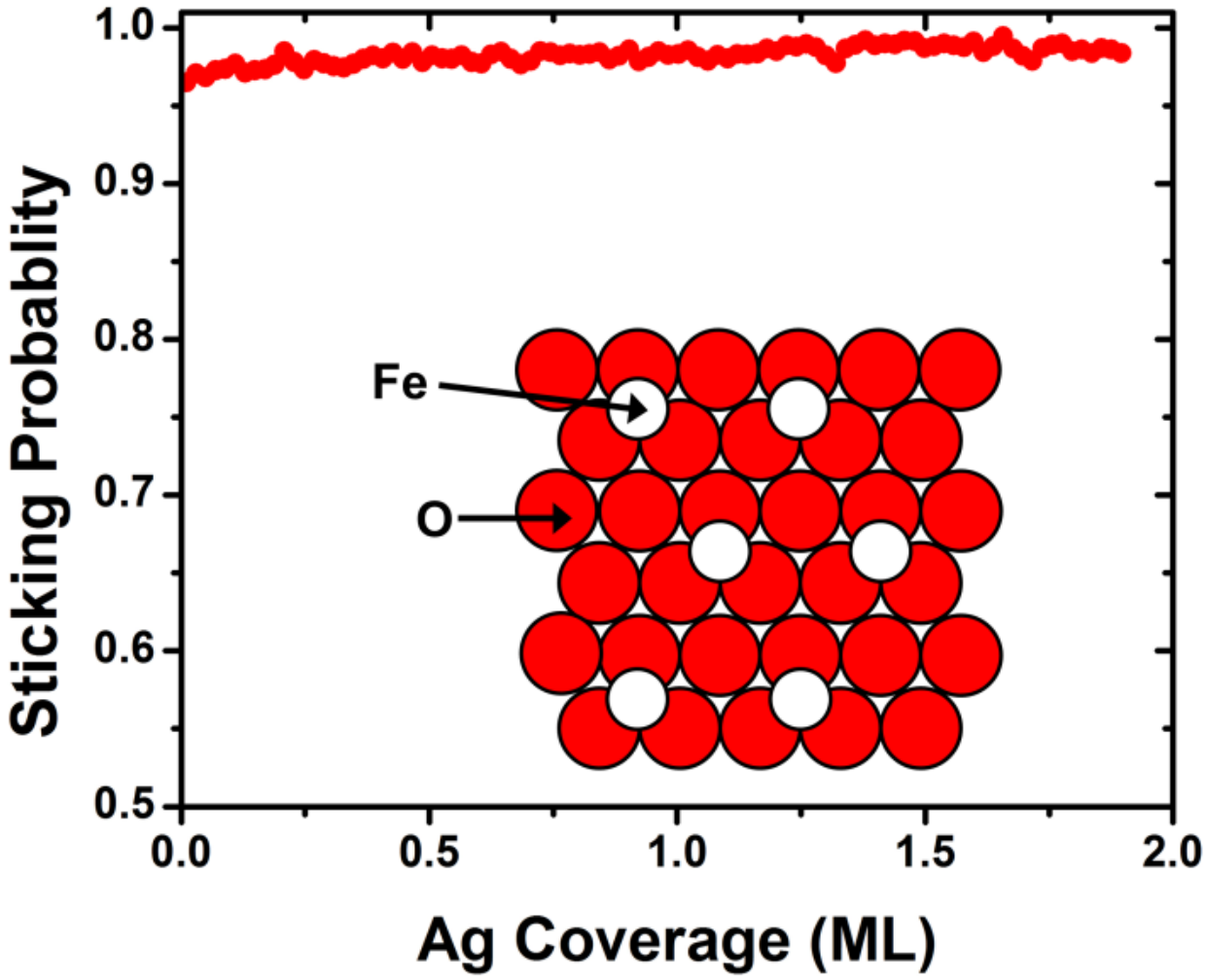

Figure 6.2 Sticking probability of Ag atoms onto the $Fe_3O_4(111)$ thin film at 300 K as function of Ag coverage. One monolayer is defined as 1.42 x 10^{15} atoms per cm^2**,** which is the number of oxygen atoms exposed to the vacuum per unit area for $Fe_3O_4(111)$. The insert shows a structural model of the $Fe_3O_4(111)$ surface.

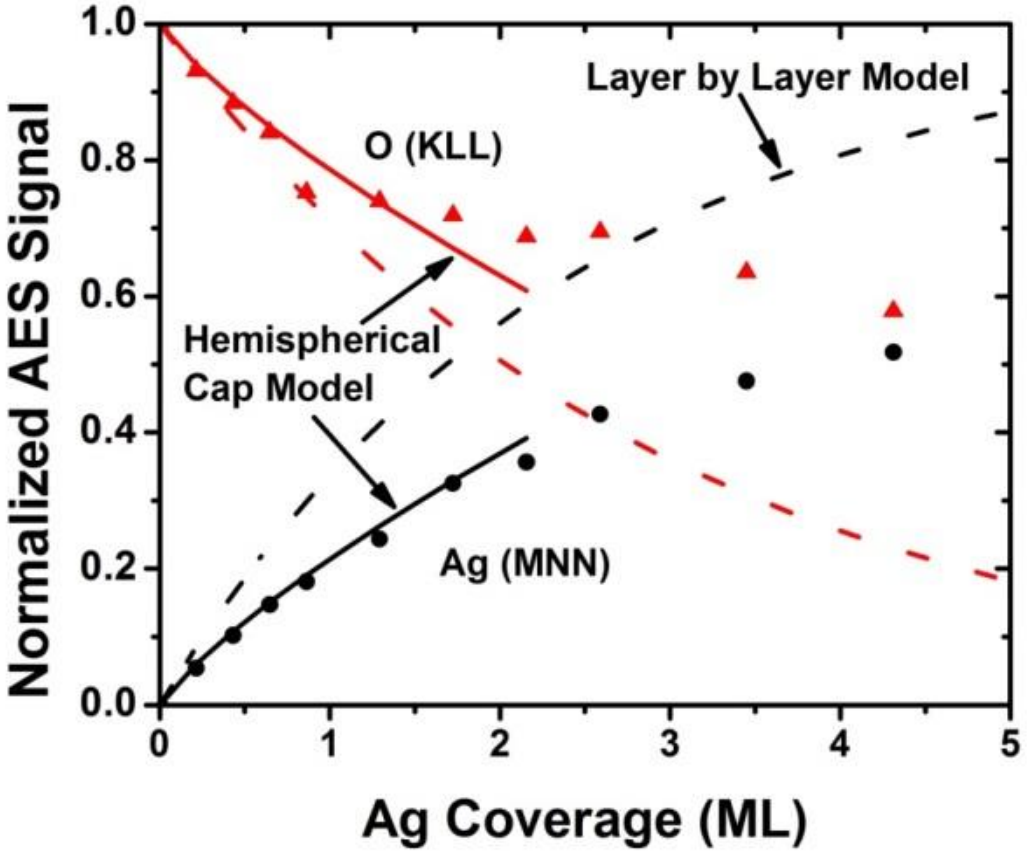

Figure 6.3 Integrated Ag (circles) and O (triangles) AES intensities, normalized to bulk Ag and the clean $Fe_3O_4(111)$ surface, respectively, versus Ag coverage at 300 K. The dashed curves correspond to the expected behavior if Ag grew layer-by-layer. The solid curves correspond to the calculated curve for a hemispherical cap model (with a Ag particle density of 4×10^{12} particles per cm^2). The inelastic mean path used was 0.71 nm for Ag and 0.93 nm for O,[116] and the detection angle was 45°.

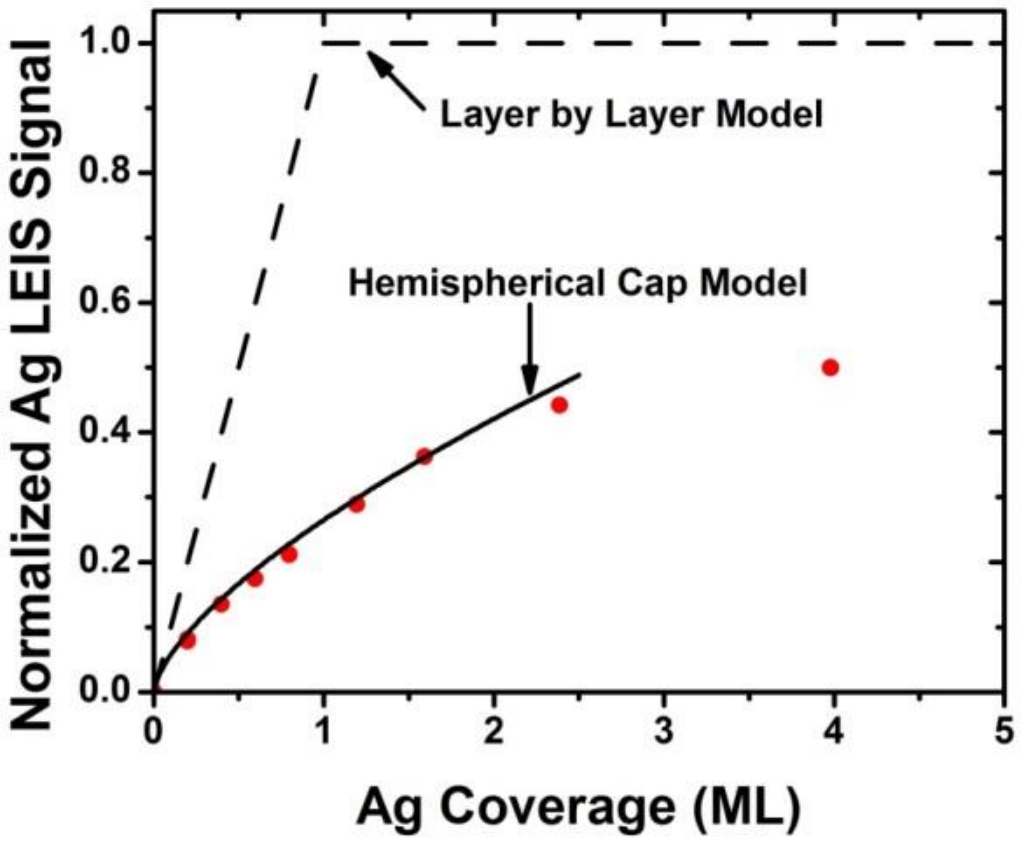

Figure 6.4 Integrated Ag LEIS intensity, normalized to bulk Ag, versus Ag coverage at 300 K on Fe_3O_4(111). The dashed lines correspond to the expected curve if Ag grew layer-by-layer. The solid curve corresponds to the calculated curve for a hemispherical cap model (with a Ag particle density of 4 x 10^{12} particles per cm^2).

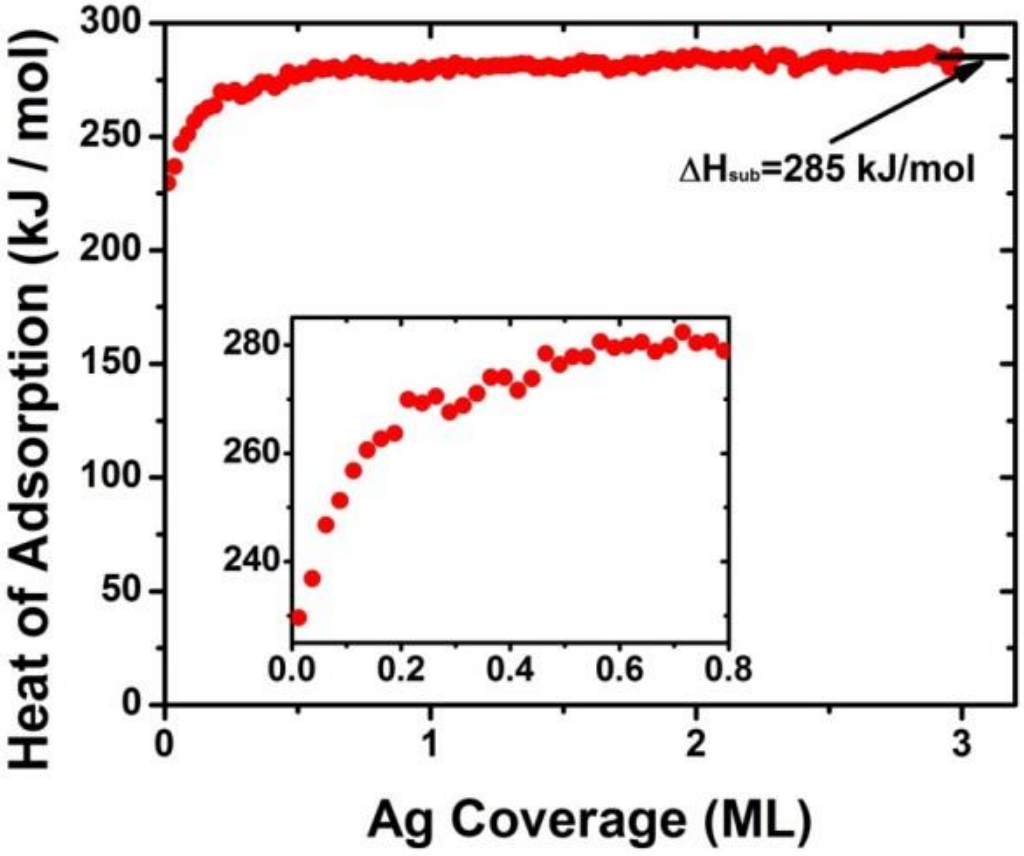

Figure 6.5 Heat of Ag atom adsorption versus Ag coverage at 300 K on $Fe_3O_4(111)$. The data is the average of three experiments. Each data point represents a pulse of 0.025 ML of Ag. The inserts shows the 0 – 0.8 ML range in expanded scale.

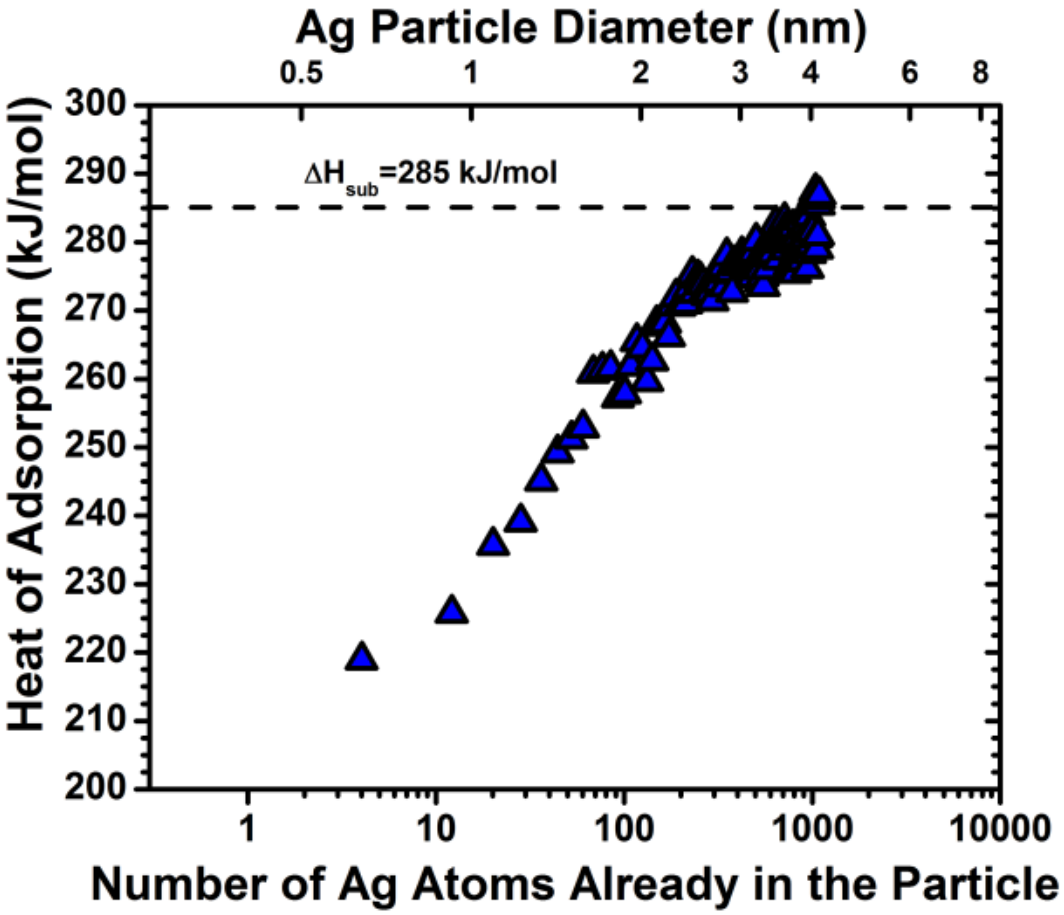

Figure 6.6 Measured heat of Ag atom adsorption versus the average Ag particle size on $Fe_3O_4(111)$ at 300 K. The Ag particle size is expressed as both the effective diameter and the number of Ag atoms already in the particle, both estimated assuming the Ag is in the form of 3D particles with a fixed density of 4×10^{12} particles per cm^2, as measured by AES and LEIS. The diameter is estimated assuming hemispherical shape, an assumption also used in analyzing the AES and LEIS data.

Chapter 7 The Hemispherical Cap Model for Analyzing Electron Spectroscopy Signals during Thin Film Growth: Extension to Non-Normal Detection Angles

J.C. Sharp and C.T. Campbell

Department of Chemistry

University of Washington

Seattle, Washington 98195-1700, USA

Abstract

The growth of nanoparticles on a surface are key ingredients many heterogeneous catalysts, fuel cells, other electrocatalysts and photocatalysts. The size of these nanoparticles can have an effect on the usability. To study the size of these nanoparticles an electron spectroscopy can be used. For electron spectroscopy conducted at an angle normal to the surface, the relationship between the normalized electron intensity and the particles' size and density has been derived. In this paper, we used a numerical method to determine the normalized electron intensities versus the particles radius divided by the inelastic mean free path for angles other than normal detection. We used this information to give a method for modifying the results at non-normal angles to fit the expected results for detection at normal to the surface. Further we show that for large values of the particle radius per the inelastic mean free path, the ratio of the normalized intensity is nearly equal to the ratio of the spectroscopic footprints given by $0.5*(1+1/\cos\theta)$, where θ is the angle of detection from normal.

A very common structural motif in materials science involves nanoparticles of one material dispersed across the surface of another. Such structures are commonly encountered when making and/or studying catalysts, microelectronics, plasmonic and optical devices, nanoelectrode arrays, coatings and thin film growth by vapor deposition or other condensation processes. For example, metal nanoparticles dispersed across the surfaces of oxides and carbon supports are key ingredients in many heterogeneous catalysts, fuel cells, other electrocatalysts and photocatalysts, all of which are crucial for energy, fuel and environmental technologies and chemical processing. One of the three growth modes that occur during thin film growth by vapor deposition is the Volmer-Weber mode, whereby clusters of the deposited material first nucleate and then grow as 3-D nanoparticles on the substrate.[35,52,83,105,106,117] A very common method to estimate the size and number density of such nanoparticles is based upon measurements of the intensities of peaks associated with substrate and adsorbate elements using an electron spectroscopy, typically either X-Ray Photoelectron Spectroscopy (XPS) or Auger Electron Spectroscopy (AES). A model that has been very widely applied for analyzing these intensities is the hemispherical cap model introduced by Diebold et al.,[52] which assumes that the nanoparticles all have the shape of hemispheres with the same diameter at any coverage. It is often applied to cases where the intensities of substrate and adsorbate peaks have been measured versus the amount of adsorbate deposited on the flat substrate surface, in which case the further assumption is made that the number of particles per unit area remains constant. This number density is estimated from a fit of these plots of intensities versus coverage to the resulting equations of this hemispherical cap model, which also gives the average diameter of the particles versus coverage.[52,106] Unfortunately, these equations for the hemispherical cap model only apply when the electron intensities have been measured for a take-off angle normal to the substrate

surface. Here, we present an expansion of that model that allows it to be applied at other angles of electron detection, which are often demanded by the constraints on sample mounting or manipulation.

In either XPS or AES, electrons are emitted from a material due to interaction with either X-Ray photons or high energy electrons. The intensity of the electrons emitted at given kinetic energies is element specific. These electrons can interact with matter prior to escaping vacuum and lose energy. The probability for an electron to traverse through matter without the loss of energy, is defined as escape probability, p_{escape}, and is given by the equation

$$p_{\text{escape}} = e^{-d/\lambda}\,, \tag{1}$$

where d is the distance the electron transverses through matter, referred to as the attenuation distance, and λ is the characteristic inelastic mean free path for the measured electron, which depends on its kinetic energy and the material, as reported in detail.[118] Using Equation 1 for a simple over-layer of an adsorbate on a substrate, the ratio of the intensity of electrons from the substrate, I_{sub}, covered by an over-layer of thickness, t, to the intensity with no over-layer, $I_{sub,0}$ can be determined. Similarly, the ratio of the intensity of electrons from an over-layer, I_{ads}, to the intensity of electron from an infinitely thick adsorbate over-layer, $I_{ads,\,\infty}$, can also be determined.[119] For normal detection the equations, respectively, are

$$I_{sub}/I_{sub,0} = e^{-t/\lambda_{sub}} \tag{2}$$

$$I_{ads}/I_{ads,\infty} = 1 - e^{-t/\lambda_{abs}} \tag{3}$$

Where where λ_{sub} is the inelastic mean free path of electrons from the substrate and λ_{abs} is the inelastic mean free path of electrons from the adsorbate. When the angle of detection is instead

at some angle θ from normal to the surface, the thickness, *t*, is replaced with *t* cos θ in these equations.

When the adsorbate is in the form of nanoparticles instead of a uniformly thick layer, the analysis is much more complex, since the distance any electron travels through the solids is dependent upon where the electron originated from within the plane of the substrate surface. In the hemispherical cap model mentioned above, the ratio of the intensity of emitted electrons from adsorbed hemispherical particles to the intensity of emitted electrons from an infinitely thick film of the same adsorbate was determined for the case of normal detection by averaging (integrating) over the total surface area,[52] and found to be

$$\frac{I_{ads}}{I_{ads(\infty)}} = n\pi R^2 - 2\pi n\lambda_{ads}^2\left[1 - \left[1 + \frac{R}{\lambda_{ads}}\right]e^{-R/\lambda_{ads}}\right], \qquad (4)$$

where *n* is the particle density, *R* is the radius of the hemispherical caps. For the signal from the substrate relative to the signal at zero coverage, they found that:

$$\frac{I_{sub}}{I_{sub(0)}} = 1 - n\pi R^2 - 2\pi n\lambda_{sub}^2\left[1 - \left[1 + \frac{R}{\lambda_{sub}}\right]e^{-R/\lambda_{sub}}\right]. \qquad (5)$$

These equations only work for electrons emitted normal to the surface.

In order to determine the relationship between particle geometry and signal intensity of electron spectroscopies using non-normal detection methods, Equations 4 and 5 can be derived by integrating the escape probability given in Equation 1, where the distance an electron travels is simply the z-coordinate of a hemisphere centered at (0, 0, 0). In this case, the surface is defined as the *z*=0 plane. For non-normal detection the distance an electron travels through the adsorbate from a single coordinate is no longer the *z*-coordinate of the hemispherical cap as described in eq. 6, nor is it simply related to the *z*-coordinate divided by cos(θ). Figure 1

illustrates how using a $d/\cos(\theta)$ correction would overestimate the attenuation length for electrons from the substrate in the "shadow" of the hemispherical cap. In Figure 1, the solid part of the lines represent where an electron would be traveling through the adsorbate, while the dashes part represents traveling through vacuum where there is no probability of energy loss. Since we know of no method for solving for all distances symbolically, we instead propose the following numerical method.

The substrate surface, with the surface defined as the z=0 plane, is divided up into discrete segments. For a single point in one of these segments, the distance an electron emitted from that point would travel through the hemispherical cap is calculated and used as the average for all points in that particular segment. For points on the surface directly underneath the hemispherical cap, the distance is calculated by determining the length of a line originating from the point and with an angle from normal to the surface same as that of the detector intersects the hemispherical cap. For points on the "shadow," the line originating from the point intercepts the hemisphere twice. The distance between these two intersections is the distance an electron travels through the hemispherical cap. These same distances are used to calculate the signal from the adsorbate. The limits on where this calculation is performed in from $-R$ to R in the y-direction and from $-R/\cos(\theta)$ to R in the x-direction. Outside of these limits the attenuation due to the adsorbate is zero. Assuming the particles are distributed on the surface hexagonally, the maximum R can reach before spectroscopic footprints overlap is in determined the following equation,

$$2\sqrt{1/2n\sqrt{3}} \Big/ 1 + 1/\cos(\theta). \qquad (6)$$

When these distances are used in conjunction with Equation 1, the escape probability for an electron from any point on the surface or substrate can be determined. These results can then be normalized by dividing by the escape probability at d = 0 for electrons from the substrate and d = ∞ for electrons from the adsorbate. To verify the methodology, the values calculated using this method at normal detection were compared to those calculated using Equation 4, as shown in Figure 2. Using a step size 0.01 nm, i.e., a discrete segment has an area of 0.0001 nm^2, to calculate the signal from the hemispherical cap leads to a percent error from Equation 4 of less than 0.1%. As usual with numeric integration, choosing a smaller step size leads to a greater accuracy while increasing the computational time. Changing the step size from 0.02 nm to 0.01 nm leads to less than 0.01% change in the calculated values.

Figure 3 shows a plot of the normalized electron intensity at a specified take-off angle divided by the normalized electron intensity at normal detection versus the radius of the particle, *R*, divided by the inelastic mean free path for an electron, λ, from the adsorbate assuming a constant particle density for detection at 0°, 30°, 45°, 60°, 70º and 75° from normal.. This plot will allow the reader to be able to correct experimentally acquired data to that of normal detection and fit it to Equation 4 using relevant values for *n* and *λ.* As Figure 3 show the value for the ratio of the normalized electron intensities approach a single value for large *R/λ* which is nearly equal to the ratio of the spectroscopic footprints given by

$$0.5\left(1+\frac{1}{\cos\theta}\right). \tag{7}$$

To determine the normalized signal from the substrate at a given angle, the following equation is used

$$\frac{I_{sub}}{I_{sub,\infty}} = 1-\left(\frac{I_{abs}}{I_{abs,normal}}\right)\frac{I_{abs,normal}}{I_{abs,\infty}}. \tag{8}$$

Where $I_{abs}/I_{abs,\ normal}$ is read from Figure 3 for a given R/λ and $I_{abs,\ normal}/\ I_{abs,\infty}$ is determined from Equation 4 for a given R, λ and n.

In conclusion, we have applied a numerical method to determine the normalized electron spectroscopy intensity for varying angles from normal for hemispherical caps. We verified this method by comparing it the results the numerical method generated with results determined previously using the equations from Diebold *et al*. and found less than 0.1% error with a step size of 0.01 nm. We have also given readers a method to correct experimental results at non-normal angles to fit the equations derived by Diebold *et al.*, so density of nanoparticles on the surface can be determined.

7.1 Figures

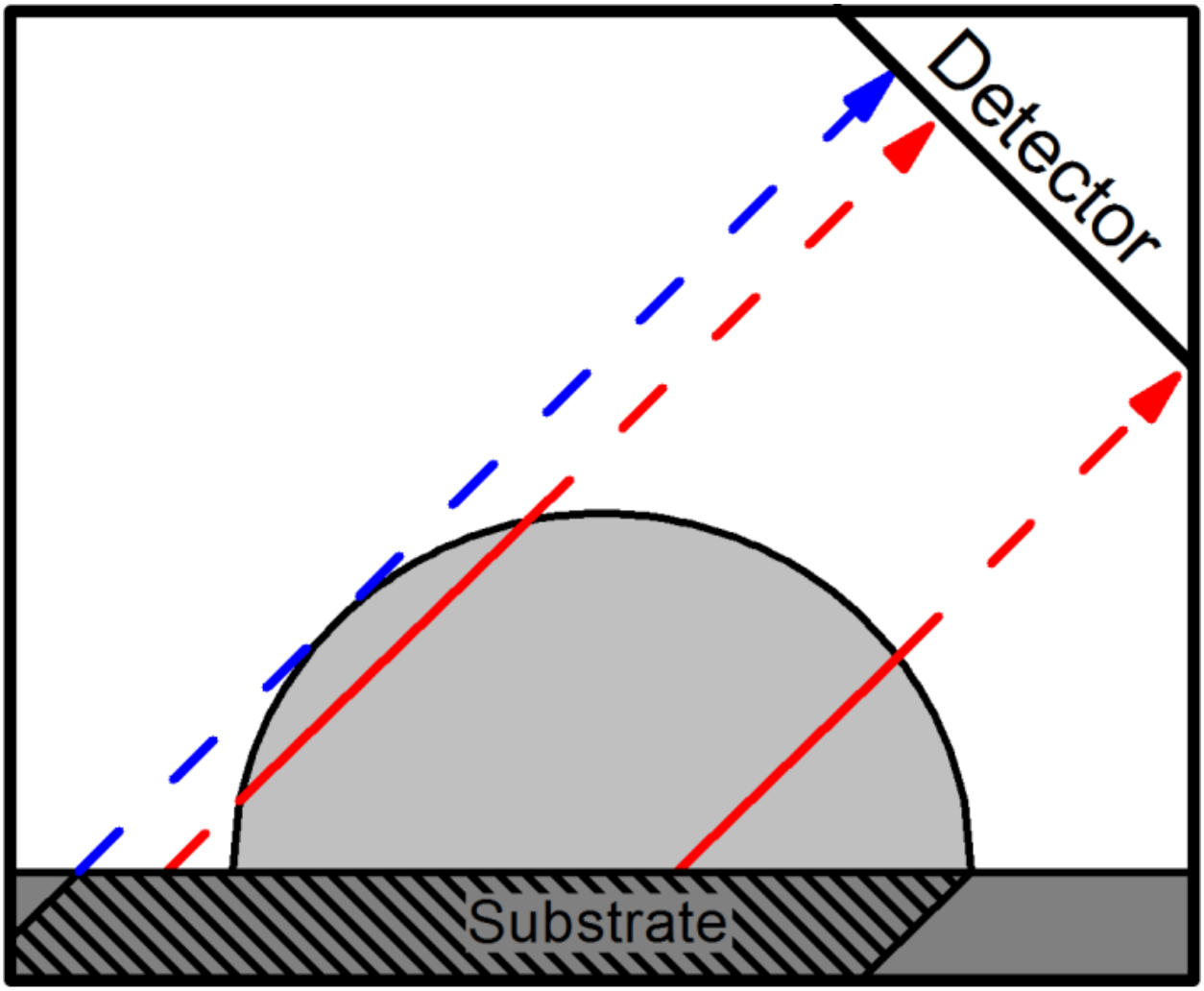

Figure 7.1 Electrons emmited from the substrate will be attenuated by the hemispherical cap if they originate from either the area under the cap or from the shadow created by the cap as indicated by the hashed area. The hashed area of the substrate therefore represents the effective spectroscopic footprint of the particle at this particular angle.

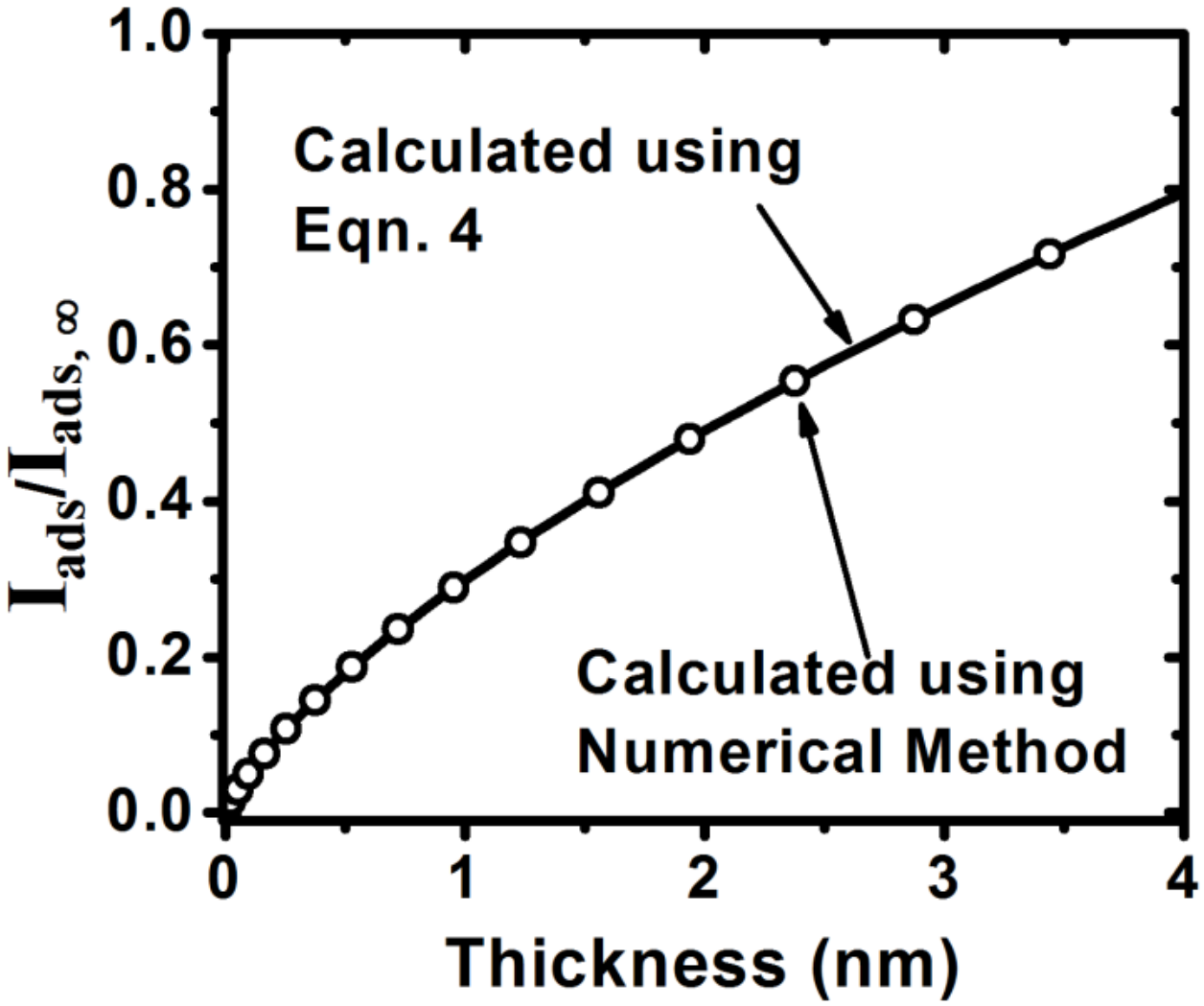

Figure 7.2 Intensity of adsorbate electrons relative to that for an infinitely thick film versus average thickness for hemispherical caps with number density n=0.005 particles/nm^2 and λ=1 nm. The solid line is calculated using Equation 1 and the open circles were determined using the numerical method with a step size of 0.01 nm and have a less than 0.1% deviation from the solid line.

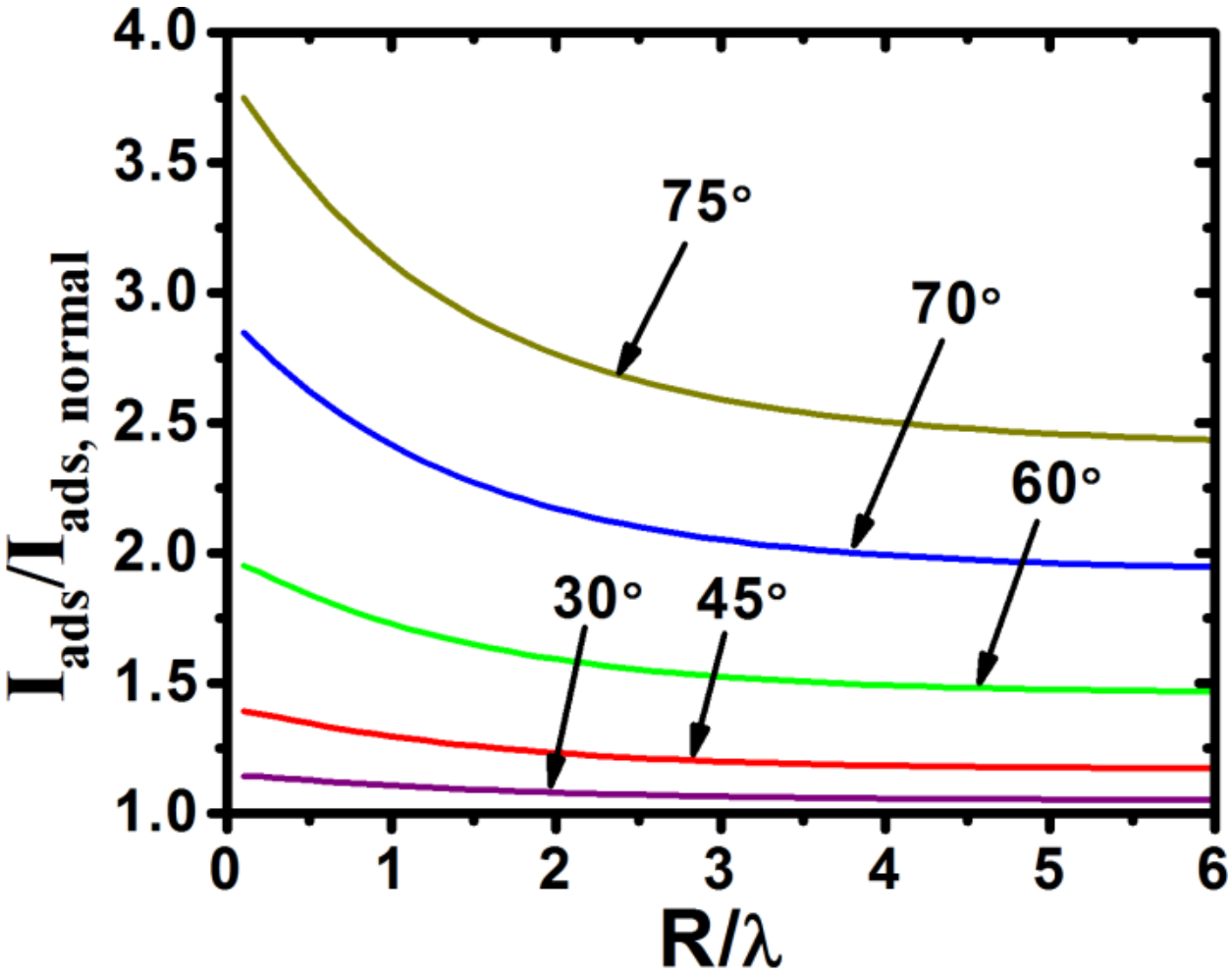

Figure 7.3 Plot of the normalized electron intensity for a peak associated with the adsorbed hemispherical particles at different take-off angles divided by the electron intensity at normal detection, plotted versus the radius of the adsorbed particle, *R*, divided by the inelastic mean free path for that electron through the adsorbed material, λ, assuming a constant particle density. This plot allows readers to correct values calculated using the standard hemispherical cap model derived for normal detection (i.e., Eqn. 4) to fit experimental data acquired at other detection angles, which in turn allows one to quantitatively estimate particle densities from such data.

Chapter 8 Conclusions

In this dissertation, surface science techniques were applied to study the metal / organic and metal / inorganic interfaces. In the chapters 3, 4, and 5, the growth of Ca onto polymers that are of interest in OPVs and OLEDs were studied. In chapter 6, the growth of Ag / Fe_3O_4(111) interface was studied. The energetics of late transition metal on oxide surfaces are of particular interest in catalysts, fuel cells, other electrocatalysts and photocatalysts. In chapter 7, a method for determining particle size and number density for Volmer-Weber growth using photoelectron spectroscopy data acquired at an angle other than normal is detailed. Previously these values could only be determined from photoelectron spectroscopy data acquired at normal to surface.

In chapter 3, the formation of the Ca / MEH-CN-PPV interface was studied calorimetry, LEIS, and XPS at 300 K and 130 K. Based on calorimetry and XPS data, at low coverage (<1 ML), CA was found to diffuse and react with cyano or alkoxy groups in the polymer chain, with the dominant reaction has Ca removing two cyano groups and forming $Ca(CN)_2$ and cross-linking polymer chains. After 4 ML, the dominant reaction was Ca binding to Ca and forming 3D islands. For deposition at low temperatures, the subsurface diffusion / reaction of Ca was significantly decreased. The effective thickness of the reacted polymer went from an estimated 5.6 nm (7 monomer layers) at 300 K to 1.0 nm (1.2 monomer layers) at 130 K.

In chapters 4 and 5, the formation of the Ca / PDHF and Ca / PDFHV interfaces were studied calorimetry, LEIS, XPS, and UPS at different temperatures and with and without electron damage. Ca deposited on these surfaces can desorb, diffuse across and into the surface, and react with defects in PDHF and PDFHV, or bond with other Ca atoms on the surface to form 3D islands. At very low coverages (<0.75 ML), the dominant reaction is with defects in the

polymers or impurities. After 0.75 ML, the main reaction is Ca binding to Ca and forming 3D islands on the surface. As with the Ca / MEH-CN-PPV, deposition of Ca at low temperatures (130 K), decreased the subsurface diffusion / reaction of Ca, thus increased the growth of Ca(s) on the surface. For the electron-damaged polymer surfaces, the electron damage increased the sticking probability of Ca and the slightly increased the heat of adsorption. The increases in the heat of adsorption are attributed to electron damage disrupting the polymer structure to enable faster Ca diffusion through the polymer. The electron damage did not significantly alter the morphology of the growing Ca(solid) particles on the surface of these polyfluorenes.

In chapter 6, growth of Ag on $Fe_3O_4(111)$ was studied by calorimetry, LEIS and AES. The initial heat of adsorption was ~230 kJ/mol, which is ~55kJ/mol weaker than the binding of Ag to bulk Ag. The initial sticking probability was ~0.96 and increased ~0.99 by 1.0 ML. The LEIS and AES data showed Ag grew as 3D islands on the surface. Fitting the LEIS and AES using a hemispherical cap model found the Ag particle density of 4×10^{12} particles per cm^2. Using this particle density, the average size of Ag particles was calculated at each Ag coverage, and the heat of adsorption versus Ag particle size was determined. From this, it was found that the Ag atoms in Ag nanoparticles supported on $Fe_3O_4(111)$ increase in stability (decrease in chemical potential) by ~55 kJ/mol as the Ag particle size grows from ~0.6 nm to ~4 nm, but stabilizes near the chemical potential in bulk Ag solid after reaching a diameter of ~4 nm. The adhesion energy for ~4 nm Ag(solid) particles to $Fe_3O_4(111)$ was found to be 2.5 ± 0.3 J/m^2, similar to values found for Ag on $CeO_{2-x}(111)$ surfaces.

In chapter 7, a numerical method for determining the normalized photoelectron signal from a hemispherical cap at angle of detection other than normal is detailed. This numerical method was verified by comparing its results at normal detection with the results determined using the

equations in Diebold *et al*., and found less than 0.1% error with a step size 0.01 nm. Using method, a way to correct data acquired at angle other than normal to that of normal detection is given. In particular for large values of the particle radius divided by the inelastic mean path, it is seen that the normalized photoelectron signal from the adsorbate is approximately 0.5*(1+1/cos θ), where θ is the angle from the surface normal.

References

(1) Friend, R. H.; Gymer, R. W.; Holmes, A. B.; Burroughes, J. H.; Marks, R. N.; Taliani, C.; Bradley, D. D. C.; Dos Santos, D. A.; Bredas, J. L.; Logdlund, M.; Salaneck, W. R. *Nature* **1999**, *397*, 121.

(2) Coakley, K. M.; McGehee, M. D. *Chemistry of Materials* **2004**, *16*, 4533.

(3) Granstrom, M.; Petritsch, K.; Arias, A. C.; Friend, R. H. *Synthetic Metals* **1999**, *102*, 957.

(4) Goodman, D. W. *Chemical Reviews* **1995**, *95*, 523.

(5) Baumer, M.; Freund, H. J. *Progress in Surface Science* **1999**, *61*, 127.

(6) Campbell, C. T. *Accounts of Chemical Research* **2013**, *46*, 1712.

(7) Santra, A. K.; Goodman, D. W. *Journal of Physics-Condensed Matter* **2003**, *15*, R31.

(8) Parker, I. D. *Journal of Applied Physics* **1994**, *75*, 1656.

(9) Yu, G.; Heeger, A. J. *Journal of Applied Physics* **1995**, *78*, 4510.

(10) Broms, P.; Birgersson, J.; Johansson, N.; Logdlund, M.; Salaneck, W. R. *Synthetic Metals* **1995**, *74*, 179.

(11) Halls, J. J. M.; Baigent, D. R.; Cacialli, F.; Greenham, N. C.; Friend, R. H.; Moratti, S. C.; Holmes, A. B. *Thin Solid Films* **1996**, *276*, 13.

(12) Zhu, J. F.; Bebensee, F.; Hieringer, W.; Zhao, W.; Baricuatro, J. H.; Farmer, J. A.; Bai, Y.; Steinruck, H. P.; Gottfried, J. M.; Campbell, C. T. *J. Am. Chem. Soc.* **2009**, *131*, 13498.

(13) Bebensee, F.; Zhu, J. F.; Baricuatro, J. H.; Farmer, J. A.; Bai, Y.; Steinruck, H. P.; Campbell, C. T.; Gottfried, J. M. *Langmuir* **2010**, *26*, 9632.

(14) Janssen, F. J. J.; van Ijzendoorn, L. J.; van der Gon, A. W. D.; de Voigt, M. J. A.; Brongersma, H. H. *Physical Review B* **2004**, *70*, 165425.

(15) Gao, Y.; Park, K. T.; Hsieh, B. R. *Journal of Applied Physics* **1993**, *73*, 7894.

(16) Hon, S. S.; Richter, J.; Stuckless, J. T. *Chemical Physics Letters* **2004**, *385*, 92.

(17) Ettedgui, E.; Hsieh, B. R.; Gao, Y. *Polymers for Advanced Technologies* **1997**, *8*, 408.

(18) Andersson, G. G.; van Gennip, W. J. H.; Niemantsverdriet, J. W.; Brongersma, H. H. *Chemical Physics* **2002**, *278*, 159.

(19) Giro, R.; Caldas, M. J. *Physical Review B* **2007**, *76*, 161303.

(20) Zhu, J.; Goetsch, P.; Ruzycki, N.; Campbell, C. T. *Journal of the American Chemical Society* **2007**, *129*, 6432.

(21) Granstrom, M.; Petritsch, K.; Arias, A. C.; Friend, R. H. *Synthetic Metals* **1999**, *102*, 953.

(22) Greenham, N. C.; Samuel, I. D. W.; Hayes, G. R.; Phillips, R. T.; Kessener, Y.; Moratti, S. C.; Holmes, A. B.; Friend, R. H. *Chemical Physics Letters* **1995**, *241*, 89.

(23) Fahlman, M.; Salaneck, W. R.; Moratti, S. C.; Holmes, A. B.; Bredas, J. L. *Chemistry-a European Journal* **1997**, *3*, 286.

(24) Peng, Z. H.; Galvin, M. E. *Chemistry of Materials* **1998**, *10*, 1785.

(25) Greenham, N. C.; Moratti, S. C.; Bradley, D. D. C.; Friend, R. H.; Holmes, A. B. *Nature* **1993**, *365*, 628.

(26) Halls, J. J. M.; Walsh, C. A.; Greenham, N. C.; Marseglia, E. A.; Friend, R. H.; Moratti, S. C.; Holmes, A. B. *Nature* **1995**, *376*, 498.

(27) Liao, L. S.; Cheng, L. F.; Fung, M. K.; Lee, C. S.; Lee, S. T.; Inbasekaran, M.; Woo, E. P.; Wu, W. W. *Chemical Physics Letters* **2000**, *325*, 405.

(28) Campbell, A. J.; Bradley, D. D. C.; Antoniadis, H. *Journal of Applied Physics* **2001**, *89*, 3343.

(29) Kulkarni, A. P.; Jenekhe, S. A. *Macromolecules* **2003**, *36*, 5285.

(30) van Woudenbergh, T.; Wildeman, J.; Blom, P. W. M.; Bastiaansen, J.; Langeveld-Voss, B. M. W. *Advanced Functional Materials* **2004**, *14*, 677.

(31) Arias, A. C.; MacKenzie, J. D.; Stevenson, R.; Halls, J. J. M.; Inbasekaran, M.; Woo, E. P.; Richards, D.; Friend, R. H. *Macromolecules* **2001**, *34*, 6005.

(32) Halls, J. J. M.; Arias, A. C.; MacKenzie, J. D.; Wu, W. S.; Inbasekaran, M.; Woo, E. P.; Friend, R. H. *Advanced Materials* **2000**, *12*, 498.

(33) Liao, L. S.; Fung, M. K.; Lee, C. S.; Lee, S. T.; Inbasekaran, M.; Woo, E. P.; Wu, W. W. *Applied Physics Letters* **2000**, *76*, 3582.

(34) Choong, V. E.; Park, Y.; Hsieh, B. R.; Gao, Y. *Journal of Physics D-Applied Physics* **1997**, *30*, 1421.

(35) Campbell, C. T. *Surface Science Reports* **1997**, *27*, 1.

(36) Campbell, C. T. *Journal of the Chemical Society-Faraday Transactions* **1996**, *92*, 1435.

(37) George, S. M. *Chemical Reviews* **1995**, *95*, 475.

(38) Ertl, G. *Handbook of heterogeneous catalysis*; VCH: Weinheim, 1997.

(39) Campbell, C. T.; Sellers, J. R. V. *Faraday Discussions* **2013**, *162*, 9.

(40) Haruta, M. *Catalysis Today* **1997**, *36*, 153.

(41) Schalow, T.; Brandt, B.; Starr, D. E.; Laurin, M.; Shaikhutdinov, S. K.; Schauermann, S.; Libuda, J.; Freund, H. J. *Angewandte Chemie-International Edition* **2006**, *45*, 3693.

(42) Fischer-Wolfarth, J.-H.; Farmer, J. A.; Flores-Camacho, J. M.; Genest, A.; Yudanov, I. V.; Roesch, N.; Campbell, C. T.; Schauermann, S.; Freund, H.-J. *Physical Review B* **2010**, *81*.

(43) Sun, Y. N.; Qin, Z. H.; Lewandowski, M.; Shaikhutdinov, S.; Freund, H. J. *Surface Science* **2009**, *603*, 3099.

(44) Meyer, R.; Shaikhutdinov, S. K.; Freund, H. J. *Zeitschrift Fur Physikalische Chemie-International Journal of Research in Physical Chemistry & Chemical Physics* **2004**, *218*, 905.

(45) Qin, Z. H.; Lewandowski, M.; Sun, Y. N.; Shaikhutdinov, S.; Freund, H. J. *Journal of Physical Chemistry C* **2008**, *112*, 10209.

(46) Kiejna, A.; Ossowski, T.; Pabisiak, T. *Physical Review B* **2012**, *85*.

(47) Xu, W. X.; Wang, L. C.; Wang, R.; Fu, X. C. *Journal of Colloid and Interface Science* **1996**, *179*, 350.

(48) Estrella, M.; Barrio, L.; Zhou, G.; Wang, X.; Wang, Q.; Wen, W.; Hanson, J. C.; Frenkel, A. I.; Rodriguez, J. A. *Journal of Physical Chemistry C* **2009**, *113*, 14411.

(49) Yu, X.; Wang, S.-G.; Li, Y.-W.; Wang, J.; Jiao, H. *Journal of Physical Chemistry C* **2012**, *116*, 10632.

(50) Gatel, C.; Snoeck, E. *Surface Science* **2006**, *600*, 2650.

(51) Zhang, D.-H.; Li, H.-B.; Li, G.-D.; Chen, J.-S. *Dalton Transactions* **2009**, 10527.

(52) Diebold, U.; Pan, J. M.; Madey, T. E. *Physical Review B* **1993**, *47*, 3868.

(53) Venables, J. *Introduction to surface and thin film processes*; Cambridge University Press: Cambridge, UK; New York, 2000.

(54) Vickerman, J. C. *Surface analysis : the principal techniques*; John Wiley: Chichester [England]; New York, 1997.

(55) Borronibird, C. E.; Alsarraf, N.; Andersson, S.; King, D. A. *Chemical Physics Letters* **1991**, *183*, 516.

(56) Borronibird, C. E.; King, D. A. *Review of Scientific Instruments* **1991**, *62*, 2177.

(57) Alsarraf, N.; Stuckless, J. T.; Wartnaby, C. E.; King, D. A. *Surface Science* **1993**, *283*, 427.

(58) Stuckless, J. T.; Frei, N. A.; Campbell, C. T. *Review of Scientific Instruments* **1998**, *69*, 2427.

(59) Diaz, S. F.; Zhu, J. F.; Harris, J. J. W.; Goetsch, P.; Merte, L. R.; Campbell, C. T. *Surface Science* **2005**, *598*, 22.

(60) Baigent, D. R.; Marks, R. N.; Greenham, N. C.; Friend, R. H.; Moratti, S. C.; Holmes, A. B. *Synthetic Metals* **1995**, *71*, 2177.

(61) Chang, C. C.; Pai, C. L.; Chen, W. C.; Jenekhe, S. A. *Thin Solid Films* **2005**, *479*, 254.

(62) Starr, D. E.; Campbell, C. T. *Journal of Physical Chemistry B* **2001**, *105*, 3776.

(63) Pauls, S. W.; Campbell, C. T. *Surface Science* **1990**, *226*, 250.

(64) Campbell, C. T.; Sellers, J. R. V. *Journal of the American Chemical Society* **2012**, *134*, 18109.

(65) Strunskus, T.; Kiene, M.; Willecke, R.; Thran, A.; von Bechtolsheim, C.; Faupel, F. *Materials and Corrosion-Werkstoffe Und Korrosion* **1998**, *49*, 180.

(66) Smithson, R. L. W.; McClure, D. J.; Evans, D. F. *Thin Solid Films* **1997**, *307*, 110.

(67) Strunskus, T.; Zaporojtchenko, V.; Behnke, K.; von Bechtolsheim, C.; Faupel, F. *Advanced Engineering Materials* **2000**, *2*, 489.

(68) Bebin, P.; Prud'homme, R. E. *Chemistry of Materials* **2003**, *15*, 965.

(69) Zaporojtchenko, V.; Zekonyte, J.; Biswas, A.; Faupel, F. *Surface Science* **2003**, *532*, 300.

(70) Beamson, G.; Briggs, D. *High Resolution XPS of Organic Polymers : the Scienta ESCA300 Database*; Wiley: Chichester [England]; New York, 1992.

(71) Lee, D. W.; Kim, K.; Jin, J. I.; Park, Y. *Synthetic Metals* **2004**, *143*, 181.

(72) Li, S.; Kang, E. T.; Ma, Z. H.; Tan, K. L. *Surface and Interface Analysis* **2000**, *29*, 95.

(73) Zurcher, P.; Bauer, R. S. *Journal of Vacuum Science & Technology a-Vacuum Surfaces and Films* **1983**, *1*, 695.

(74) Moulder, J.; Stickle, W.; Sobol, P.; Bomben, K. *Handbook of X-ray Photoelectron Spectroscopy*; 2nd ed.; Perkin-Elmer: MN, 1992.

(75) Sugama, T.; Kukacka, L. E.; Carciello, N.; Hocker, N. J. *Cement and Concrete Research* **1989**, *19*, 857.

(76) Benson, N.; Gassmann, A.; Mankel, E.; Mayer, T.; Melzer, C.; Schmechel, R.; von Seggern, H. *Journal of Applied Physics* **2008**, *104*, 054505.

(77) W. M. Haynes, e. *CRC Handbook of Chemistry and Physics*; 93rd Edition (Internet Version 2013) ed.; CRC Press/Taylor and Francis: Boca Raton, FL, 2013.

(78) Farmer, J. A.; Campbell, C. T. *Science* **2010**, *329*, 933.

(79) Chen, Z.; Shen, Y. R.; Somorjai, G. A. *Annual Review of Physical Chemistry* **2002**, *53*, 437.

(80) Jeng, U.; Hsu, C. H.; Sheu, H. S.; Lee, H. Y.; Inigo, A. R.; Chiu, H. C.; Fann, W. S.; Chen, S. H.; Su, A. C.; Lin, T. L.; Peng, K. Y.; Chen, S. A. *Macromolecules* **2005**, *38*, 6566.

(81) Dean, J. A.; Lange, N. A. *Lange's Handbook of Chemistry. 13.ed*; McGraw-Hill,1985: New York,N.Y., 1985.

(82) Bebensee, F.; Schmid, M.; Steinrueck, H.-P.; Campbell, C. T.; Gottfried, J. M. *Journal of the American Chemical Society* **2010**, *132*, 12163.

(83) Zhu, J.; Farmer, J. A.; Ruzycki, N.; Xu, L.; Campbell, C. T.; Henkelman, G. *Journal of the American Chemical Society* **2008**, *130*, 2314.

(84) Venables, J. A. *Surface Science* **1994**, *299*, 798.

(85) Neher, D. *Macromolecular Rapid Communications* **2001**, *22*, 1366.

(86) Kreyenschmidt, M.; Klaerner, G.; Fuhrer, T.; Ashenhurst, J.; Karg, S.; Chen, W. D.; Lee, V. Y.; Scott, J. C.; Miller, R. D. *Macromolecules* **1998**, *31*, 1099.

(87) Weinfurtner, K.-H.; Fujikawa, H.; Tokito, S.; Taga, Y. *Applied Physics Letters* **2000**, *76*, 2502.

(88) Grice, A. W.; Bradley, D. D. C.; Bernius, M. T.; Inbasekaran, M.; Wu, W. W.; Woo, E. P. *Applied Physics Letters* **1998**, *73*, 629.

(89) Chen, M.; Feng, X. F.; Zhang, L.; Ju, H. X.; Xu, Q.; Zhu, J. F.; Gottfried, J. M.; Ibrahim, K.; Qian, H. J.; Wang, J. O. *Journal of Physical Chemistry C* **2010**, *114*, 9908.

(90) Ju, H.; Feng, X.; Ye, Y.; Zhang, L.; Pan, H.; Campbell, C. T.; Zhu, J. *Journal of Physical Chemistry C* **2012**, *116*, 20465.

(91) Sharp, J. C.; Bebensee, F.; Baricuatro, J. H.; Steinrueck, H. P.; Gottfried, J. M.; Campbell, C. T. *Journal of Physical Chemistry C* **2013**, *117*, 23781.

(92) Tanuma, S.; Powell, C. J.; Penn, D. R. *Surface and Interface Analysis* **1991**, *17*, 911.

(93) *CRC Handbook of Chemistry and Physics*; 92nd Edition (Internet Version 2012) ed.; CRC Press/Taylor and Francis: Boca Raton, FL.

(94) Zekonyte, J.; Erichsen, J.; Zaporojtchenko, V.; Faupel, F. *Surface Science* **2003**, *532*, 1040.

(95) Nowak, S.; Groning, P.; Kuttel, O. M.; Collaud, M.; Dietler, G. *Journal of Vacuum Science & Technology a-Vacuum Surfaces and Films* **1992**, *10*, 3419.

(96) Collaud, M.; Nowak, S.; Kuttel, O. M.; Groning, P.; Schlapbach, L. *Applied Surface Science* **1993**, *72*, 19.

(97) Massey, S.; Cloutier, P.; Bazin, M.; Sanche, L.; Roy, D. *Journal of Applied Polymer Science* **2008**, *108*, 3163.

(98) Makuuchi, K.; Cheng, S. *Radiation processing of polymer materials and its industrial applications*; Wiley: Hoboken, N.J, 2011.

(99) Clough, R. L.; Shalaby, W. S. *Radiation effects on polymers*; American Chemical Society: Washington, D.C., 1991.

(100) Sezen, M.; Plank, H.; Fisslthaler, E.; Chernev, B.; Zankel, A.; Tchernychova, E.; Blumel, A.; List, E. J. W.; Grogger, W.; Polt, P. *Physical Chemistry Chemical Physics* **2011**, *13*, 20235.

(101) Montilla, F.; Mallavia, R. *Advanced Functional Materials* **2007**, *17*, 71.

(102) Sharp, J. C.; Feng, X. F.; Farmer, J. A.; Guo, Y. X.; Bebensee, F.; Baricuatro, J. H.; Zillner, E.; Zhu, J. F.; Steinrück, H.-P.; Gottfried, J. M.; Campbell, C. T. *Journal of Physical Chemistry C* **2014**, *118*, 2953.

(103) Campbell, C. T.; Paffett, M. T. *Surface Science* **1984**, *139*, 396

(104) Bao, X.; Muhler, M.; Pettinger, B.; Schlogl, R.; Ertl, G. *Catalysis Letters* **1993**, *22*, 215.

(105) Larsen, J. H.; Ranney, J. T.; Starr, D. E.; Musgrove, J. E.; Campbell, C. T. *Physical Review B* **2001**, *63*, 195410.

(106) Farmer, J. A.; Baricuatro, J. H.; Campbell, C. T. *Journal of Physical Chemistry C* **2010**, *114*, 17166.

(107) Campbell, C. T.; Sharp, J. C.; Yao, Y. X.; Karp, E. M.; Silbaugh, T. L. *Faraday Discussions* **2011**, *152*, 227.

(108) Ihm, H.; Ajo, H. M.; Campbell, C. T. *J. Phys. Chem. B* **2004**, *108*, 14627.

(109) Zscherpel, D.; Ranke, W.; Weiss, W.; Schlogl, R. *Journal of Chemical Physics* **1998**, *108*, 9506.

(110) Weiss, W.; Ranke, W. *Progress in Surface Science* **2002**, *70*, 1.

(111) Ritter, M.; Weiss, W. *Surface Science* **1999**, *432*, 81.

(112) Memeo, R.; Ciccacci, F.; Mariani, C.; Ossicini, S. *Thin Solid Films* **1983**, *109*, 159.

(113) Campbell, C. T.; Starr, D. E. *Journal of the American Chemical Society* **2002**, *124*, 9212.

(114) Campbell, C. T.; Parker, S. C.; Starr, D. E. *Science* **2002**, *298*, 811.

(115) Stuckless, J. T.; Starr, D. E.; Bald, D. J.; Campbell, C. T. *Journal of Chemical Physics* **1997**, *107*, 5547.

(116) Seah, M. P. a. D. W. A. *Surface and Interface Analysis* **1979**, *1*, 2.

(117) Venables, J. A. *Surface Science* **1994**, *299*, 798.

(118) NIST X-ray Photoelectron Spectroscopy Database, Version 3.5, National Institute of Standards and Technology, Gaithersburg, 2003 http://srdata.nist.gov/xps/

(119) Ertl, G.; J., K. *Low Energy Electrons and Surface Chemistry*; VCH: Weinheim, Federal Republic of Germany; Deerfield Beach, FL, USA, 1985.